A Three Pulse Optical Echo Study of Depolarising Collisions in Caesium

Thesis

A Three Pulse Optical Echo Study Of Depolarising Collisions in Caesium

William Thomason Dove B.Sc.(Dunelm) M.Sc.(Essex)

A thesis submitted in partial fulfilment of the requirements for the degree of Doctor of Philosophy in Physics at The Open University
27th June 1991

Abstract

The work described in this thesis is an experimental study, using three excitation pulse photon echoes, of collisional relaxation of caesium atoms perturbed by noble gases.

The theoretical aspects of this thesis include the development of a density matrix theory to describe the formation of echoes formed from a sequence of three excitation pulses when applied to a multi-level system. The manner in which the resultant echoes store information about optical coherences, Zeeman coherences and state populations is discussed. The theory of collisional relaxation of three excitation pulse echoes by depolarising collisions and velocity changing collisions is introduced. Measurements of collision cross sections for depolarising collisions and velocity changing collisions for atoms in a single state are possible by the three excitation pulse echo techniques.

The experimental work of this thesis involves the measurement of collisional relaxation of three pulse echoes formed on the caesium $6S_{\frac{1}{2}} \leftrightarrow 7P_{\frac{3}{2}}$ (455 nm) and $6S_{\frac{1}{2}} \leftrightarrow 7P_{\frac{1}{2}}$ (459 nm) transitions, perturbed by low pressure (below 1 torr) helium, argon and xenon gas. One series of experiments measured the collision cross section for optical coherence destroying collisions, and the results obtained are in good agreement with previous two pulse echo measurements. The remaining experimental work determined values of collision cross sections due to depolarising collisions for ground state caesium atoms perturbed by noble gas. This marks the first measurement of this parameter for $6S_{\frac{1}{2}}$ ground state caesium atoms.

Contents

List of Figures

List of Tables

Acknowledgements

First I would like to thank Dr Alan Durrant and Dr Joy Manners who conceived and supervised this research, the funding for which was provided by SERC and the Open University. I would also like to thank Marilyn Moffat, Steve Daniels, Simon Rae, Dave Meara, Ian Trimnell and Richard Adams, all of the academic computing service, who managed to smooth out the hiccups encountered in producing this manuscript. I also wish to thank the Physics Department technical and support staff, Nobby Lowndes, Roger Bence, Martin Sydee, Yvonne McKay and Mandy Musgrave for their invaluable assistance. In addition I should like to express my gratitude to all the many friends who have helped me in one way or another while I have been writing up.

Last of all, I should like to thank my family, especially my parents, for all their encouragement, support, help and patience over the years.

Prologue

The main purpose of this work was the study of collisional parameters for the $6S_{\frac{1}{2}} \leftrightarrow 7P_{\frac{1}{2}}$ and $6S_{\frac{1}{2}} \leftrightarrow 7P_{\frac{3}{2}}$ caesium transitions perturbed by noble gases, using optical echoes. The particular technique employed was the three excitation pulse photon echo. Since this work followed on from the two pulse photon echo work done by Godfrey [1], three pulse echo experiments were conducted in order to measure the same collision cross sections studied by Godfrey, in order to check that the three pulse photon echo technique gave consistent results. In addition to these experiments, other three pulse echo experiments were undertaken which were concerned with the study of collisional parameters which could not be obtained using the two pulse photon echo technique.

This thesis is arranged on the following lines:

Chapter 1 begins with an outline of collision broadening theory, before going on to discuss both frequency domain spectroscopy and time domain spectroscopy. Two and three pulse photon echoes are introduced with reference to the Bloch vector model. This model is a pictorial, three dimensional representation of the echo formation process in a two-level system, and has been chosen because of its simplicity and clarity. The discussion of the photon echo process is then extended to degenerate two-level systems (real systems). The last part of this chapter outlines the photon echo experiments performed for this thesis.

Chapter 2 contains a survey of two- and three–pulse photon echo work performed by various researchers.

Chapter 3 contains a description of photon echo formation using density matrices. Whilst this method is not as simple or as accessible as the Bloch vector model, it does have the advantage that it can be applied to multi-level atoms excited by a sequence of excitation pulses.

Chapter 4 contains a description of the equipment used in the photon echo experiments.

Chapter 5 is concerned with the calibration of various pieces of the equipment.

Chapter 6 describes the procedure for the photon echo experiments and contains the main results of this thesis. The theory of how collisional information is obtained from the experiments is discussed. The experimental results are discussed and comparisons made with previous work where applicable.

Chapter 1

Introduction to collisional effects on coherently radiating atoms.

This section is concerned with radiating atoms collisionally perturbed by atoms of a foreign gas which is present at very low pressures, where the atomic density of the radiating atoms is sufficiently low that resonant collisions can be neglected. It is assumed that only elastic collisions occur, and that both the binary approximation (that collisions only involve one radiating atom and one foreign gas atom) and the impact approximation (that the time during which a collision takes place is much shorter than the interval between collisions) hold. Collisional effects on radiating atoms manifest themselves either as broadening or shifts of a spectral line in the case of frequency domain spectroscopy, or as a reduction of coherence in the case of time domain spectroscopy. Study of the spectroscopy of these atoms thus yields information about the collisional processes taking place.

Spectral line-shapes and their associated broadening mechanisms are reviewed by many authors, with those by Bransden and Jochain [2], Yariv [3] and Thorne [4] being reasonably comprehensive accounts. Section 1.1 contains a brief discussion of spectral line broadening mechanisms, whilst Section 1.2 outlines a selection of frequency domain and time domain experiments and discusses their relative merits with respect to the information that can be obtained from them. Section 1.3 describes photon echo formation in two level atoms via the Bloch vector model. Section 1.4 considers

echo formation in real, degenerate two level systems, and Section 1.5 outlines the experiments performed in this thesis.

1.1 Spectral broadening mechanisms in gases.

A single atom will, to a good approximation, only absorb and emit radiation at reasonably well defined frequencies, giving rise to spectral lines for absorption and emission. Closer inspection of these spectral lines reveals that they are not single valued, but rather contain a spread of frequencies, with the intensity of the spectral line varying across this frequency range. Thus the spectral lines are broadened, with the shape or profile of the line dependent upon the line broadening mechanisms present. Spectral line broadening can be broadly divided into two categories, namely homogeneous broadening and inhomogeneous broadening.

1.1.1 Homogeneous broadening.

Homogeneous broadening is characteristic of *all* atoms in a sample. In low pressure gases there are two main possible homogeneous broadening processes: radiative (or natural line) broadening and pressure broadening. Radiative broadening can be explained in terms of Heisenberg's uncertainty principle as applied to the transition lifetime — uncertainty in the transition time corresponds to uncertainty in the transition frequency. Radiative broadening exhibits a Lorentzian profile of half width at half maximum (hwhm) given by

$$\delta\nu_{rad} = \frac{1}{4\pi\tau_0}$$

where τ_0 is the natural lifetime for the transition and the hwhm is measured in Hz. Typically, τ_0 for electronic transitions is in the region $10^{-8} - 10^{-6}$ s, giving $\delta\nu_{rad} \simeq 0.1$ MHz - 10 MHz. This represents a very narrow broadening, and it is usually swamped by other broadening mechanisms.

Pressure broadening in a low pressure gas is the result of collisions which cause a loss of atoms from the radiating transition (inelastic collision) or,

for elastic collisions, a loss of phase information of the atomic dipole moment. Thus, the coherence of the radiation from the atom is maintained, on average, only for a time of τ_c, where τ_c is the mean time between collisions. Hence the line profile is broadened as a Lorentzian of hwhm given by

$$\delta\nu_{press} = \frac{1}{2\pi\tau_c}$$

As the gas pressure increases, τ_c decreases, resulting in an increase of the broadening of the profile. At higher pressures asymmetries and shifts can develop in the spectral line-shape, though this work is not concerned with high pressure effects.

1.1.2 Inhomogeneous broadening.

The main inhomogeneous broadening process that occurs in gases is that of Doppler broadening resulting from the motion of the atoms. Excited atoms radiate in the laboratory frame at frequencies given by

$$\nu_{obs} = \nu_0(1 + \frac{v_z}{c}) \quad \text{for } \frac{v_z}{c} \ll 1$$

where ν_{obs} is the frequency seen by an observer looking in the negative z-direction, ν_0 is the transition frequency and v_z is the z-component of the atom's velocity. The shape of the Doppler broadened profile is Gaussian, with a hwhm given by

$$\delta\nu_{Dopp} = \frac{\nu_0}{c} u\sqrt{\ln 2}$$

where u is the radiating atom mean speed given by $u = \sqrt{\frac{2k_BT}{m}}$, k_B is Boltzmann's constant, T is the absolute temperature and m is the atomic mass.

Any broadened line profile is likely to be a convolution of the three broadened line-shapes. The resultant line-shape is called a Voigt profile (see Figure 1.1), and it is essentially composed of a central region which is near-Gaussian in shape, with a Lorentzian profile which is more discernable in the wings. Typically, Doppler broadening has a fwhm of $\approx$ 1 GHz, whereas the fwhm of the Lorentzian is of order 1 MHz. The mechanism of Doppler

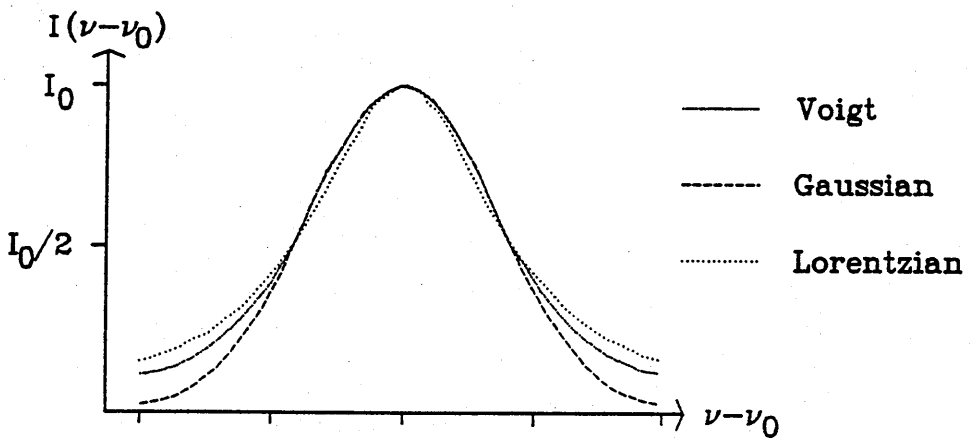

Figure 1.1 The Voigt profile.

broadening is well understood, whereas that for pressure broadening is much more complex. In order to study the collisional effects due to pressure broadening alone, which can give information on interatomic potentials, it is necessary to remove the Doppler broadening since it normally swamps pressure broadening, and many experimental techniques have been devised which achieve this. The next section gives a brief description of the major methods adopted.

1.2 Experimental techniques to study collisional effects in gases

Many line broadening experiments have been devised to study collisional effects, and this section outlines some of the more widely used techniques. In addition to frequency domain studies, time domain experiments have been devised, which look at the effects of collisions on the optical coherence. This form of spectroscopy is often referred to as 'coherent optical transient spectroscopy', and this section also contains a brief description of some time domain experiments.

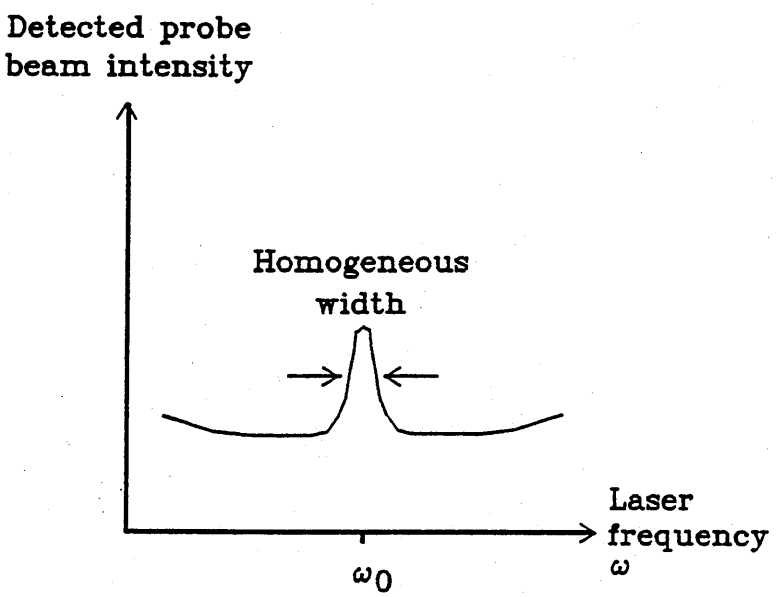

Figure 1.2 The type of profile obtained from a saturating absorption experiment.

1.2.1 Line broadening experiments.

There are two methods by which the effects of Doppler broadening can be circumvented. The first of these is to work at pressures which are sufficiently high that the shape of the profile, at least in the wings, is dominated by pressure broadening. Experiments using this method have been conducted using alkali and alkali-earth vapours perturbed by noble gases [5] [6] [7]. Traditionally these have used diffraction gratings or interferometers to measure the spectral profile, either in emission or absorption. However at these pressures the binary and impact approximations are no longer strictly valid. These experiments will not be discussed further. The second method is to work at low pressures using 'Doppler-free' techniques. Saturation spectroscopy and two-photon absorption spectroscopy are two such techniques, where the effects of Doppler broadening are substantially reduced or even eliminated from the spectral profile.

In saturation spectroscopy, a saturating laser beam is passed through a

sample of gas. A very small part of the emergent beam is back-reflected through the sample, so that this lower intensity 'probe' beam and the saturating beam are counter propagating. After passing through the sample, the probe beam is directed to a detector. The saturating beam frequency, and hence the probe beam too, is then swept through the line profile of the sample. When the beam is far from the line centre, only those atoms which have large velocities will be Doppler shifted into resonance with the saturating beam. The probe beam can interact only with those atoms with the opposite Doppler shift and is absorbed by them. As the laser is tuned nearer to the central resonant frequency, it interacts with atoms with progressively smaller Doppler shifts, the number density of which increases as the detuning decreases and hence the probe beam is absorbed more. However, when the laser is tuned within the *homogeneous* linewidth, the saturating and probe beams interact with the same velocity set of atoms, thus the attenuation of the probe beam is reduced, since the absorption has been saturated by the intense saturating beam. Figure 1.2 gives a schematic representation of typical saturation absorption experiment profile. Many experiments have been conducted using this technique to study such things as the Lamb shift in the H_α hydrogen line [8], as well as broadening produced by various collision mechanisms [9], [10], [11], [12].

The two photon absorption technique again uses counter propagating laser beams, but in this case they are of equal intensity, and are tuned to half the transition frequency under study. The selection rules for two photon absorption ($\Delta l = 0, \pm 2$) mean that only electric dipole forbidden transitions can be studied by this method. When an atom passes through the beams then, to first order, the light from each beam is Doppler shifted by equal but opposite amounts in the atom's frame of reference. When the laser is tuned to within the homogeneous linewidth, any atom can absorb one photon from each beam. This is true for all velocities, resulting in a much higher signal-to-noise ratio in the line-shape measurements than is possible for saturation spectroscopy. Figure 1.3 shows the profile for a typical two

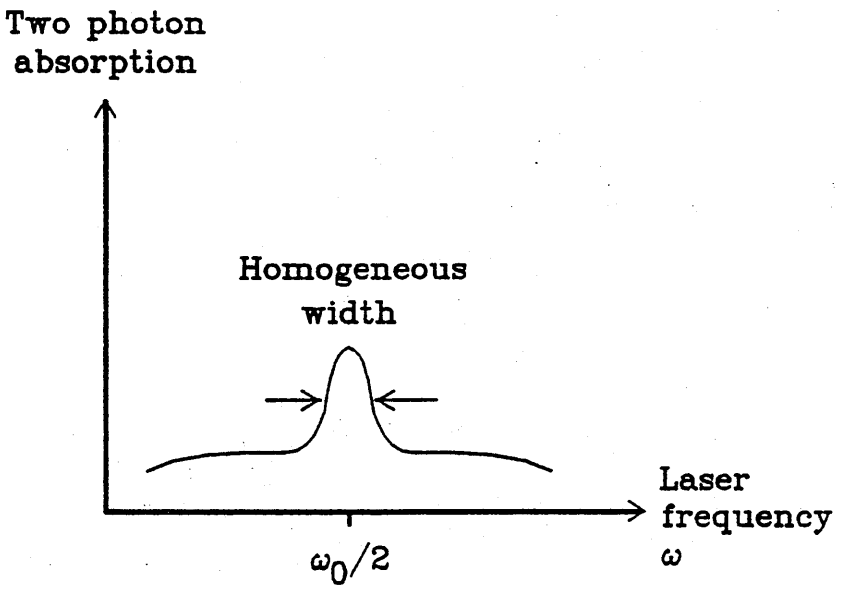

Figure 1.3 The type of profile obtained from a two photon absorption experiment.

photon absorption experiment. When the laser frequency is varied, the corresponding absorption profile is not Doppler broadened. However, the probability of two-photon absorption by an atom is very small unless the atom has an intermediate energy level nearly half way between the two levels under study. Biraben et al [13] have studied collisional effects of perturber atoms on the $3S \leftrightarrow 5S$ and the $3S \leftrightarrow 4D$ transitions of sodium using the two photon absorption technique.

1.2.2 Coherent optical transient spectroscopy.

Collision mechanisms can be studied by Doppler-free experiments in the time domain as well as in the frequency domain. There are three main coherent optical transient effects used in time domain spectroscopy, these being optical nutation, free induction decay and photon echoes. Reviews of the theory and early work are given by Shoemaker [14] and Allen and Eberly [15].

Optical nutation occurs when a sample is subjected to a stepwise res-

onant optical field. Atoms in the ground state absorb radiation and are excited to the upper level, whereupon they are immediately stimulated to emit by the applied optical field. Consequently, the atoms return to the ground state and can again absorb radiation, causing the process to repeat itself with the result that the absorption is sinusoidally modulated. The alternating absorption and stimulated emission of radiation from the sample is called optical nutation, and this process is the optical analogue of the nmr phenomenon of transient nutation [16]. The manner in which the sinusoid is damped out gives information about the relaxation processes i.e. spontaneous decay and collisional effects. Optical nutation was first seen in SF_6 using a Q-switched CO_2 laser as the resonant source [17].

Free induction decay (FID) refers to the radiation emitted by atoms after they have been excited by a pulse. Suppose that an atom is excited by a coherent resonant pulse to a superposition of its ground and excited states. If a sample contains a number of such atoms then a phased array of oscillating dipole moments in the sample results. When the excitation pulse is turned off, the atomic dipoles continue to oscillate and the sample radiates a macroscopic optical field which is coherent with the applied pulse. The oscillations are again damped out by spontaneous decay and collisional effects. However, in the case of a gas, thermal motions cause the radiation emitted by the individual atoms to be Doppler shifted, with the result that the atoms in the sample lose their coherence, and the sample's observed emission is seen to rapidly decay in intensity. This rapid decay of the coherence of an ensemble of atoms immediately after an excitation pulse is called free induction decay. The FID occurs in a period of approximately $\Delta\omega^{-1}$, where $\Delta\omega$ is the range of frequencies excited by the applied optical pulse. If the whole Doppler profile is excited then $\Delta\omega = \delta\nu_{Dopp}$. Measurements of collisional decay have been carried out quite successfully in the microwave region [18], where the FID process is not too rapid to be observed. At optical frequencies, however, the FID process is considerably shorter, and for experiments in which the whole of the Doppler linewidth is excited, the FID time is of order 1 ns, which is often considerably shorter than the excitation

pulses available. With the advent of picosecond pulse duration lasers optical FID may be fruitfully investigated.

In photon echo experiments a sequence of two or more excitation pulses are applied to a sample. The sample emits an FID pulse after each pulse as expected, but in addition other pulses, called echoes, are emitted at other times. This thesis uses the photon echo technique to measure the collision cross sections of caesium-noble gas atom interactions. The next section describes the process of photon echo formation and the effects of collisions on it.

1.3 Photon echoes and collisional effects.

This section is divided into four subsections. Subsection 1.3.1 contains a brief introduction to the two pulse photon echo, whilst Subsection 1.3.2 introduces the Bloch vector model, and goes on to use this to describe the two pulse photon echo process. Subsection 1.3.3 is concerned with three pulse photon echo formation, and Subsection 1.3.4 describes the effects of collisions on both two and three pulse photon echoes.

1.3.1 Two pulse photon echoes

The photon echo is the optical equivalent of the magnetic spin echo encountered in nuclear magnetic resonance experiments, with the latter being first observed by Hahn [19] in 1950. In Hahn's experiment, an ensemble of nuclear spins contained in a liquid and placed in an external magnetic field, was subjected to a sequence of two short, intense, rf pulses, which were separated by a time τ. At a further interval τ after the second pulse had been applied the spin ensemble produced a spontaneous magnetic moment.

The explanation for this effect is based on the presence of inhomogeneities in the local magnetic field experienced by the individual spins. When the first pulse is applied, all of the spins in the sample are aligned by the pulse. As soon as the pulse ends, the individual spins are free to precess in the external magnetic field. However, because of inhomogeneities present

in this magnetic field, they precess at different rates, with the result that the macroscopic magnetic moment of the ensemble decays as the magnetic moment vectors of the individual spins become dephased with respect to one another. This dephasing process is the spin equivalent of the FID phenomenon mentioned in Subsection 1.2.2, and the spins will remain dephased if the system is left in this condition. The second excitation pulse, however, reverses the relative phases of the precessing spins, thereby initiating a reversal of the FID process, so that the dephasing which occurred during the period τ between the first and second excitation pulses is reversed after the second excitation pulse, with the rephasing process being complete at time $t = \tau$ after the second excitation pulse. Since the ensemble spins are all aligned when the phase reversal process is complete, there is a macroscopic magnetic moment which is observed as a spontaneous nuclear induction signal, which has been termed a 'spin echo'. However, the individual spins continue to precess at their respective rates, so the nuclear induction signal is only a transient effect. If the excitation pulse widths are sufficiently short in duration (i.e. less than $\approx \delta\omega^{-1}$ where here $\delta\omega$ is the spread of the precession frequencies of the spins) then the echo duration is simply twice the FID time.

In the case of photon echoes, a pulsed laser acts as the excitation source, and it is the dephasing and rephasing of the atomic or molecular electric dipole moments in an inhomogeneously broadened sample which constitutes the echo formation process. Photon echoes have been observed in both solids and gases, and the inhomogeneity essential for the FID (and hence echo formation) can be caused by crystal field lattice strains in the case of some solids, and Doppler broadening in the case of gases.

Theoretical treatments of the spin echo and the two pulse photon echo are based on the same underlying mathematics, since they are both generated by assemblies of two-state systems. Both types of echo can be described graphically with reference to Bloch vectors, which represent the quantum state of the system and give a three dimensional visualisation of the time evolution of the system when it is excited by a resonant pulse or a sequence

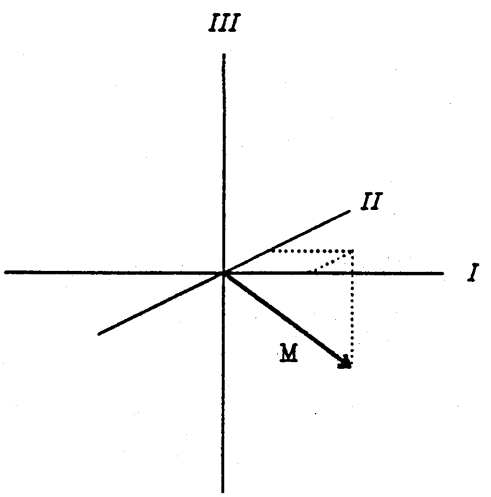

Figure 1.4 The Bloch vector representation of a two level atom. The I and $-II$ axes represent the in-phase and in-quadrature components of the electric dipole moment respectively, whereas the III axis represents the inversion.

of resonant pulses. The major part of this chapter is devoted to the Bloch vector description of photon echoes formed in gases. More detailed discussions of the Bloch vector and its relationship to the optical Bloch equations are given in many treatises: those by Shoemaker [14], Allen and Eberly [15], and Feynman et al [20] are very clear accounts. Other diagrammatic treatments of photon echoes can be found in papers by Mossberg et al [21], Beach et al [22] and Durrant et al [23].

1.3.2 The Bloch vector picture of two pulse photon echo formation.

The state of a two level atom can be represented pictorially by means of the Bloch vector, which is denoted by M. M has components $(\mathrm{M}_I, \mathrm{M}_{II}, \mathrm{M}_{III})$ as shown in Figure 1.4, where the I and $-II$ axes represent respectively the in-phase and in-quadrature components of the atomic dipole moment with respect to the E field of the applied optical excitation pulse, and the III axis represents the population inversion of the atom. Normalisation of the atomic state requires that M is of unit length. Thus, an atom which is in

its ground state is represented by the Bloch vector M=(0,0,-1), whilst an atom which is in its excited state is represented by M=(0,0,1).

The atomic dipole moment components, M_I and M_{II}, are the slowly varying amplitudes, with the oscillations at the laser driving frequency removed. This is equivalent to observing a precessing spin system in the 'rotating frame' i.e. rotating at the centre of line frequency (see reference [15] for example). It follows from the optical Bloch equations [14] [15] that the time-dependence of M is determined by the equation

$$\frac{d\mathrm{M}}{dt} = \mathrm{M} \wedge \Omega \tag{1.1}$$

which describes the precession of M in a cone about Ω, where Ω is a generalised driving field with components $\Omega = (\kappa E_0, 0, \Delta\omega)$, where E_0 is the amplitude of the applied laser field, $\kappa = \frac{d_{12}}{\hbar}$ where d_{12} is the electric dipole moment matrix element for the transition. κE_0 is the Rabi flipping frequency. $\Delta\omega$ is the detuning of the atom's resonance frequency from the laser frequency. Assuming that the laser is tuned to the centre frequency ω_0 of the inhomogeneously broadened line and that the laser pulse propagates in the z direction, then, for a particular atom with velocity component v_z in the z direction, $\Delta\omega = kv_z$ where k is the wavenumber of the laser pulse $(= \frac{2\pi}{\lambda})$. Figure 1.5 shows the precession of M about Ω for an atom initially in the ground state which is driven off resonance (i.e. $\Delta\omega \neq 0$), and Figure 1.6 shows the behaviour of M when the atom is driven resonantly (i.e. $\Delta\omega = 0$). The Bloch vector M rotates in the $II - III$ plane at the Rabi flipping frequency. It is assumed that for a Doppler broadened assembly of atoms a resonant pulse satisfies the condition $\kappa E_0 \gg \Delta\omega$ for all v_z, so that $\Delta\omega$ can be neglected in comparison to κE_0 for all atoms in the sample. Thus, when the pulse acts, Ω has components $\Omega = (\kappa E_0, 0, 0)$ and the inhomogeneous broadening is neglected.

In most echo experiments, includung those conducted for this thesis, $\Delta\omega > \kappa E_0$. However an echo is still formed. The echo is smaller than it would be if all atoms were excited resonantly, and the echo width is slightly

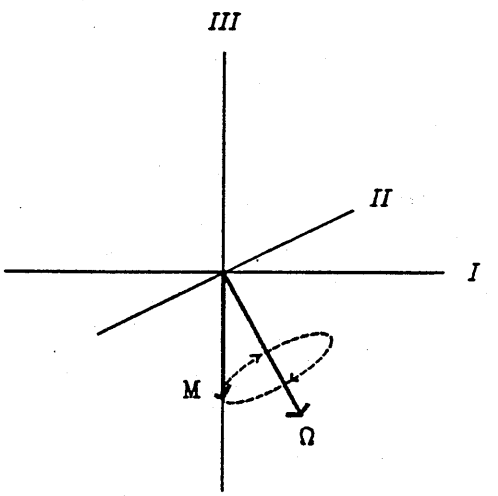

Figure 1.5 The Bloch vector representation of a two level atom driven off resonance.

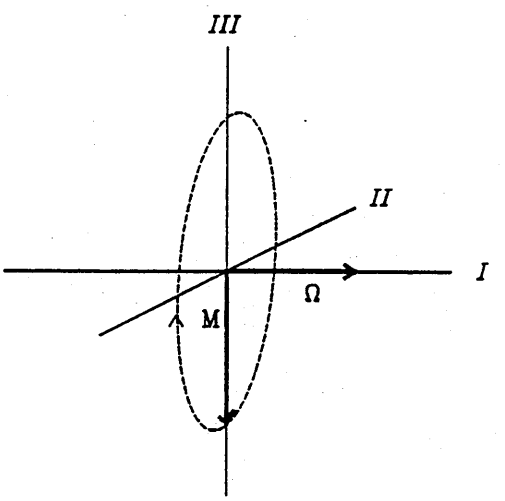

Figure 1.6 The Bloch vector representation of a two level atom driven on resonance from the ground state. The vector M precesses in the $II - III$ plane at the Rabi frequency.

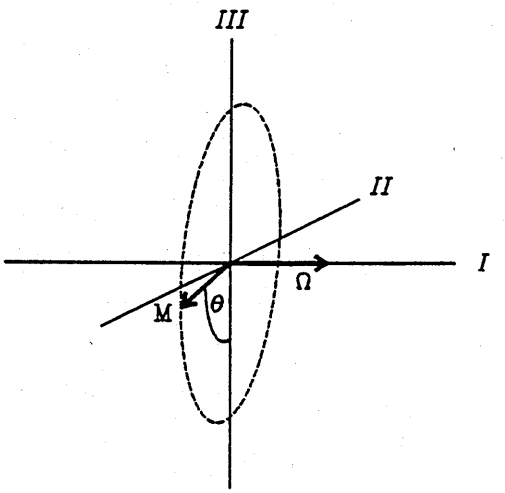

Figure 1.7 The effect of a resonant θ pulse acting on a ground state, two level atom: note that the Bloch vector M is rotated about $-I$ through an angle θ.

longer and is delayed by an amount of order of a pulse width. Furthermore the collisional decay is bot affected [14].

When a resonant (optical) field is applied to the atom, the incident pulse can be characterised by the angle θ through which the Bloch vector M is rotated about the $-I$ axis; θ is called the pulse area, and a pulse of area θ is referred to as a θ pulse. Figure 1.7 shows the effect of a resonant 'θ' pulse on the M vector of a ground state atom.

In the two pulse echo experiment two collinear, resonant pulses with

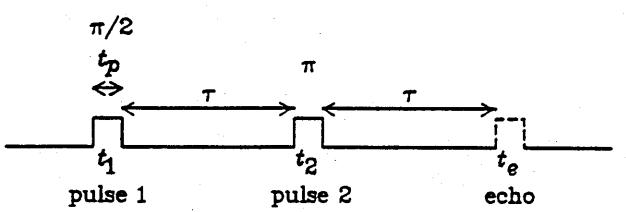

Figure 1.8 The pulse sequence employed in the two pulse photon echo experiment.

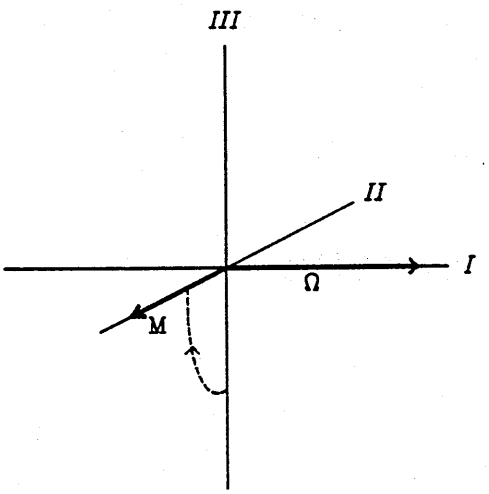

Figure 1.9 The effect of a resonant $\frac{\pi}{2}$ pulse acting on a ground state, two level atom.

different pulse areas and separated by a period τ, as shown in Figure 1.8, are applied to the inhomogeneously broadened sample. Ideally, the pulse areas are $\frac{\pi}{2}$ and π, as indicated in Figure 1.8. The atoms are initially in the ground state. Immediately after the resonant $\frac{\pi}{2}$ pulse, the Bloch vectors for all the atoms will lie along $-II$, representing the fact that each atom is in a superposition of its ground and excited states (with each state having an equal probability). Each individual dipole moment is entirely in quadrature with the driving field: Figure 1.9 shows this.

In order to describe the behaviour of the sample when the pulse is removed, one has to consider the effect of the inhomogeneity in the sample. When no pulse is being applied $\Omega = (0, 0, \Delta\omega)$, and the M vectors precess with frequencies $\Delta\omega$ about the III axis. Figure 1.10 shows this precession for the Bloch vectors of three different atoms initially aligned by the first pulse at time $t = 0$ along the $-II$ axis. M_0 is the Bloch vector for an atom with no detuning (hence $\Omega = 0$), and M_1 and M_2 correspond to $\Delta\omega_1 > 0$ and $\Delta\omega_2 < 0$ respectively. If the Bloch vectors are left to precess for a time τ then M_0 remains stationary, M_1 has moved through an angle $\Delta\omega_1\tau$ and M_2 has rotated through an angle $\Delta\omega_2\tau$ in the opposite sense, where $\Delta\omega_1$ and

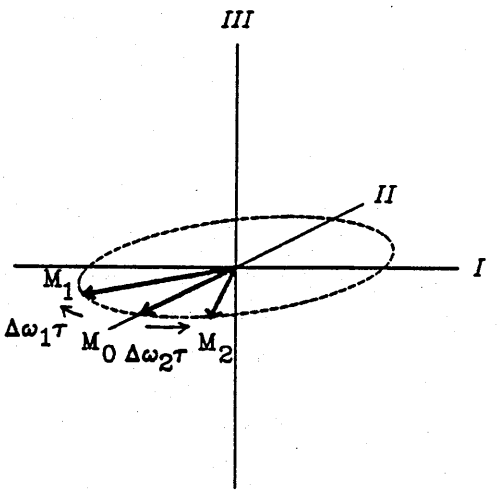

Figure 1.10 Precession of Bloch vectors at time τ after a resonant $\frac{\pi}{2}$ pulse has been applied to a ground state, two level atom. Note that the Bloch vectors are shown to have moved through small angles purely to aid visualisation.

$\Delta\omega_2$ are the corresponding detunings. Now consider an inhomogeneously broadened sample containing a very large number of atoms. Clearly, if the period τ is long compared with the FID time ($\Delta\nu_{Dopp}^{-1}$), then the individual Bloch vectors will be uniformly distributed throughout the $I - II$ plane, with the result that there is no overall macroscopic dipole moment.

When a second resonant pulse, this time a π pulse, is applied to the system at time $t = \tau$, its effect is to rotate each Bloch vector through an angle π about $-I$. The positions of the Bloch vectors immediately after the resonant π pulse are shown in Figure 1.11. The Bloch vector M_0 which, in Figure 1.10, was along the $-II$ axis immediately before the resonant π pulse was applied, is now along the II axis immediately after the pulse. Similarly M_1, which made an angle $\Delta\omega_1\tau$ to the $-II$ axis immediately before the pulse is applied, now makes an angle $\Delta\omega_1\tau$ to the II axis immediately after the pulse, as shown. The π pulse has effectively reversed the relative phases of the Bloch vectors, but it has not affected their precession rates or direction, since the driving vector for each atom, $\Omega = (0, 0, \Delta\omega)$, is the same after

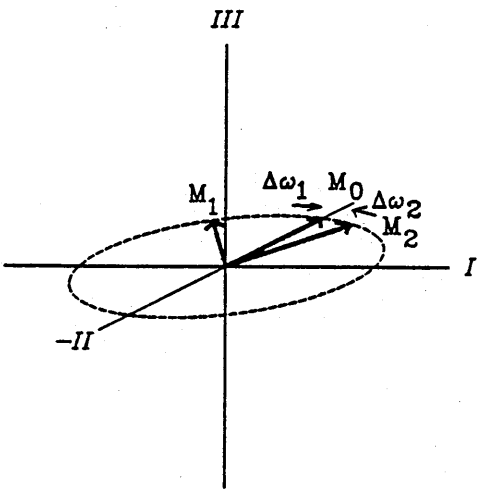

Figure 1.11 Position of the three Bloch vectors shown in the previous figure immediately after the resonant π pulse has been applied to the system.

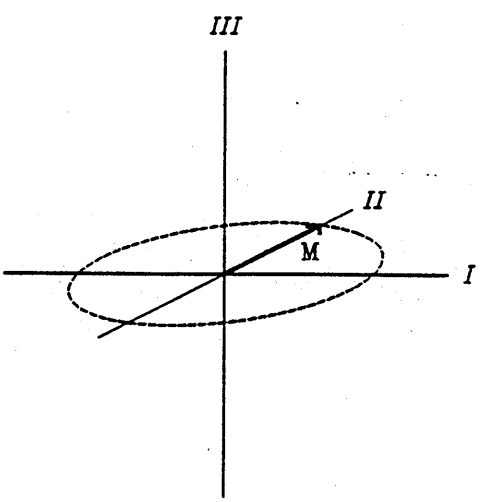

Figure 1.12 Phase reversal completed at time τ after the π pulse has been applied. All Bloch vectors lie along M.

the second pulse as it was between the pulses. Therefore, after the π pulse, the individual Bloch vectors rephase, with the rephasing process being complete when all the Bloch vectors are aligned along the II axis at time τ after the π pulse has been applied, as shown in Figure 1.12. This realignment of all of the Bloch vectors corresponds to a rephasing of all of the atomic dipole moments, with the result that there is a macroscopic dipole moment which produces the coherent optical pulse emitted by the sample; it is this pulse which constitutes the photon echo, which is of duration $2\Delta\omega^{-1}$.

1.3.3 Three pulse photon echoes — stimulated echoes

The previous section has shown, via the Bloch vector model, how a photon echo can be produced from a sequence of two resonant pulses. However, a photon echo of a different kind, called a stimulated echo, can also be produced from a sequence of *three* resonant excitation pulses on a two-level atom. The ideal pulse area sequence for this is a $\frac{\pi}{2}$, $\frac{\pi}{2}$, $\frac{\pi}{2}$ sequence, as shown in Figure 1.13. Since a π pulse has the same effect on the inversion as two contiguous $\frac{\pi}{2}$ pulses, replacing the second resonant pulse in the two pulse photon echo experiment (the π pulse) by two contiguous $\frac{\pi}{2}$ pulses will still cause a photon echo to be produced. Whilst this would seem obvious, it is perhaps less clear why a photon echo is still produced at time τ after the third pulse, when the second and third $\frac{\pi}{2}$ pulses are no longer contiguous but separated by a period T. The Bloch vector model can be used to describe how this stimulated echo is produced.

The first $\frac{\pi}{2}$ pulse is applied at time t_1 to ground state atoms, so that a

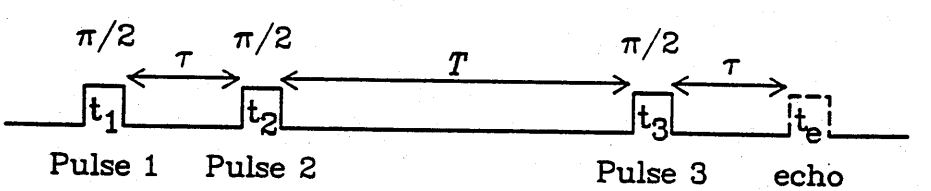

Figure 1.13 The excitation pulse/echo separation for a three pulse (stimulated) echo.

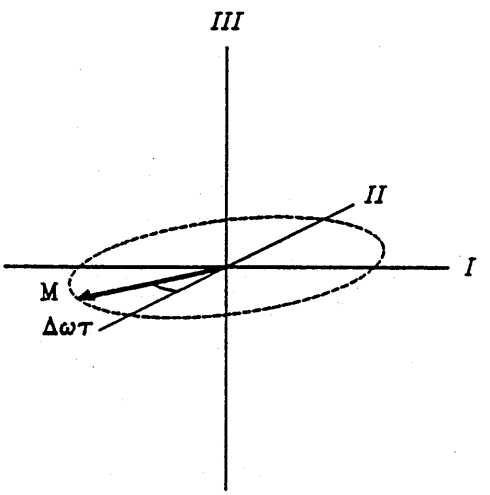

Figure 1.14 The position of a Bloch vector M following free precession during time τ after the first excitation pulse.

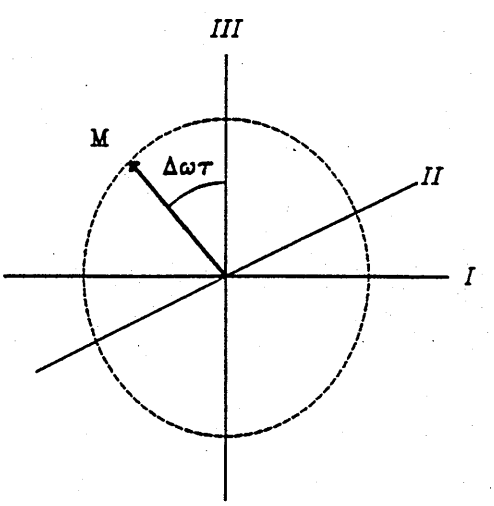

Figure 1.15 The position of the Bloch vector M immediately after the second excitation pulse at time τ after the first pulse. Note that the dotted circle in Figure 1.14, which was in the $I - II$ plane, has been rotated so that it lies in the $I - III$ plane.

typical Bloch vector M lies along the $-II$ axis immediately after the pulse has been applied. Suppose precession of a Bloch vector for a period τ ($\tau \gg$ the FID time) after the first pulse causes M to lie in the $-I, -II$ quadrant at an angle $\Delta\omega\tau$ to the $-II$ axis, as shown in Figure 1.14. If a second $\frac{\pi}{2}$ pulse is applied at time $t_2 = t_1 + \tau$, then immediately after the pulse, M lies in the $I - III$ plane at an angle $\Delta\omega\tau$ to the III axis, and this is shown in Figure 1.15.

After the second pulse, M again precesses about the III axis so that its motion describes the surface of a cone of half angle $\Delta\omega\tau$, shown in Figure 1.16. If one resolves the Bloch vector into two components, the inversion W along the III axis and a component D initially along the $-I$ axis, as shown in Figure 1.17, then W remains fixed whilst D rotates in the $I - II$ plane with angular velocity $\Delta\omega$. Thus, for an assembly of atoms, the D components 'fan out' in the $I - II$ plane. However, W for each Bloch vector remains fixed and it is the subsequent time evolution of this component that will give rise to the stimulated echo.

The third $\frac{\pi}{2}$ excitation pulse is applied at time t_3 where $t_3 = t_2 + T$, and causes the components W for all atoms to lie along the II axis, as shown in Figure 1.18. After the third pulse, the components W precess in the $I - II$ plane about the $-III$ axis and at time $t_e = t_3 + \tau$, the stimulated echo time, W lies in the $+I, +II$ quadrant of the $I - II$ plane, at an angle $\Delta\omega\tau$ to the II axis — see Figure 1.19.

To appreciate why an echo is formed at this time, it is necessary to look again at the Bloch vector depicted in Figure 1.14. M not only represents the Bloch vector of an atom which has precessed through the angle $\Delta\omega\tau$, but it also describes a whole group of atoms with detunings given by $\Delta\omega_n = \Delta\omega + \frac{2n\pi}{\tau}$, where $n = 0, \pm1, \pm2, ...$ All members of the group were aligned at $t = t_1$ and were aligned again at $t = t_1 + \tau$. Thus, provided their velocity components v_z remain unchanged, the time τ represents a rephasing time for the members of this group. Since Figure 1.18 shows the position of the inversion component W for all atoms immediately following the third pulse,

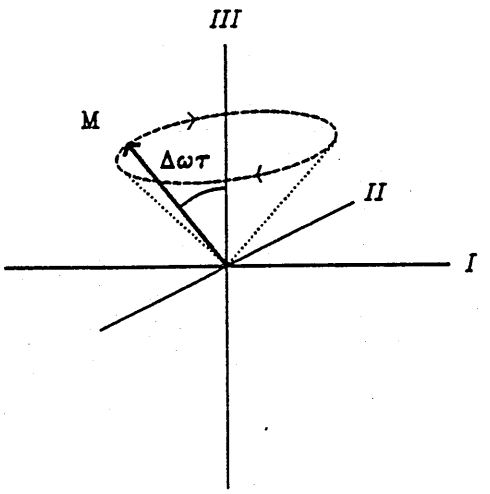

Figure 1.16 Precession of the Bloch vector M after the second excitation pulse.

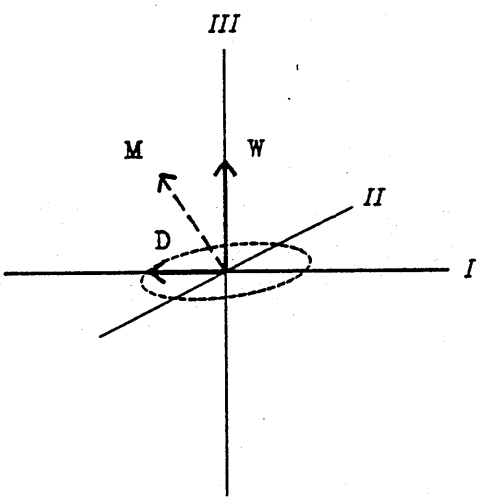

Figure 1.17 The Bloch vector M can be resolved into two components, W along the III axis, and D initially along the $-I$ axis.

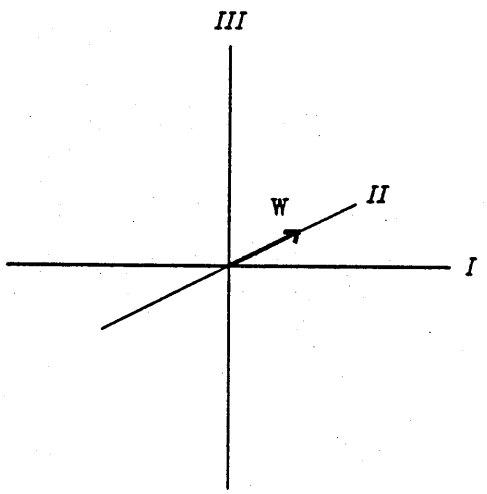

Figure 1.18 Position of the inversion components W of all atoms immediately after the third excitation pulse has been applied.

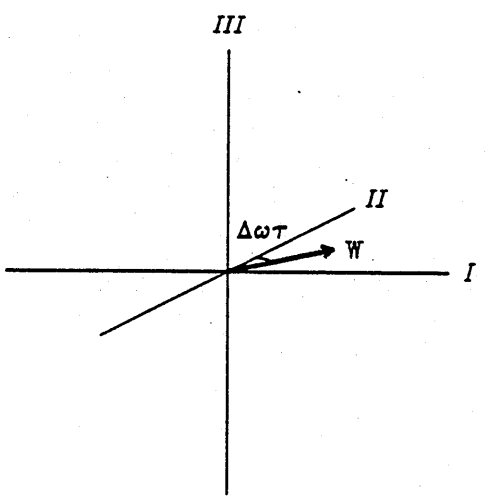

Figure 1.19 The position of a typical inversion component, W, at the echo formation time.

all members of all groups are aligned at this time and they subsequently dephase. However, at time $t_3 + \tau$ the members of each group rephase, with the different groups rephasing at different angles $\Delta\omega\tau$ in the I, II quadrant. It will be recalled that up to now only the behaviour of those Bloch vectors that were in the $-I, -II$ quadrant at time $t_1 + \tau$ has been considered. In fact, for atoms whose Bloch vector precession in the time τ between the first and second pulses causes them to be displaced within $\pm\frac{\pi}{2}$ from the $-II$ axis, then immediately after the third pulse has been applied the inversion component, W for all of these atoms lies along the $+II$ axis. Consequently, at time $t = t_3 + \tau$ all of the inversion components, W, again lie within a net angular displacement of $\frac{\pi}{2}$ from the $+II$ axis. Similarly, for those atoms whose Bloch vectors precess in time τ after the first pulse through a net angular displacement such that they lie within $\pm\frac{\pi}{2}$ with respect to the $+II$ axis, immediately after the third excitation pulse their inversion components W all lie along the $-II$ axis. Thus at time $t = t_3 + \tau$ each W lies within $\pm\frac{\pi}{2}$ of the $+II$ axis. Hence at time $t = t_3 + \tau$ the W components for *all* atoms lie within $\pm\frac{\pi}{2}$ of the $+II$ axis, resulting in a net macroscopic dipole moment. This net macroscopic moment at time $t_3+\tau$ is the stimulated echo. Note that since different groups are not all aligned at the echo formation time the stimulated echo will be smaller in intensity than the two excitation pulse echo.

1.3.4 Collisional effects on echo formation

So far this chapter has discussed the mechanisms for echo formation for atoms whose only interaction is with the optical field produced by the laser

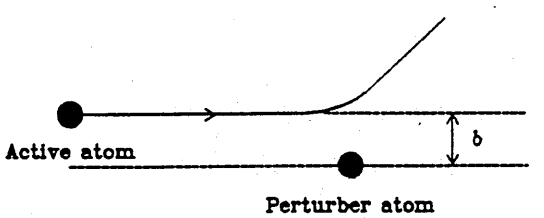

Figure 1.20 The impact parameter, b, for a collision involving two atoms.

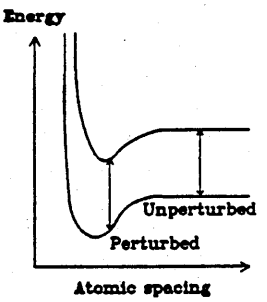

Figure 1.21 The variation of energy with atomic separation for two energy levels. The energy difference between the levels also changes with the atomic separation, giving rise to a change in the transition frequency.

pulses. It is now necessary to consider what happens when the echo forming atoms (active atoms) are subjected to one or more elastic collisions with perturbing atoms. Consider a collision with impact parameter b, as depicted in Figure 1.20. When a collision takes place between an active atom and a perturber atom , the velocity of the active atom is changed by some amount, as is the phase of the atom's dipole moment. The reason for the latter effect is that during a collision the atom's upper and lower energy states are usually perturbed by different amounts (see Figure 1.21), and so during the collision the atom's transition frequency varies slightly. When the colliding atoms are again well separated, the change in transition frequency during the collision manifests itself as a phase change in the atomic dipole moment.

If the impact parameter is small enough to produce a phase change of greater than π, the collision is classified as 'hard'. Otherwise the phase change is less than π and the collision is described as 'soft'. The impact parameter at which the phase change is exactly π is referred to as the Weisskopf radius, and is usually denoted by b_W. Generally, hard collisions result in a loss of phase coherence due to the impact and are referred to as *phase changing collisions* (pcc). In the Bloch vector model pcc can be represented by a large random displacement of the component of the Bloch vector in the $I - II$ plane to some other part of the $I - II$ plane. The result of this displacement is that the atom does not contribute to the echo, for at the echo

formation time the Bloch vector will not be aligned with those of uncollided atoms. In the case of soft collisions, the change in phase due to the impact is small, but the change in the velocity of the centre of mass of the atom has to be taken into account, as an atom which has undergone a velocity change will radiate at a different Doppler-shifted frequency in the laboratory frame, with the result that the atom will accumulate a phase change which will increase as the time after the collision increases, such that the larger the time after the collision, the smaller the velocity change necessary to accumulate a sufficient phase change. This is manifest in the Bloch spheres as a change in the precession frequency $\Delta\omega$ in the $I - II$ plane. Collisions of this type are called diffractive velocity changing collisions [24]. For hard collisions, the effect of collisional velocity changes are masked by the large random phase change during the impact. All collisions that destroy the phase coherence of the electric dipole moment of the atom, whether by impact or by velocity change, are called *optical coherence destroying collisions.* The two pulse echo described in Section 1.3.1 is attenuated by both types of optical coherence destroying collisions occurring at any time in the interval between the first excitation pulse and the echo.

The stimulated echo is also attenuated by both types of optical coherence destroying collisions during the two intervals $t_2 - t_1$ and $t_e - t_3$, when the relevant components of the Bloch vector are in the $I - II$ plane. However, in the interval between the second and third pulses the relevant components, W, are aligned along the inversion axis (see Figure 1.17) and are insensitive to the phase of the dipole moment. Thus, optical coherence destroying collisions occurring in the interval between the second and third pulses do not attenuate the stimulated echo. This allows the effects of other collision mechanisms, that are otherwise masked by optical coherence destroying effects, to be studied. In particular, this thesis utilises three pulse echoes to measure the cross sections for the collisional destruction of Zeeman coherences (depolarising collisions) in caesium by elastic collisions with noble gases, and to observe the effect of collisional velocity changes on the Zeeman

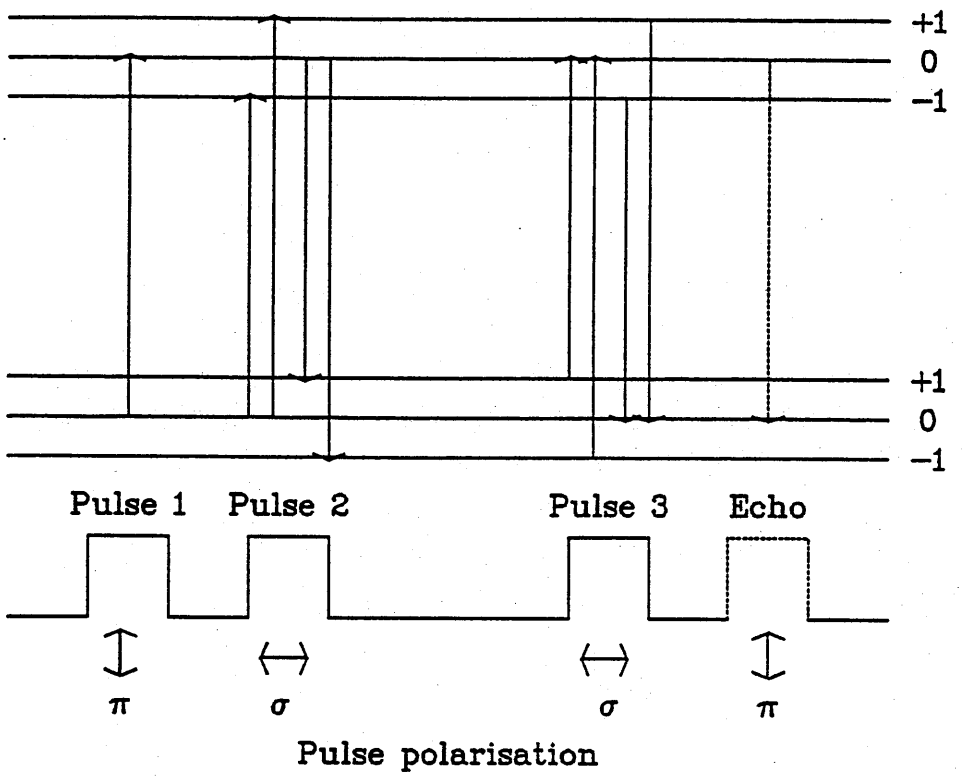

Figure 1.22 Echo formation from three linearly polarised excitation pulses acting on a degenerate, two-level system.

coherences.

1.4 Photon echoes in degenerate two-level systems.

Although the Bloch vector model is a useful construct in visualising the echo formation process it is, however, only applicable to a non-degenerate, two-level system. Of course, most real systems do not fall into this category. The case of three non-degenerate levels is discussed in detail in Chapter 3. A brief consideration of stimulated echo formation in a degenerate two level system is now given.

Suppose a degenerate, two-level system is subjected to three, linearly polarised excitation pulses, as shown in Figure 1.22 (which shows only three Zeeman sub-levels for simplicity). The first excitation pulse (a π-polarised pulse) forms an optical coherence between the ground and excited states, and again for simplicity only one $\Delta m = 0$ transition is shown. The second excitation pulse (a σ-polarised pulse) forms coherences between the Zeeman sublevels of both the excited and ground states, called Zeeman coherences. The third excitation pulse (another σ pulse) transfers the Zeeman coherences to an optical coherence between the ground and excited states. The resultant echo has the same linear polarisation as the first excitation pulse. In the interval between the second and third excitation pulses, the echo producing information resides only in the Zeeman coherences and components of orientation and alignment. The echo can therefore be attenuated in this interval only by collisions which destroy the Zeeman coherences either by 'depolarising' collisions or by collisional destruction of the velocity modulations (velocity-changing collisions) of components of orientation and alignment.

The experiments performed for this thesis use the pulse-polarisation scheme depicted in Figure 1.22 but different level schemes designed to investigate ground state and excited state Zeeman coherences respectively, and are outlined in the next section.

1.5 The photon echo experiments undertaken in this thesis.

The experiments were designed to measure the caesium-noble gas collision cross section for:

(i) destruction of optical coherence (phase changing and velocity changing collisions) on the $6S_{\frac{1}{2}} \leftrightarrow 7P_{\frac{3}{2},\frac{1}{2}}$ transitions;

(ii) destruction of Zeeman coherences (depolarising and velocity changing collisions) on the $6S_{\frac{1}{2}}$ ground state and the $7P_{\frac{3}{2}}$ state.

In addition, information is obtained on the velocity changing collision cross sections for the $6S_{\frac{1}{2}}$ ground state and the mean square velocity change per collision.

Three types of three-pulse echo experiments were performed, and the energy level diagrams and excitation pulse sequences for these experiments are shown in Figure 1.23.

(a) tri-level echo experiments specifically designed to isolate the collisional depolarising effects on the $6S_{\frac{1}{2}}$ ground state. The third pulse transfers the ground state coherences to the $7P_{\frac{3}{2}}$ level. The echo is then formed on the $6S_{\frac{1}{2}} \leftrightarrow 7P_{\frac{3}{2}}$ transition so that only the ground state Zeeman coherences are relevant. These experiments also gave the mean of the optical coherence cross sections for the $7P_{\frac{3}{2}} \leftrightarrow 6S_{\frac{1}{2}}$ and $7P_{\frac{1}{2}} \leftrightarrow 6S_{\frac{1}{2}}$ transitions;

(b) tri-level echo experiments specifically designed to isolate the collisional depolarising effects on the $7P_{\frac{3}{2}}$ excited state — see Figure 1.23(b). Only preliminary experiments were performed, and it was decided not to pursue them as the echo formed was too small to work with;

(c) stimulated echo experiments which in principle give the combined effect of collisional depolarisation in both the $6S_{\frac{1}{2}}$ ground state and the $7P_{\frac{3}{2}}$ excited state (in practice, however, because of the very small excited state echo it seems likely that this experiment only measured ground state effects).

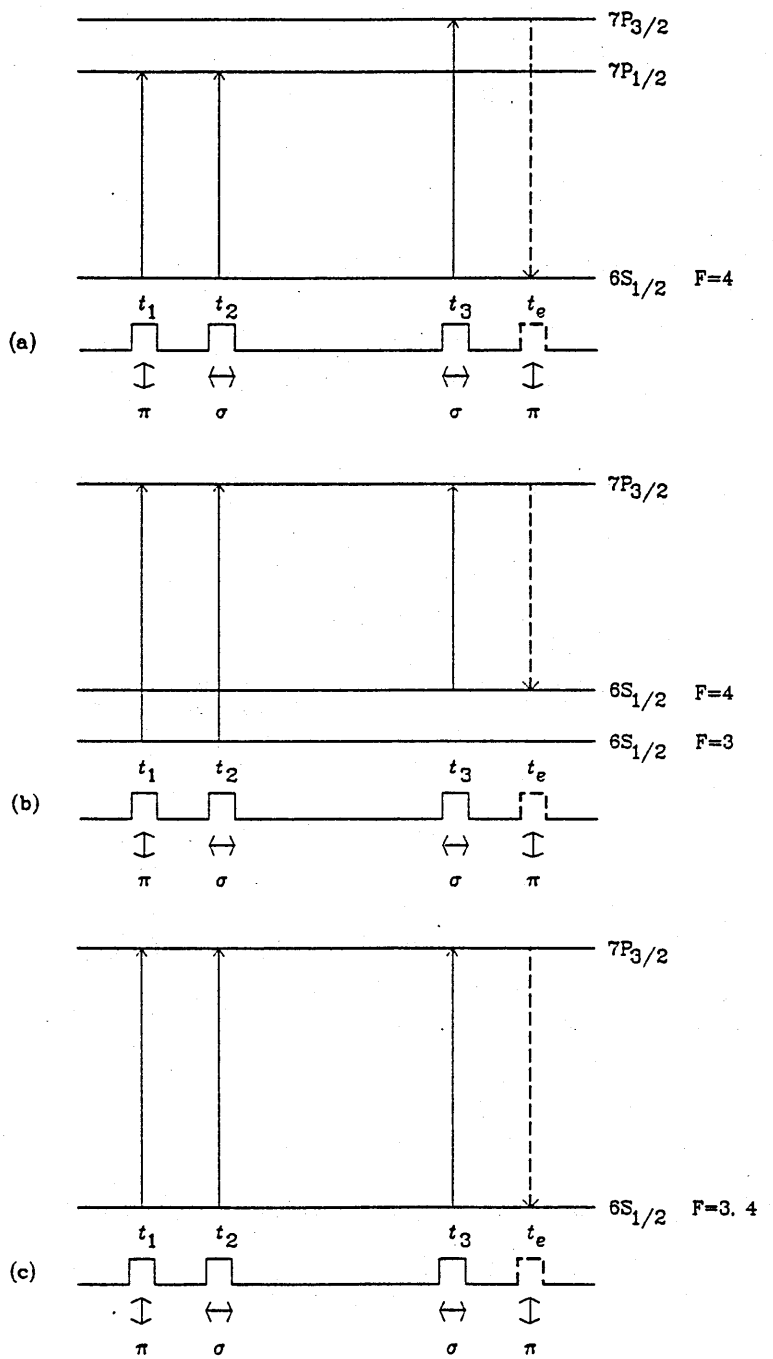

Figure 1.23 The excitation pulse sequence and the transitions involved for: (a) a tri-level echo experiment for ground state collisional depolarisation; (b) a tri-level echo experiment for excited state collisional depolarisation; (c) a stimulated echo experiment.

Chapter 2

A review of two and multiple pulse photon echo experiments.

2.1 The first photon echo experiments

Photon echoes were first observed by Kurnit et al [25] in 1964, who reported that a ruby crystal cooled to liquid nitrogen temperatures had been made to emit spontaneously a short, intense burst of radiation after being excited by two short, intense light pulses at 693.5 nm from a Q-switched ruby laser. The experimental arrangement employed is shown in Figure 2.1. In common with all echo experiments, a major difficulty was in detecting the weak echo signal without incurring saturation or damage to the detector due to the excitation pulses. Both Pockels cell electro-optic shutters and beam angling (spatial filtering) techniques were employed to this effect. Unfortunately, because of phase matching requirements [15], the echo intensity was found to decrease rapidly with the angle, ϕ, between the excitation pulses (see Figure 2.1) where ϕ was of the order of a few mrads. Further experiments with ruby [26] [27] investigated the echo intensity dependence upon the excitation pulse separation angle ϕ.

Scully at al [28] were the first to put forward the idea of photon echo formation in gases. They predicted that the echo forming conditions necessary would be similar to those encountered for a solid, with the addition that as the interpulse time increased, collisions would reduce the echo intensity in a

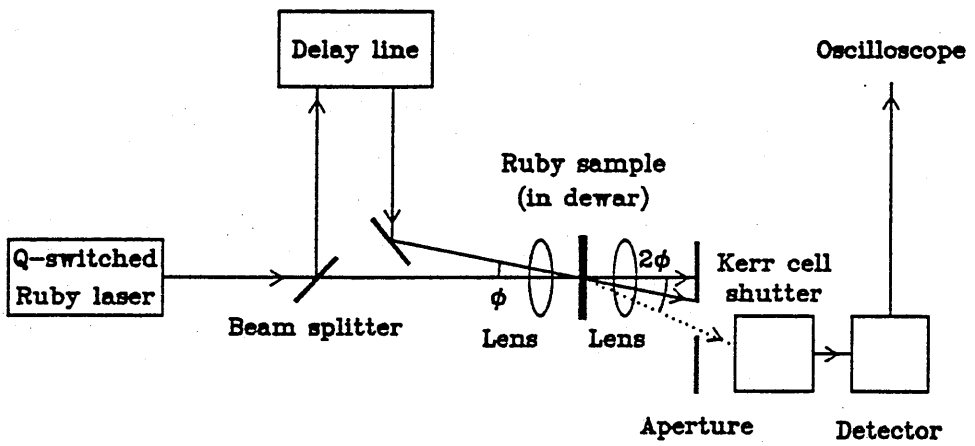

Figure 2.1 Experimental arrangement for the first photon echo experiment.

manner characteristic of the type of collision processes. Since photon echoes are free of the effects of inhomogeneous broadening, they therefore provide the basis of a Doppler free technique with which to study collisional effects on gases, and this has been the main use to which the photon echo technique has been put (however photon echo experiments are still being conducted in solids e.g. Rebane et al [29]).

As pointed out in Subsection 1.3.4, interatomic collisions can attenuate the echo intensity, with the attenuation produced in an experiment being dependent on both the interpulse time and the gas pressure. Two types of experimental procedure have therefore been adopted: those in which the gas pressure remains constant and the interpulse time is varied, and those in which the interpulse time remains fixed and the gas pressure is varied.

Photon echo experiments in gases can be further classified into two broad

categories: photon echoes formed on vibro-rotational transitions in molecular gases, (Subsections 2.2.1 and 2.2.2), and photon echoes formed on electronic transitions in atomic gases, (Subsections 2.3.1 and 2.3.2). From the late 1960's through to most of the 1970's, the most readily available excitation pulse source was the CO_2 laser. Although the lasing frequency was fixed at wavelengths near 10.59 μm, the existence was known of several molecular gases which had vibro-rotational transitions near this frequency which could be made resonant with the laser by Stark-shifting techniques [14]. It was not until the advent of the dye laser that photon echo experiments could be performed with atomic gases to investigate electronic transitions. Both two and multiple pulse echo experiments have been conducted in the two types of gases.

2.2 Photon echoes formed in molecular gases

2.2.1 Two pulse echo experiments

In 1968 Patel and Slusher [30] observed the first photon echo formed in a gas. The gas used was SF_6 (at a pressure of about 15 mtorr), and two separate CO_2 lasers provided excitation pulses of $\approx$ 200 ms duration. The laser frequency was resonant with one of the many vibro-rotational levels associated with the ν_3 transition. When a fixed pressure of a few mtorr of noble perturber gas were added, the relative echo intensity was observed to decay exponentially as the interpulse time was increased, with the rate of decay being a measure of the collision-induced homogeneous relaxation time (T_2') and hence dependent upon the particular perturber gas used. From their results Patel and Slusher were also able to calculate the inelastic collision cross sections for the particular levels excited, and in conjunction with Gordon et al [31] investigated the echo's intensity and polarisation, using linearly polarised excitation pulses whose polarisation planes were inclined at varying angles to each other. Polarisation effects have also been studied in SF_6 by other authors [32] [33].

In 1971, Brewer and Shoemaker [34] reported the observation of pho-

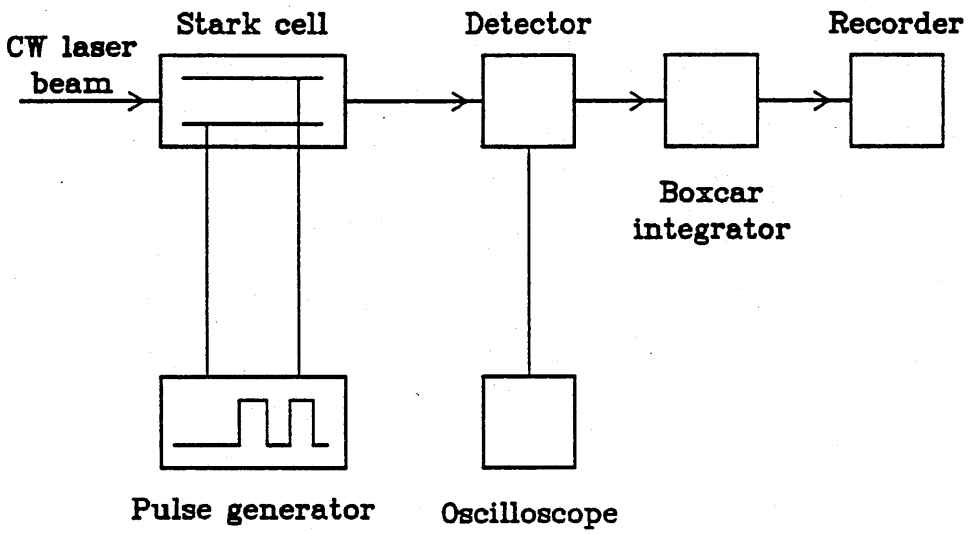

Figure 2.2 Block diagram showing the basic components of a Stark-switching experiment.

ton echoes in $^{13}CH_3F$ and NH_2D, using a novel technique called 'Stark-switching'. Figure 2.2 is a block diagram of the main components used in a Stark-switching experiment. In this technique, instead of using a pulsed, resonant laser to excite a transition, a cw laser is employed, with the molecular transition Stark shifted in and out of resonance in a pulsed manner. As well as opening up a much wider group of molecules which could be studied, this approach had the added advantage that the echo was detected through heterodyning the echo radiation with the much more intense cw laser radiation, resulting in much greater sensitivity. Brewer and Shoemaker's results for T_2' indicated that collisional relaxation for CH_3F–CH_3F collisions was primarily through rotational energy transfer. Further experiments using $^{13}CH_3F$ in which the interpulse time τ was varied [35] with the $^{13}CH_3F$

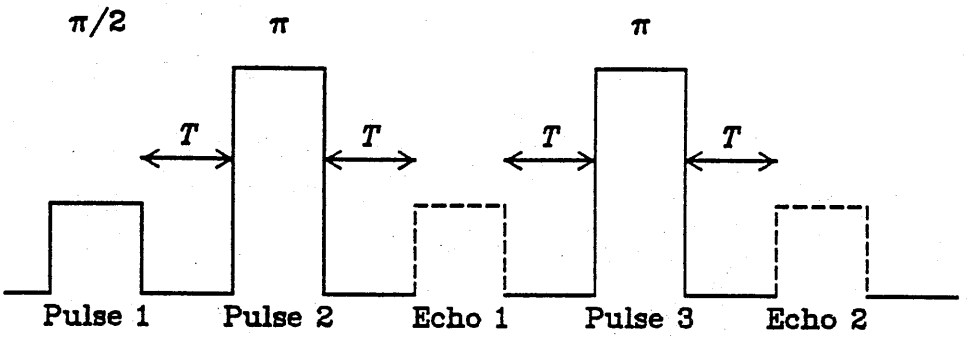

Figure 2.3 The Carr-Purcell echo train. Each time a π pulse is applied an echo is produced, with the maximum length of the Carr-Purcell train being dependent upon the inelastic collision and spontaneous decay rates.

pressure kept constant showed that the echo decay behaviour exhibited two distinct stages. At small τ the decay varied exponentially as $e^{-C\tau}$ (where C is a constant proportional to the collision rate), due to rotational energy transfer, while at large τ the decay varied as $e^{-D\tau^3}$. The change in the decay is due to the effects of velocity changing collisions, which are discussed in more detail in Section 6.3.

2.2.2 Multiple pulse echo experiments

Very few multiple pulse echo experiments have been performed using molecular gases, probably because the level decay rates determined by such experiments are more readily available through other coherent transient techniques e.g. delayed nutation and adiabatic passage. Stimulated echoes have been observed in $^{13}CH_3F$ and $^{15}NH_3$ [14], but considerably more experiments have been conducted employing the Carr-Purcell echo train. This type of echo derives its name from a similar phenomenon in nuclear magnetic reso-

nance, discovered by Carr and Purcell in 1954 [36] — see Figure 2.3. When a two pulse photon echo sequence is followed by a third pulse, of area π, at a time after the second pulse identical to the interval between the first pulse and the echo, another echo is formed (this is perhaps more readily apparent using the Bloch vector model). Furthermore, when a sequence of π pulses is subsequently applied, all identically separated by the interval between the second and third pulses, then an echo is produced midway between each pulse pair. The collisional decay rate of the echoes formed differs from that of echoes formed from two excitation pulses, as it is insensitive to velocity changing collisions. The reason for this is that the dephasing that occurs after one of the π pulses is reversed after the next one and so on. By keeping the time between consecutive pairs of excitation pulses small, the dephasing brought about by velocity changing collisions can be made small, even if the time between the first excitation pulse and the n^{th} echo is of the order of several excited state lifetimes, and the n^{th} echo will be much greater in intensity than an ordinary two pulse echo formed at the same time after the initial excitation pulse. Carr-Purcell echoes have been used to determine the population decay rates, by inelastic collisions or spontaneous decay, in NH_2D [37] and $^{13}CH_3F$ [38].

2.3 Photon echoes formed in atomic gases

The first photon echoes produced in an atomic gas were two pulse echoes observed on the first resonance transition $6S_{\frac{1}{2}} \leftrightarrow 6P_{\frac{3}{2}}$ in caesium, by Bölger and Diels [39] in 1968. Working at a vapour pressure of 5×10^{-4} torr, they measured the decay of echo intensity as a function of interpulse time τ, without foreign gas perturbers, and obtained a lifetime for the excited state of 28 ns. Research work has mainly concentrated on optical transitions in lithium, sodium, caesium and ytterbium vapours which are perturbed by low pressures of noble gases ($\leq$ 1 torr), where high vapour pressures of active atoms (of the order of 10^{-5} torr) can be readily achieved at modest temperatures. Interest has focussed on measurements of echo decay rates for

inelastic collisions and elastic phase-interrupting collisions, the same mechanisms that produce foreign gas pressure broadening (see Subsection 1.2.1). Echoes provide a Doppler free technique for studying pressure broadening with the advantage that the perturber gas pressures used are very low (≤ 1 torr). Good reviews of some of this work are given by Mossberg et al [40] [41].

2.3.1 Two pulse photon echoes

Following the earlier work done by Bölger and Diels on the first resonance transition in caesium, Baer and Abella [42] in 1976 observed echoes on four separate transitions between the $F = 3, 4$ hyperfine components of the caesium $6S_{\frac{1}{2}}$ ground state, and the second excited fine structure doublet $7P_{\frac{1}{2}}$, $7P_{\frac{3}{2}}$ (the same transitions are studied in the experimental work of this thesis). For a caesium pressure of about 10^{-4} torr and without foreign gas perturber atoms, the lifetime for the $7P_{\frac{1}{2}}$ state was found to be approximately 150 ns, for both the $F = 3$ and $F = 4$ components of the ground state. Modulations were observed in the echo intensity as the interpulse time was increased, and these were interpreted as photon echo quantum beats due to hyperfine structure. The experimental results obtained were in close agreement to those predicted in theory [43], in which the caesium atom was treated as a multilevel system. A spherical tensor treatment of photon echo quantum beats has been produced by Baer [44]. Baer and Abella [45], and Aoki [46] have studied photon echo quantum beats. In some of these experiments they applied a weak longitudinal magnetic field which resulted in a rotation of the plane of polarisation of the echo produced on either of the $6S_{\frac{1}{2}} \leftrightarrow 7P_{\frac{1}{2}}, 7P_{\frac{3}{2}}$ transitions. This feature forms the basis of the polarisation rotation discrimination technique, in which identically plane-polarised excitation pulses, and the resultant echo, fall on an analyser whose polarisation axis is orthogonal to that of the excitation pulses. The excitation pulses are therefore blocked while a substantial part of the echo can be made to pass through the analyser, since the plane of polarisation of the echo is rotated by the magnetic field.

Sodium has also been used as an echo forming medium, with the first echoes observed on the sodium D lines by Bölger et al [47]. Collisional decay of the D line transitions due to phase interrupting effects was reported by Brewer and Genack [48] in 1976. In later experiments Flusberg et al [49] studied collisional relaxation by noble gases for sodium atoms in thermally unpopulated states. Two lasers were employed in the experiments, with the first laser being a 'pump' laser, tuned to resonance with the sodium D_1 line to populate the $3^2P_{\frac{1}{2}}$ state. The second laser was tuned to an appropriate $3^2P_{\frac{1}{2}} \leftrightarrow n^2S_{\frac{1}{2}}$ or $3^2P_{\frac{1}{2}} \leftrightarrow n^2D_{\frac{3}{2}}$ transition, and provided the two excitation pulses. The pump pulse preceded the first excitation pulse by 4 ns. All three pulses were collinear. Pockels cell shutters were used to reduce the intensity of these pulses at the photomultiplier tube, and the echo decay was measured by varying the noble gas pressure with fixed interpulse times. The exponential decay rate of the echo intensities for the various transitions did not exhibit a τ^3 dependence. This was assumed to be due to either population changing or elastic phase interrupting collisions (or both) dominating over velocity changing effects. Later work by Mossberg et al [50] [51] in 1980 studied the contribution of velocity changing effects to the relaxation of optical coherence in sodium-helium collisions, as well as noble gas relaxation of the sodium D lines.

Beach et al [52] conducted some two pulse echo experiments using lithium vapour without perturbers. In two separate experiments in which the excitation pulses were angled by 0.7 mrad and 1.4 mrad respectively, the measured range of echo intensities (for echoes formed on the lithium D_2 line) was greater than 10^{10}, and represented measurements made over a range of 15 radiative lifetimes. Echo intensity modulations due to the hyperfine structure of the upper state were also observed.

In other experiments using lithium, Kachru et al [53] [54] studied collisional effects on the two D line transitions, D_1 ($2S_{\frac{1}{2}} \leftrightarrow 2P_{\frac{1}{2}}$) and D_2 ($2S_{\frac{1}{2}} \leftrightarrow 2P_{\frac{3}{2}}$). They reported the first measurement of a total effective cross section $\sigma_{\text{eff}}(\infty)$, where $\sigma_{\text{eff}}(\tau) = \sigma_B + \sigma_v(\tau)$. Here σ_B describes the effects of hard, phase changing and inelastic collisions, and $\sigma_v(\tau)$ describes the ef-

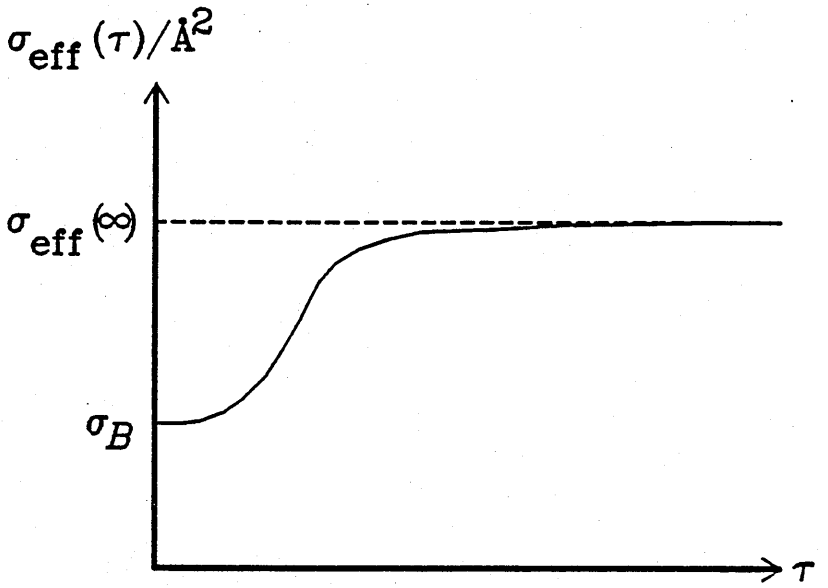

Figure 2.4 Variation of $\sigma_{\text{eff}}(\tau)$ with τ.

fects of soft velocity changing collisions (see Subsection 1.3.4). The results obtained for the variation of $\sigma_{\text{eff}}(\tau)$ with τ were similar to Figure 2.4. The graph has its distinctive shape for the following reasons. As mentioned in Subsection 1.3.4, velocity changes experienced by the atom initiate a phase change, which is built up linearly in time. For large velocity changes, only a comparatively short time has to elapse before the accumulated phase change results in the atom being 'lost' from the echo. For smaller velocity changes, the time required to accumulate a corresponding phase change is larger, with the result that as τ increases, weaker and weaker velocity changing collisions result in the atom being lost from the echo. At very large τ the velocity changing effect saturates towards a limiting value, $\sigma_{\text{eff}}(\infty)$, at which essentially all velocity changing collisions attenuate the echo. Typical velocity changes were estimated to be roughly 1% of the mean thermal speed.

The first resonance transition of ytterbium ($^1S_0 \leftrightarrow ^3P_1$) has also been studied by many workers. Forber et al [55] [56] investigated collisional effects with xenon as the perturber gas, using both photon echoes and Lamb dip measurements, and found that the values for σ_B and $\sigma_{\text{eff}}(\infty)$ obtained

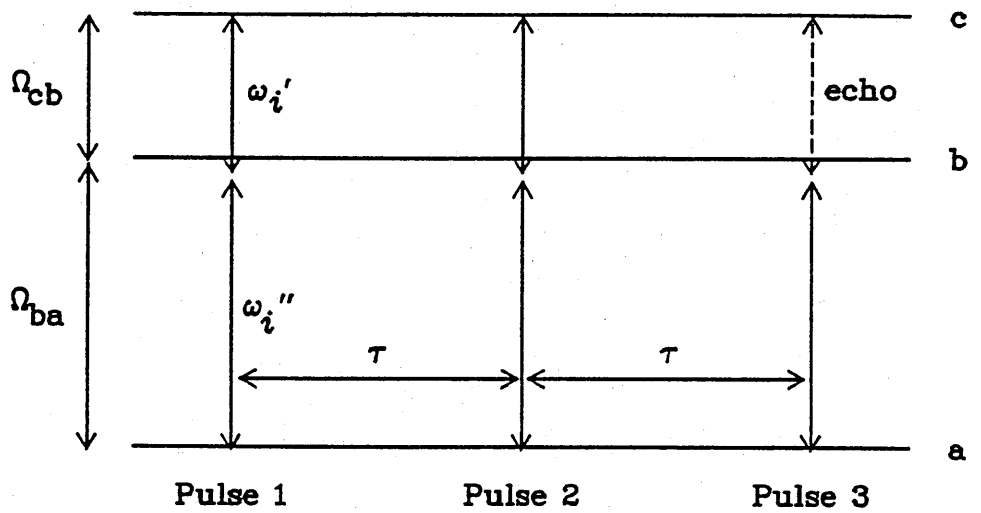

Figure 2.5 Excitation pulse sequence for a 'two-photon' echo.

by both techniques agreed to within 10%. Further work by the same authors on the same transition [57] measured the velocity dependence of the total cross section, again with a xenon perturber, and concluded that quantum mechanical van der Waals scattering was the predominant interaction.

Durrant and Manners [58] [59] made the first measurements of elastic collision cross sections for noble gas broadening of the caesium $6S_{\frac{1}{2}} \leftrightarrow 7P_{\frac{1}{2}}, 7P_{\frac{3}{2}}$ doublet in 1984. A vapour pressure of about 10^{-5} torr was used, and the echoes were observed using the polarisation rotation discrimination technique. Using helium, neon, argon and krypton as perturbers (with pressures typically below 1 torr), they found reasonable agreement between most of their measurements of the elastic collision cross sections and the corresponding broadening constants obtained by high resolution measurements of pressure broadened line profiles [5] [6] [7] [60]. Further noble gas perturber experiments for the same caesium transitions [61] established an estimate for the average diffractive velocity change produced by a collision.

In addition to the two pulse echoes described above, experiments have also been performed using the 'two-photon' echo. This type of echo (along

with other echoes) was predicted in several papers [62] [63] [64], but was first observed in sodium in 1978 by Flusberg et al [65]. The excitation pulse sequence employed is shown in Figure 2.5. The two-photon echo was produced in a three-level system with energy levels a, b and c such that the $a \leftrightarrow b$ and the $b \leftrightarrow c$ transitions were electric dipole allowed, but the $a \leftrightarrow c$ transition was not. The atom was excited by two 'pulses', each containing two optical fields ω_i' and ω_i'' (near Ω_{cb} and Ω_{ba} respectively) which could together resonantly excite the $a \leftrightarrow c$ transition by two photon absorption, producing a coherent superposition of the a and c states. A probe pulse of frequency ω_i'' applied at time τ after the second pulse simultaneously produced a photon echo of frequency ω_i'. Since the two-photon echo depends on the rephasing of the forbidden $a \leftrightarrow c$ transition, the echo intensity was independent of the collisional decay of the intermediate state, and so the collisional decay rate measured is that of the forbidden transition.

Generally speaking, collision cross sections measured by two pulse echo techniques agree fairly well with those measured by line broadening experiments. Mossberg et al [37] reported significant discrepancies between their photon echo measurements of the sodium $D_1 : D_2$ broadening constant ratios, and previously obtained linewidth measurements. Kachru et al [53] [54] in their experiments using lithium reported discrepancies between the ratios of the D line broadening cross sections for their echo measurements compared to those obtained by lineshape measurements. In their work on caesium, Durrant and Manners [58] [59] found that their broadening constant ratios were consistently slightly smaller than earlier line shape measurements [5] [6] [7] [60]. One possible reason for the discrepancies is that photon echo experiments are performed at very low pressures, whereas line broadening experiments are performed in the wings of the broadened profile at high pressures, where the impact approximation may no longer be strictly valid.

2.3.2 Three pulse photon echoes

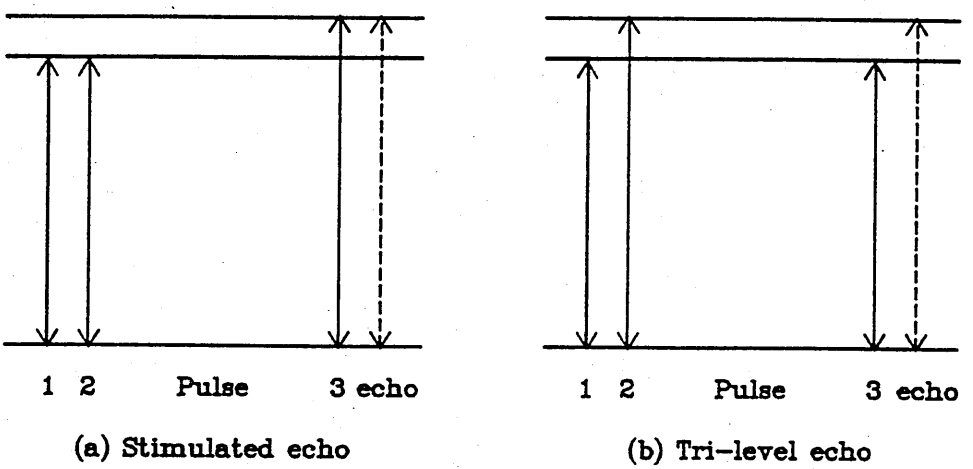

Figure 2.6 Excitation pulse sequences for (a) a stimulated echo, and (b) a tri-level echo.

A wide variety of three pulse photon echo experiments utilising one or more transitions is possible, and a common (but not rigorous) way of categorising them is to divide the experiments into two types. Those in which the first and second pulses are on the same transition are often called 'stimulated' echoes (these can occur in both two and three-level systems) — see Figure 2.6(a). Those in which the first and second pulses are not on the same transition are often termed 'tri-level' echoes — see Figure 2.6(b). When polarised light is used and different Zeeman transitions are excited this nomenclature is ambiguous. Sometimes the term tri-level is used when three energy levels are involved. The experiments performed for this thesis use polarised light, and for convenience a decision on terminology has had to be made. The term 'stimulated echo' is used when all three excitation pulses connect the same two energy levels (see Figure 1.23(c)), and the term 'tri-level' echo is used when three energy levels are involved (see Figure 1.23(a), (b)): these figures should be regarded as the defining figures whenever the terms stimulated and tri-level are subsequently used in this thesis.

In fact, several different kinds of tri-level and stimulated echo can be produced, and a comprehensive review is given by Mossberg et al [37]. Three pulse echoes have several advantages over two pulse echoes, one of these being that phase matching of the wave vectors for the excitation pulses and the echo can be achieved for non-collinear pulses (see Section 3.7). Another advantage is that three pulse echoes can be used to study the collisional relaxation of dipole forbidden transitions. More importantly perhaps, is that the effects of collisions on populations and Zeeman coherences can be studied — the subject of this thesis.

Phase matching for three pulse echoes allows for echo propagation in both the forward direction (this is taken to be in roughly the same direction as the first pulse), and also the backward direction (details of phase matching and Doppler dephasing effects are given in Chapter 3). Fujita et al [66] reported the first backward stimulated echo on the $3S_{\frac{1}{2}} \leftrightarrow 3P_{\frac{1}{2}}$ sodium D line in 1979, though since the excitation pulses had orthogonal polarisations, the authors pointed out that the echo could be thought of as a backward, two level version of a tri-level echo. Using argon as the perturber good agreement was found with the decay rate measurements obtained by Flusberg et al [49] using two pulse echoes. The same backward stimulated echo technique was employed by Asaka et al [67] in their measurements of collisional broadening of the $X\Sigma \leftrightarrow A\Sigma$ transition of molecular sodium. This technique is also employed in the experiments conducted in this thesis.

Mossberg et al [68] reported the first tri-level echo in sodium in 1977, when they investigated the collisional relaxation by argon of optical coherences on several forbidden $3^2S_{\frac{1}{2}} \leftrightarrow n^2D_{\frac{3}{2}}$ transitions. The excitation pulse sequence used is shown in Figure 2.7(a). Two years later the same authors [69] published their measurements of helium, neon and argon induced collisional relaxation of the forbidden $3S \leftrightarrow nS$ ($3S \leftrightarrow nD$) transitions, where n ranged from 5 to 20 (4 to 34). Where applicable, their collision cross sections compared very well with two photon absorption measurements. In another kind of tri-level experiment (termed an inverted difference frequency tri-level echo) [70] the cross sections were studied for noble gas broadening

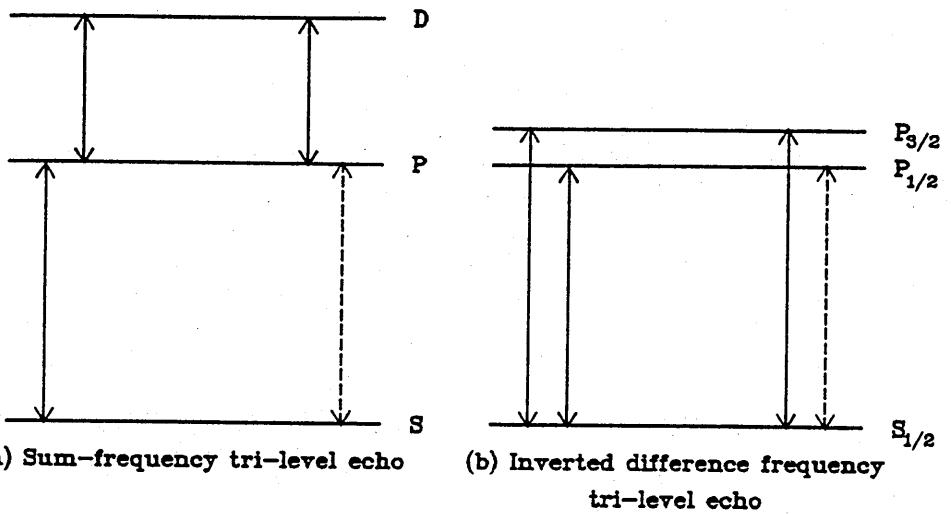

Figure 2.7 Excitation pulse sequences for (a) sum-frequency tri-level echo, and (b) inverted difference-frequency tri-level echo.

of the forbidden $3P_{\frac{1}{2}} \leftrightarrow 3P_{\frac{3}{2}}$ transition in sodium — the excitation pulse sequence for this experiment is shown in Figure 2.7(b). Similar tri-level echo experiments using caesium have been performed by Manners and Durrant [71], in which a tri-level echo was used to measure the collision cross sections (using noble gas perturbers) for the electric-dipole-forbidden fine structure transition $7P_{\frac{1}{2}} \leftrightarrow 7P_{\frac{3}{2}}$.

Stimulated echoes occur when the first two pulses of a three pulse sequence excite the same transition. The third pulse can then be on the same transition or on a different transition from one of the two levels excited. The important feature of the stimulated echo is that it is insensitive to phase changing collisions occurring in the interval t_{32} between the second and third pulses. This feature allows other collision mechanisms, such as velocity changing collisions, occurring in this interval to be studied.

Mossberg et al have performed stimulated echo measurements of he-

lium induced [72] and CO induced [73] velocity changing cross sections of sodium atoms in the $3S_{\frac{1}{2}}$ and $3P$ states. Several stimulated echo experiments have also been performed in ytterbium by Keller and Le Gouët [74] [75] [76], Yodh et al [77] and Ghosh et al [78] [79]. In these experiments different Zeeman sublevels are selected by suitably polarising the excitation pulses. Keller and Le Gouët measured elastic and depolarising cross sections between helium, neon and xenon perturbers and $6s6p^3P_1$ level ytterbium atoms. Yodh et al performed similar experiments, though the respective polarisations of the excitation pulses enabled different relaxation rates to be studied. Ghosh et al investigated collision kernels via isolated multipole echoes: the first two excitation pulses were identically elliptically polarised, creating a velocity space grating formed from anisotropic moments of the $^3P_1$ excited state. The third excitation pulse was plane polarised and incident on the sample at an angle to the first two pulses. The resultant echo was formed in the same direction as the third pulse, and was fed into a photomultiplier tube after passing through an analyser. Through varying the polarisation of the first two pulses, the collisional relaxation of different multipole moments could be studied.

Lastly, mention is made of some interesting phase conjugation experiments conducted by Carlson et al [80] in ytterbium vapour. Using a stimulated echo, they found that the echo signals could be backward propagating, phase conjugate replicas of the second excitation pulse. A considerable amount of work has also been conducted into the use of stimulated photon echoes as a means of storing information [81] [82].

Chapter 3

A density matrix approach to photon echo formation in a three-level atom

This chapter deals with the theory of echo formation in a non-degenerate three-level atom using density matrices. The final section shows how the theory can be modified to apply to real atoms with Zeeman-degenerate levels. Starting with the time-dependent Schrödinger equation, Section 3.1 considers an atom interacting with an applied optical field of frequency ω and introduces the idea of a time-independent Hamiltonian, and a corresponding time evolution operator in a 'rotating frame'. Section 3.2 considers the case of near-resonant pulsed excitation and derives the rotating frame Hamiltonian $\hat{H}_\omega$ for a two-level atom in matrix form. A form of the time evolution operator matrix for a two-level atom, which can be applied to a three-level atom subject to pulses that are resonant with two levels only, is derived in Section 3.3. The concept of density matrices is introduced in Section 3.4. Section 3.5 derives the dipole moment expectation value for a single atom. The phase of a dipole moment due to a single atom, and hence the macroscopic polarisation of a vapour sample as a whole, is calculated in Section 3.6. Section 3.7 considers the case when this polarisation is a maximum, which constitutes the echo formation time, and determines the reduction of echo intensity when non-collinear excitation pulses are used. Using the concept of 'Fresnel Zones', Section 3.8 establishes expressions for both the absolute echo intensity, and the number of photons which comprise

the echo, for collinear excitation pulses. Section 3.9 shows how velocity modulated populations can be produced by two excitation pulses. Finally, the rotating-frame phase matrix for a simplified version of the stimulated echo experiments performed in this thesis is given in Section 3.10. Throughout this chapter the assumption is made that the atom can be considered stationary for the duration of each excitation pulse (i.e. Doppler broadening during excitation is ignored): this is analogous to the assumption made in Chapter 1 that during excitation $\kappa E_0 \gg \Delta\omega$.

3.1 The time evolution operator of an excited three-level atom

The laboratory frame time dependent Schrödinger equation for an isolated, unperturbed atom is given by

$$\hat{H}_0\psi(t) = i\hbar\frac{\partial\psi(t)}{\partial t} \tag{3.1}$$

where $\hat{H}_0$ is the Hamiltonian (operators are denoted by $\hat{}$). If the atom is irradiated with light of frequency ω then an atom-field interaction energy operator $\hat{V}$ results, where in the electric dipole approximation $\hat{V}$ is given by

$$\hat{V} = -\hat{\vec{p}}\cdot\vec{E} \tag{3.2}$$

here $\hat{\vec{p}}$ is the electric dipole vector operator and $\vec{E}$ is the electric vector of the steady optical field. Equation 3.1 then becomes

$$\begin{aligned}\frac{\partial\psi(t)}{\partial t} &= -\frac{i}{\hbar}[\hat{H}_0 + \hat{V}]\psi(t) \\ &= -\frac{i}{\hbar}\hat{H}\psi(t)\end{aligned} \tag{3.3}$$

This equation can be more easily solved if one removes the fast optical time variations of angular frequency ω by transforming from the laboratory frame to a 'rotating frame' and uses an approximation known as 'the rotating wave approximation' to obtain a time-independent Hamiltonian $\hat{H}_\omega$. The details of the transformation will be dealt with in the next section, but for the

moment the assumption is made that the transformed Hamiltonian $\hat{H}_\omega$ is time-independent. Wave functions and operators in the rotating frame are denoted by a subscript ω. If one defines a wave function $\psi_\omega(t)$ of slowly varying amplitude by

$$\psi_\omega(t) = e^{i\hat{A}t}\psi(t) \tag{3.4}$$

where $\hat{A}$ is a transformation operator which removes the fast optical time variations of frequency ω, then

$$\psi(t) = e^{-i\hat{A}t}\psi_\omega(t)$$

Differentiating equation 3.4 gives

$$\frac{\partial\psi_\omega(t)}{\partial t} = i\hat{A}e^{i\hat{A}t}\psi(t) + e^{i\hat{A}t}\frac{\partial\psi(t)}{\partial t}$$

and applying equation 3.3 yields

$$\begin{aligned}
\frac{\partial\psi_\omega(t)}{\partial t} &= e^{i\hat{A}t}i\hat{A}\psi(t) + e^{i\hat{A}t}[-\frac{i}{\hbar}(\hat{H}_0 + \hat{V})]\psi(t) \\
&= e^{i\hat{A}t}i\hat{A}e^{-i\hat{A}t}\psi_\omega(t) - e^{i\hat{A}t}[\frac{i}{\hbar}(\hat{H}_0 + \hat{V})]e^{-i\hat{A}t}\psi_\omega(t) \\
&= -\frac{i}{\hbar}e^{i\hat{A}t}[\hat{H}_0 + \hat{V} - \hbar\hat{A}]e^{-i\hat{A}t}\psi_\omega(t) \\
\frac{\partial\psi_\omega(t)}{\partial t} &= -\frac{i}{\hbar}\hat{H}_\omega\psi_\omega(t)
\end{aligned} \tag{3.5}$$

where

$$\hat{H}_\omega = e^{i\hat{A}t}[\hat{H}_0 + \hat{V} - \hbar\hat{A}]e^{-i\hat{A}t} \tag{3.6}$$

Since the condition was made that $\hat{H}_\omega$ is time independent, equation 3.5 can be integrated to give

$$\begin{aligned}
\psi_\omega(t) &= e^{-\frac{i}{\hbar}\hat{H}_\omega t}\psi_\omega(t_0) \\
&= \hat{M}\psi_\omega(t_0)
\end{aligned} \tag{3.7}$$

where $\psi_\omega(t_0)$ is the initial wave function and $\hat{M}$ is the time evolution operator in the rotating frame. This analysis has so far considered steady continuous wave excitation starting at time t_0. From now on this chapter

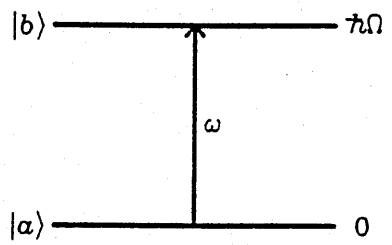

Figure 3.1 Ground-state two-level atom excited by light of frequency ω

will consider the effect of Fourier-transform limited square pulses of duration τ. The time evolution operator is then given by

$$\hat{M} = e^{-\frac{i}{\hbar}\hat{H}_\omega \tau} \tag{3.8}$$

In the next section the explicit form of $\hat{H}_\omega$ is obtained for a two-level sub-system excited by a resonant pulse.

3.2 A time-independent Hamiltonian for a two-level system

In all of the experiments performed for this thesis, any one laser pulse is tuned to resonance with a transition connecting only two levels, so it is sufficient to limit this analysis to the resonant interaction of a laser pulse with a two-level sub-system. Consider the case of a non-degenerate two-level atom with ground state $|a>$ of zero energy and excited state $|b>$ of energy $\hbar\Omega$ as depicted in Figure 3.1. The Hamiltonian for the system is given by the matrix $\mathbf{H_0}$ where

$$\mathbf{H_0} = \begin{pmatrix} 0 & 0 \\ 0 & \hbar\Omega \end{pmatrix} \tag{3.9}$$

Since this analysis concerns states which are non-degenerate, the vector aspects of $\hat{\vec{p}}$ and $\vec{E}$ in equation 3.2 are suppressed so it is sufficient to look at scalar representations of these quantities. The matrix for the dipole operator

is then

$$\mathrm{p} = \begin{pmatrix} 0 & p_{ab} \\ p_{ba} & 0 \end{pmatrix} \tag{3.10}$$

where $p_{ab} =< a|\hat{p}|b >$. The electric field seen by the atom can be represented by

$$E = \mathcal{E}e^{-i(\omega t - \vec{k}\cdot\vec{r})} + c.c. \tag{3.11}$$

where $\mathcal{E}$ is a constant amplitude and $\vec{k}$ is the wavevector for a pulse of frequency ω near Ω. It is assumed that the pulse duration is sufficiently small that the effect of the motion of the atom during the pulse can be neglected and so $\vec{r}$ is the position of the atom at the time of the pulse. Since E is not an operator, the operator matrix $\mathrm{V} = -\mathrm{p}E$ is given by

$$\mathrm{V} = \begin{pmatrix} 0 & -p_{ab}(\mathcal{E}^* e^{i(\omega t - \vec{k}\cdot\vec{r})} + cc) \\ -p_{ba}(\mathcal{E}e^{-i(\omega t - \vec{k}\cdot\vec{r})} + cc) & 0 \end{pmatrix} \tag{3.12}$$

From equation 3.4 the matrix for $e^{i\mathrm{A}t}$ is given by

$$e^{i\mathrm{A}t} = \begin{pmatrix} 1 & 0 \\ 0 & e^{i\omega t} \end{pmatrix} = \begin{pmatrix} e^{i0t} & 0 \\ 0 & e^{i\omega t} \end{pmatrix}$$

Hence A is

$$\mathrm{A} = \begin{pmatrix} 0 & 0 \\ 0 & \omega \end{pmatrix} \tag{3.13}$$

The Hamiltonian can now be determined in matrix form using equation 3.6 i.e.

$$\mathrm{H}_\omega = e^{i\mathrm{A}t}(\mathrm{H}_0 + \mathrm{V} - \hbar\mathrm{A})e^{-i\mathrm{A}t} \tag{3.14}$$

This calculation is greatly simplified since H_0 and $-\hbar\mathrm{A}$ are diagonal and therefore remain unchanged by this transformation. Hence equation 3.14 becomes

$$\mathrm{H}_\omega = \mathrm{H}_0 - \hbar\mathrm{A} + e^{i\mathrm{A}t}\mathrm{V}e^{-i\mathrm{A}t} \tag{3.15}$$

where

$$\mathrm{H}_0 - \hbar\mathrm{A} = \begin{pmatrix} 0 & 0 \\ 0 & \hbar(\Omega - \omega) \end{pmatrix} \tag{3.16}$$

Now $e^{iAt}Ve^{-iAt}$ in matrix form is

$$e^{iAt}Ve^{-iAt} = \begin{pmatrix} 1 & 0 \\ 0 & e^{i\omega t} \end{pmatrix} \times$$

$$\begin{pmatrix} 0 & -p_{ab}(\mathcal{E}^* e^{i(\omega t - \vec{k}\cdot\vec{r})} + cc) \\ -p_{ba}(\mathcal{E} e^{-i(\omega t - \vec{k}\cdot\vec{r})} + cc) & 0 \end{pmatrix} \begin{pmatrix} 1 & 0 \\ 0 & e^{-i\omega t} \end{pmatrix}$$

On evaluation this becomes

$$e^{iAt}Ve^{-iAt} =$$

$$\begin{pmatrix} 0 & -p_{ab}(\mathcal{E}^* e^{-i\vec{k}\cdot\vec{r}} + \mathcal{E} e^{-i(2\omega t - \vec{k}\cdot\vec{r})}) \\ -p_{ba}(\mathcal{E} e^{i\vec{k}\cdot\vec{r}} + \mathcal{E}^* e^{i(2\omega t - \vec{k}\cdot\vec{r})}) & 0 \end{pmatrix}$$

Using the rotating wave approximation allows one to neglect terms containing $e^{\pm 2i\omega t}$ giving

$$e^{iAt}Ve^{-iAt} = \begin{pmatrix} 0 & -p_{ab}\mathcal{E}^* e^{-i\vec{k}\cdot\vec{r}} \\ -p_{ba}\mathcal{E} e^{i\vec{k}\cdot\vec{r}} & 0 \end{pmatrix} \tag{3.17}$$

Hence

$$\mathrm{H}_\omega = \begin{pmatrix} 0 & -p_{ab}\mathcal{E}^* e^{-i\vec{k}\cdot\vec{r}} \\ -p_{ba}\mathcal{E} e^{i\vec{k}\cdot\vec{r}} & \hbar(\Omega - \omega) \end{pmatrix} \tag{3.18}$$

Clearly H_ω is time-independent.

Since the atom can be considered to be at rest for the duration of the excitation pulse there is effectively no Doppler shift, so all the atoms see the same optical field. If $\omega = \Omega$ there is no detuning and $\hbar(\Omega - \omega) = 0$ holds for all atoms. The matrix for H_ω can be written

$$\mathrm{H}_\omega = \begin{pmatrix} 0 & \alpha^* \\ \alpha & 0 \end{pmatrix} \tag{3.19}$$

where

$$\alpha = -p_{ba}\mathcal{E} e^{i\vec{k}\cdot\vec{r}} \tag{3.20}$$

In summary the rotating wave approximation has been used to obtain a time-independent Hamiltonian in the rotating frame. The next step is to solve the Schrödinger equation.

3.3 Determination of M matrix

Equation 3.8 defines the matrix M i.e.

$$\mathrm{M} = e^{-\frac{i}{\hbar}\mathrm{H}_\omega \tau} \tag{3.21}$$

H_ω is not diagonal and so the calculation cannot be easily performed. However it is possible to transform the exponent in equation 3.21 to one which is diagonal. Equation 3.21 can be expressed as a Taylor sum i.e.

$$\mathrm{M} = 1 + \frac{-i}{\hbar}\mathrm{H}_\omega \tau + \frac{1}{2!}(\frac{-i}{\hbar}\mathrm{H}_\omega \tau)^2 + ... \tag{3.22}$$

Let S be an arbitrary square matrix. Then

$$\begin{aligned}
\mathrm{M} &= \mathrm{S}\mathrm{S}^{-1}(1 + \frac{-i}{\hbar}\mathrm{H}_\omega \tau + \frac{1}{2!}(\frac{-i}{\hbar}\mathrm{H}_\omega \tau)^2 + ...)\mathrm{S}\mathrm{S}^{-1} \\
&= \mathrm{S}(1 + \frac{-i}{\hbar}\tau \mathrm{S}^{-1}\mathrm{H}_\omega \mathrm{S} + \frac{1}{2!}(\frac{-i}{\hbar}\tau)^2 \mathrm{S}^{-1}\mathrm{H}_\omega^2 \mathrm{S} + ...)\mathrm{S}^{-1} \\
&= \mathrm{S}(1 + \frac{-i}{\hbar}\tau \mathrm{S}^{-1}\mathrm{H}_\omega \mathrm{S} + \frac{1}{2!}(\frac{-i}{\hbar}\tau)^2 \mathrm{S}^{-1}\mathrm{H}_\omega \mathrm{S}\mathrm{S}^{-1}\mathrm{H}_\omega \mathrm{S} + ...)\mathrm{S}^{-1} \\
&= \mathrm{S}(1 + \frac{-i}{\hbar}\tau \mathrm{S}^{-1}\mathrm{H}_\omega \mathrm{S} + \frac{1}{2!}(\frac{-i}{\hbar}\tau)^2 (\mathrm{S}^{-1}\mathrm{H}_\omega \mathrm{S})^2 + ...)\mathrm{S}^{-1}
\end{aligned}$$

and thus

$$\mathrm{M} = \mathrm{S}e^{-\frac{i}{\hbar}\tau \mathrm{S}^{-1}\mathrm{H}_\omega \mathrm{S}}\mathrm{S}^{-1} \tag{3.23}$$

Clearly this transformation holds for any square matrix but is of use here if S is the matrix which diagonalises H_ω.

3.3.1 The diagonalisation of H_ω

The diagonalising matrix S can be determined by looking at the eigenvalues λ of H_ω i.e.

$$\begin{aligned}
|\mathrm{H}_\omega - \lambda \mathrm{I}| &= 0 \\
\begin{vmatrix} -\lambda & \alpha^* \\ \alpha & -\lambda \end{vmatrix} &= 0 \\
\lambda^2 &= |\alpha|^2 \\
\lambda &= \pm|\alpha|
\end{aligned}$$

The eigenvalues must also satisfy the matrix equation

$$(\mathrm{H}_\omega - \lambda \mathrm{I})\mathrm{X} = 0 \tag{3.24}$$

where X is the column vector

$$\mathrm{X} = \begin{pmatrix} x_1 \\ x_2 \end{pmatrix}$$

Thus for $\lambda = |\alpha|$ equation 3.24 becomes

$$\begin{aligned} \begin{pmatrix} -|\alpha| & \alpha^* \\ \alpha & -|\alpha| \end{pmatrix} \begin{pmatrix} x_1 \\ x_2 \end{pmatrix} &= 0 \\ -|\alpha|x_1 + \alpha^* x_2 &= 0 \\ x_2 &= \frac{\alpha}{|\alpha|} x_1 \end{aligned}$$

giving the column eigenvector

$$\begin{pmatrix} 1 \\ \frac{\alpha}{|\alpha|} \end{pmatrix}$$

which under normalisation becomes

$$\mathrm{X}_+ = \frac{1}{\sqrt{2}} \begin{pmatrix} 1 \\ \frac{\alpha}{|\alpha|} \end{pmatrix} \tag{3.25}$$

where X_+ denotes the column eigenvector obtained when $\lambda = |\alpha|$. For $\lambda = -|\alpha|$ another normalised column eigenvector X_- results such that

$$\mathrm{X}_- = \frac{1}{\sqrt{2}} \begin{pmatrix} 1 \\ -\frac{\alpha}{|\alpha|} \end{pmatrix} \tag{3.26}$$

The diagonalising matrix S is then the square matrix formed from the two column vectors i.e.

$$\mathrm{S} = \frac{1}{\sqrt{2}} \begin{pmatrix} 1 & 1 \\ \frac{\alpha}{|\alpha|} & -\frac{\alpha}{|\alpha|} \end{pmatrix} \tag{3.27}$$

A closer look at S reveals that it is an orthogonal matrix, since the scalar product of X_+ and X_- is zero (the two row vectors that comprise S also have a scalar product of zero) and therefore

$$\mathrm{S}^{-1} = \mathrm{S}^\dagger$$

Thus

$$\mathrm{S}^{-1} = \frac{1}{\sqrt{2}} \begin{pmatrix} 1 & \frac{\alpha^*}{|\alpha|} \\ 1 & -\frac{\alpha^*}{|\alpha|} \end{pmatrix} \tag{3.28}$$

3.3.2 The matrix M

The factor $\mathrm{S}^{-1}\mathrm{H}_\omega\mathrm{S}$ in the exponent of equation 3.23 is

$$\begin{aligned} \mathrm{S}^{-1}\mathrm{H}_\omega\mathrm{S} &= \frac{1}{2} \begin{pmatrix} 1 & \frac{\alpha^*}{|\alpha|} \\ 1 & -\frac{\alpha^*}{|\alpha|} \end{pmatrix} \begin{pmatrix} 0 & \alpha^* \\ \alpha & 0 \end{pmatrix} \begin{pmatrix} 1 & 1 \\ \frac{\alpha}{|\alpha|} & -\frac{\alpha}{|\alpha|} \end{pmatrix} \\ &= \begin{pmatrix} |\alpha| & 0 \\ 0 & -|\alpha| \end{pmatrix} \end{aligned} \tag{3.29}$$

and because this is diagonal one obtains

$$e^{-\frac{i}{\hbar}\mathrm{S}^{-1}\mathrm{H}_\omega\mathrm{S}\tau} = \begin{pmatrix} e^{-i\frac{|\alpha|}{\hbar}\tau} & 0 \\ 0 & e^{i\frac{|\alpha|}{\hbar}\tau} \end{pmatrix} \tag{3.30}$$

Introducing θ, the pulse area, where

$$\theta = 2|\alpha|\tau/\hbar \tag{3.31}$$

allows equation 3.30 to be written as

$$e^{-\frac{i}{\hbar}\mathrm{S}^{-1}\mathrm{H}_\omega\mathrm{S}\tau} = \begin{pmatrix} e^{-i\frac{\theta}{2}} & 0 \\ 0 & e^{i\frac{\theta}{2}} \end{pmatrix} \tag{3.32}$$

The full expression for equation 3.23 then becomes

$$\mathrm{M} = \frac{1}{2} \begin{pmatrix} 1 & 1 \\ \frac{\alpha}{|\alpha|} & -\frac{\alpha}{|\alpha|} \end{pmatrix} \begin{pmatrix} e^{-i\frac{\theta}{2}} & 0 \\ 0 & e^{i\frac{\theta}{2}} \end{pmatrix} \begin{pmatrix} 1 & \frac{\alpha^*}{|\alpha|} \\ 1 & -\frac{\alpha^*}{|\alpha|} \end{pmatrix} \tag{3.33}$$

which on evaluation is found to be

$$\begin{aligned} \mathrm{M} &= \begin{pmatrix} \frac{1}{2}(e^{i\frac{\theta}{2}} + e^{-i\frac{\theta}{2}}) & \frac{\alpha^*}{2|\alpha|}(e^{-i\frac{\theta}{2}} - e^{i\frac{\theta}{2}}) \\ \frac{\alpha}{2|\alpha|}(e^{-i\frac{\theta}{2}} - e^{i\frac{\theta}{2}}) & \frac{1}{2}(e^{i\frac{\theta}{2}} + e^{-i\frac{\theta}{2}}) \end{pmatrix} \\ &= \begin{pmatrix} \cos\frac{\theta}{2} & -i\frac{\alpha^*}{|\alpha|}\sin\frac{\theta}{2} \\ -i\frac{\alpha}{|\alpha|}\sin\frac{\theta}{2} & \cos\frac{\theta}{2} \end{pmatrix} \end{aligned} \tag{3.34}$$

Equation 3.34 gives the M matrix for a two-level system subject to a single resonant pulse. The next step is to adapt this result so that it is appropriate for a three-level system subject to resonant pulses.

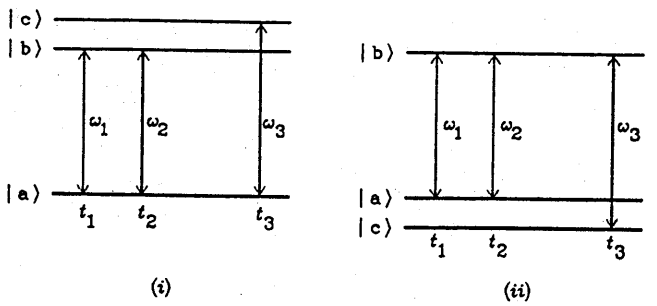

Figure 3.2 (*i*) Ground-state tri-level echo sequence for a three-level atom; (*ii*) Excited-state tri-level echo sequence for a three-level atom.

3.3.3 The M matrix for a three-level system

If one now considers the case of the three-level atom shown in Figure 3.2(*i*) with ground state $|a>$ and excited states $|b>$ and $|c>$ (with state $|c>$ at a higher energy than state $|b>$), the matrix $\mathrm{M}_{mb\leftrightarrow a}$ for a pulse of frequency ω_m (where $m = 1, 2$) which is resonant with the $|b> - |a>$ transition is clearly given by

$$\mathrm{M}_{1b\leftrightarrow a} = \begin{pmatrix} \cos\frac{\theta_1}{2} & -i\frac{\alpha^*}{|\alpha|}\sin\frac{\theta_1}{2} & 0 \\ -i\frac{\alpha}{|\alpha|}\sin\frac{\theta_1}{2} & \cos\frac{\theta_1}{2} & 0 \\ 0 & 0 & 1 \end{pmatrix} \tag{3.35}$$

where $\alpha = -p_{ba}\mathcal{E}_1 e^{i\vec{k_1}\cdot\vec{r_1}}$ and $\theta_1 = 2|\alpha|\tau/\hbar$. Similarly a pulse of frequency ω_m (where $m = 3$) which only acts on the $|c> - |a>$ transition has an $\mathrm{M}_{mc\leftrightarrow a}$ matrix given by

$$\mathrm{M}_{3c\leftrightarrow a} = \begin{pmatrix} \cos\frac{\theta_3}{2} & 0 & -i\frac{\gamma^*}{|\gamma|}\sin\frac{\theta_3}{2} \\ 0 & 1 & 0 \\ -i\frac{\gamma}{|\gamma|}\sin\frac{\theta_3}{2} & 0 & \cos\frac{\theta_3}{2} \end{pmatrix} \tag{3.36}$$

where $\gamma = -p_{ca}\mathcal{E}_3 e^{i\vec{k_3}\cdot\vec{r_3}}$ and $\theta_3 = 2|\gamma|\tau/\hbar$. The pulse sequence shown in Figure 3.2(*i*) will in future be referred to as the 'ground-state tri-level echo' sequence since the ground state is the one level common to all three excitation pulses and the echo (when formed). The density matrix analysis in the next section features explicit calculations for the ground-state tri-level

echo. The result for the excited-state tri-level echo, Figure 3.2(ii), will just be quoted since the analysis is similar to that for the ground-state tri-level echo, but the main steps in the calculation are given in Appendix A.

3.4 Generation of density matrices

If a three-level system is described in the laboratory frame by a state vector Ψ, then the laboratory frame density matrix $\rho(t)$ is defined by

$$\rho(t) = \Psi\Psi^{\dagger} \tag{3.37}$$

Transferring to the rotating frame gives a new state vector Ψ_ω where according to equation 3.4

$$\Psi_\omega = e^{i\mathrm{A}t}\Psi$$

Now

$$\Psi_\omega^{\dagger} = \Psi e^{-i\mathrm{A}t}$$

and so the density matrix in the rotating frame $\rho_\omega(t)$ is denoted by the expression

$$\begin{aligned} \rho_\omega(t) &= \Psi_\omega\Psi_\omega^{\dagger} \\ &= e^{i\mathrm{A}t}\Psi\Psi^{\dagger}e^{-i\mathrm{A}t} \\ &= e^{i\mathrm{A}t}\rho(t)e^{-i\mathrm{A}t} \end{aligned} \tag{3.38}$$

Let $\rho_\omega(t_0)$ be the initial rotating frame density matrix. For a resonant laser pulse occurring at time t where $t > t_0$ the time evolution of the density matrix is described by

$$\rho_\omega(t) = \mathrm{M}\rho_\omega(t_0)\mathrm{M}^{-1} \tag{3.39}$$

For an arbitrary sequence of n pulses the interaction-picture density matrix is clearly given by

$$\rho_\omega(t) = \mathrm{M}_n\mathrm{M}_{n-1}..\mathrm{M}_1\rho_\omega(t_0)\mathrm{M}_1^{-1}..\mathrm{M}_{n-1}^{-1}\mathrm{M}_n^{-1} \tag{3.40}$$

where $t > t_n$, $t_n > t_{n-1}$ and t_n is the time of occurrence of the nth pulse. Equation 3.39 also requires the inverse M matrix and it is a straight-forward

matter to show that for the three-level interaction matrices established earlier the inverse matrices are

$$\mathrm{M}^{-1}_{1b\leftrightarrow a} = \begin{pmatrix} \cos\frac{\theta_1}{2} & i\frac{\alpha^*}{|\alpha|}\sin\frac{\theta_1}{2} & 0 \\ i\frac{\alpha}{|\alpha|}\sin\frac{\theta_1}{2} & \cos\frac{\theta_1}{2} & 0 \\ 0 & 0 & 1 \end{pmatrix} \tag{3.41}$$

and

$$\mathrm{M}^{-1}_{3c\leftrightarrow a} = \begin{pmatrix} \cos\frac{\theta_3}{2} & 0 & i\frac{\gamma^*}{|\gamma|}\sin\frac{\theta_3}{2} \\ 0 & 1 & 0 \\ i\frac{\gamma}{|\gamma|}\sin\frac{\theta_3}{2} & 0 & \cos\frac{\theta_3}{2} \end{pmatrix} \tag{3.42}$$

The laboratory-frame density matrix for a three-level atom which is initially in the ground state is

$$\rho(t_0) = \begin{pmatrix} 1 & 0 & 0 \\ 0 & 0 & 0 \\ 0 & 0 & 0 \end{pmatrix} \tag{3.43}$$

Applying equation 3.38 gives

$$\rho_\omega(t_0) = \begin{pmatrix} 1 & 0 & 0 \\ 0 & 0 & 0 \\ 0 & 0 & 0 \end{pmatrix} \tag{3.44}$$

Using equation 3.39 for the first pulse in the ground-state tri-level echo sequence (see Figure 3.2(i)) i.e.

$$\rho_\omega(t_1) = \mathrm{M}_{1b\leftrightarrow a}\rho_\omega(t_0)\mathrm{M}^{-1}_{1b\leftrightarrow a} \tag{3.45}$$

yields

$$\rho_\omega(t_1) = \begin{pmatrix} \cos^2\frac{\theta_1}{2} & i\frac{\alpha^*}{2|\alpha|}\sin\theta_1 & 0 \\ -i\frac{\alpha}{2|\alpha|}\sin\theta_1 & \sin^2\frac{\theta_1}{2} & 0 \\ 0 & 0 & 0 \end{pmatrix} \tag{3.46}$$

If a second pulse of the same frequency as applied at a time t_2 then the density matrix at time t_2 is calculated from

$$\rho_\omega(t_2) = \mathrm{M}_{2b\leftrightarrow a}\rho_\omega(t_1)\mathrm{M}^{-1}_{2b\leftrightarrow a} \tag{3.47}$$

giving

$$\rho_\omega(t_2) = \begin{pmatrix} \rho_{aa} & \rho_{ab} & 0 \\ \rho_{ba} & \rho_{bb} & 0 \\ 0 & 0 & 0 \end{pmatrix} \tag{3.48}$$

where

$$\begin{aligned}
\rho_{aa} &= \cos^2\frac{\theta_1}{2}\cos^2\frac{\theta_2}{2} + \sin^2\frac{\theta_1}{2}\sin^2\frac{\theta_2}{2} - \frac{1}{4}\sin\theta_1\sin\theta_2\left(\frac{\alpha^*\beta + \beta^*\alpha}{|\alpha||\beta|}\right) \\
\rho_{bb} &= \sin^2\frac{\theta_1}{2}\cos^2\frac{\theta_2}{2} + \cos^2\frac{\theta_1}{2}\sin^2\frac{\theta_2}{2} + \frac{1}{4}\sin\theta_1\sin\theta_2\left(\frac{\alpha^*\beta + \beta^*\alpha}{|\alpha||\beta|}\right) \\
\rho_{ab} &= \rho^*_{ba} = \frac{i}{2}\sin\theta_1\left(\cos^2\frac{\theta_2}{2}\frac{\alpha^*}{|\alpha|} - \sin^2\frac{\theta_2}{2}\frac{\alpha\beta^{*^2}}{|\alpha||\beta|^2}\right) + \frac{i}{2}\cos\theta_1\sin\theta_2\frac{\beta^*}{|\beta|}
\end{aligned}$$

$\beta = -p_{ba}\mathcal{E}_2 e^{i\vec{k}_2\cdot\vec{r}_2}$ and $\theta_2 = 2|\beta|\tau/\hbar$.

If a third pulse of frequency ω_3 acts upon the system at time t_3 then the resulting density matrix at time t_3 is given by

$$\rho_\omega(t_3) = \mathrm{M}_{3c\leftrightarrow a}\rho_\omega(t_2)\mathrm{M}^{-1}_{3c\leftrightarrow a}$$

Hence

$$\rho_\omega(t_3) = \begin{pmatrix} \rho_{aa} & \rho_{ab} & \rho_{ac} \\ \rho_{ba} & \rho_{bb} & \rho_{bc} \\ \rho_{ca} & \rho_{cb} & \rho_{cc} \end{pmatrix} \tag{3.49}$$

where

$$\begin{aligned}
\rho_{aa} &= \cos^2\frac{\theta_3}{2}\left[\cos^2\frac{\theta_1}{2}\cos^2\frac{\theta_2}{2} + \sin^2\frac{\theta_1}{2}\sin^2\frac{\theta_2}{2} - \frac{1}{4}\sin\theta_1\sin\theta_2\left(\frac{\alpha^*\beta + \beta^*\alpha}{|\alpha||\beta|}\right)\right] \\
\rho_{bb} &= \sin^2\frac{\theta_1}{2}\cos^2\frac{\theta_2}{2} + \cos^2\frac{\theta_1}{2}\sin^2\frac{\theta_2}{2} + \frac{1}{4}\sin\theta_1\sin\theta_2\left(\frac{\alpha^*\beta + \beta^*\alpha}{|\alpha||\beta|}\right) \\
\rho_{cc} &= \sin^2\frac{\theta_3}{2}\left[\cos^2\frac{\theta_1}{2}\cos^2\frac{\theta_2}{2} + \sin^2\frac{\theta_1}{2}\sin^2\frac{\theta_2}{2} - \frac{1}{4}\sin\theta_1\sin\theta_2\left(\frac{\alpha^*\beta + \beta^*\alpha}{|\alpha||\beta|}\right)\right] \\
\rho_{ab} &= \rho^*_{ba} = \frac{i}{2}\cos\frac{\theta_3}{2}\left[\sin\theta_1\left(\cos^2\frac{\theta_2}{2}\frac{\alpha^*}{|\alpha|} - \sin^2\frac{\theta_2}{2}\frac{\alpha\beta^{*^2}}{|\alpha||\beta|^2}\right) + \cos\theta_1\sin\theta_2\frac{\beta^*}{|\beta|}\right] \\
\rho_{ac} &= \rho^*_{ca} = \frac{i}{2}\sin\theta_3\frac{\gamma^*}{|\gamma|}\left[\cos^2\frac{\theta_1}{2}\cos^2\frac{\theta_2}{2} + \sin^2\frac{\theta_1}{2}\sin^2\frac{\theta_2}{2} - \frac{1}{4}\sin\theta_1\sin\theta_2\left(\frac{\alpha^*\beta + \beta^*\alpha}{|\alpha||\beta|}\right)\right] \\
\rho_{bc} &= \rho^*_{cb} = \frac{1}{2}\sin\frac{\theta_3}{2}\frac{\gamma^*}{|\gamma|}\left[\sin\theta_1\left(\sin^2\frac{\theta_2}{2}\frac{\alpha^*\beta^2}{|\alpha||\beta|^2} - \cos^2\frac{\theta_2}{2}\frac{\alpha}{|\alpha|}\right) - \cos\theta_1\sin\theta_2\frac{\beta}{|\beta|}\right]
\end{aligned}$$

3.5 The dipole moment expectation value

The expectation value of the dipole moment in the laboratory frame, $< p >$, is found by the relationship

$$< p >= Tr(\rho \mathbf{p}) \tag{3.50}$$

where Tr refers to the trace of matrix $(\rho \mathbf{p})$ which is the sum of the elements in the leading diagonal, ρ is the density operator matrix for the laboratory frame and p is the dipole operator matrix. In the ground-state tri-level echo sequence, the matrix p has the form

$$\mathbf{p} = \begin{pmatrix} 0 & p_{ab} & p_{ac} \\ p_{ba} & 0 & 0 \\ p_{ca} & 0 & 0 \end{pmatrix}$$

Using the transformation given in equation 3.38 to convert the density matrix given in equation 3.49 to the laboratory frame density matrix $\rho(t)$ gives

$$\rho(t) = \begin{pmatrix} \rho_{aa} & \rho_{ab}e^{i\omega_1 t} & \rho_{ac}e^{i\omega_3 t} \\ \rho_{ba}e^{-i\omega_1 t} & \rho_{bb} & \rho_{bc}e^{i(\omega_3-\omega_1)t} \\ \rho_{ca}e^{-i\omega_3 t} & \rho_{cb}e^{-i(\omega_3-\omega_1)t} & \rho_{cc} \end{pmatrix} (t > t_3)$$

Hence

$$\rho\mathbf{p} = \begin{pmatrix} \rho_{ab}p_{ba}e^{i\omega_1 t} + \rho_{ac}p_{ca}e^{i\omega_3 t} & \rho_{aa}p_{ab} & \rho_{aa}p_{ac} \\ \rho_{bb}p_{ba} + \rho_{bc}p_{ca}e^{i(\omega_3-\omega_1)t} & \rho_{ba}p_{ab}e^{-i\omega_1 t} & \rho_{ba}p_{ac}e^{-i\omega_1 t} \\ \rho_{cb}p_{ba}e^{-i(\omega_3-\omega_1)t} + \rho_{cc}p_{ca} & \rho_{ca}p_{ab}e^{-i\omega_3 t} & \rho_{ca}p_{ac}e^{-i\omega_3 t} \end{pmatrix} \tag{3.51}$$

Applying equation 3.50 gives

$$\begin{aligned} < p > &= \rho_{ab}p_{ba}e^{i\omega_1 t} + \rho_{ac}p_{ca}e^{i\omega_3 t} + \rho_{ba}p_{ab}e^{-i\omega_1 t} + \rho_{ca}p_{ac}e^{-i\omega_3 t} \\ &= \mathcal{P}_{ab} + \mathcal{P}_{ac} \end{aligned} \tag{3.52}$$

where

$$\begin{aligned} \mathcal{P}_{ab} &= \rho_{ab}p_{ba}e^{i\omega_1 t} + \rho_{ba}p_{ab}e^{-i\omega_1 t} \\ \mathcal{P}_{ac} &= \rho_{ac}p_{ca}e^{i\omega_3 t} + \rho_{ca}p_{ac}e^{-i\omega_3 t} \end{aligned} \tag{3.53}$$

Each of the matrix elements of equation 3.49 contains various combinations of the phase factors α, β, γ and their conjugates. Adopting the nomenclature used by Mossberg et al [37], each group of phase terms can be thought of as a 'memory-term'. In order to show the form of these memory terms more clearly consider the case when $\theta_1 = \theta_2 = \theta_3 = \frac{\pi}{2}$. The matrix element ρ_{ab} can then be written

$$\begin{aligned} \rho_{ab} &= \rho^*_{ba} \\ &= \frac{i\sqrt{2}}{8}\frac{\alpha^*}{|\alpha|} + \frac{i\sqrt{2}}{4}\frac{\beta^*}{|\beta|} - \frac{i\sqrt{2}}{8}\frac{\alpha\beta^{*2}}{|\alpha||\beta|^2} \\ &= T^{(1)}_{ab} + T^{(2)}_{ab} + T^{(3)}_{ab} \end{aligned} \tag{3.54}$$

and the matrix element ρ_{ac} can be written

$$\begin{aligned} \rho_{ac} &= \rho^*_{ca} \\ &= \frac{i}{4}\frac{\gamma^*}{|\gamma|} - \frac{i}{8}\frac{\alpha^*\beta\gamma^*}{|\alpha||\beta||\gamma|} - \frac{i}{8}\frac{\alpha\beta^*\gamma^*}{|\alpha||\beta||\gamma|} \\ &= T^{(1)}_{ac} + T^{(2)}_{ac} + T^{(3)}_{ac} \end{aligned} \tag{3.55}$$

Only those memory terms which contain all three phase factors (or their conjugates) go on to produce the echo, and for the ground-state tri-level echo the memory terms are $T^{(2)}_{ac}$ and $T^{(3)}_{ac}$ and the conjugates $T^{(2)}_{ca}$ and $T^{(3)}_{ca}$.

For the excited-state tri-level echo excitation scheme

$$\begin{aligned} < p > &= \rho_{ab}p_{ba}e^{i\omega_1 t} + \rho_{ba}p_{ab}e^{-i\omega_1 t} + \rho_{bc}p_{cb}e^{-i\omega_3 t} + \rho_{cb}p_{bc}e^{i\omega_3 t} \\ &= \mathcal{P}_{ab} + \mathcal{P}_{bc} \end{aligned} \tag{3.56}$$

In this case the only memory terms which contribute to the echo are the $T^{(2)}_{bc}$ ($T^{(2)}_{cb}$) and $T^{(3)}_{bc}$ ($T^{(3)}_{cb}$) terms. With $\theta_1 = \theta_2 = \theta_3 = \frac{\pi}{2}$ these can be written

$$T^{(2)}_{bc} = (T^{(2)}_{cb})^* = \frac{i}{8}\frac{\alpha^*\beta\zeta^*}{|\alpha||\beta||\zeta|} \tag{3.57}$$

$$T^{(3)}_{bc} = (T^{(3)}_{cb})^* = \frac{i}{8}\frac{\alpha\beta^*\zeta^*}{|\alpha||\beta||\zeta|} \tag{3.58}$$

where $\zeta = -p_{bc}\mathcal{E}_3 e^{i\vec{k}_3\cdot\vec{r}_3}$.

This section has shown that the dipole expectation value for the ground-state tri-level echo can be thought to contain the $T_{ab}^{(l)}$ ($T_{ba}^{(l)}$) and $T_{ac}^{(l)}$ ($T_{ca}^{(l)}$) memory terms (where $l = 1, 2, 3$), with corresponding expressions for the excited-state tri-level echo. The next section shows how these memory terms can give rise to coherent emission from the vapour sample after an excitation pulse(s) has occurred.

3.6 Coherent emission from a vapour after excitation

3.6.1 The phase of the dipole moment

As stated in the previous section, the ground-state tri-level photon echo will contain a combination of the phase factors of the three excitation pulses: i.e. the terms in $< p >$ which give rise to the tri-level echo must be the memory terms which contain all three phase factors α, β and γ. The only such terms are $T_{ac}^{(2)}$ and $T_{ac}^{(3)}$, as can be seen from equation 3.55. All the other memory terms which contribute to $< p >$ are connected with free induction decay processes and two-pulse photon echo formation on the $|b> - |a>$ transition.

If $\mathcal{P}_{ac}^{(l)}$ is the dipole moment of the l^{th} memory term then for $\theta_1 = \theta_2 = \theta_3 = \frac{\pi}{2}$

$$\begin{aligned}
\mathcal{P}_{ac}^{(2)} &= p(T_{ca}^{(2)} e^{-i\omega_3 t} + c.c.) \\
&= -p\frac{i}{8}\left(\frac{\alpha\beta^*\gamma}{|\alpha||\beta||\gamma|} e^{-i\omega_3 t} + c.c.\right) \\
&= -p\frac{i}{8}\left(\frac{\mathcal{E}_1 e^{i\vec{k_1}\cdot\vec{r_1}} \mathcal{E}_2^* e^{-i\vec{k_2}\cdot\vec{r_2}} \mathcal{E}_3 e^{i\vec{k_3}\cdot\vec{r_3}}}{|\alpha||\beta||\gamma|} e^{-i\omega_3 t} + c.c.\right) \qquad (3.59)
\end{aligned}$$

where $p_{ac} = p_{ca} = p$. For all other values of θ_n then

$$\mathcal{P}_{ac}^{(2)} = C\left(\frac{\alpha\beta^*\gamma}{|\alpha||\beta||\gamma|} e^{-i\omega_3 t} + c.c.\right) \qquad (3.60)$$

where $C = -p\frac{i}{8}\sin\theta_1 \sin\theta_2 \sin\theta_3$.

Since the phase $\phi_{ac}^{(l)}$ of the dipole moment $\mathcal{P}_{ac}^{(l)}$ is of interest, equation 3.59 can be written

$$\mathcal{P}_{ac}^{(2)} = C(e^{i\phi_{ac}^{(2)}} + c.c.) \qquad (3.61)$$

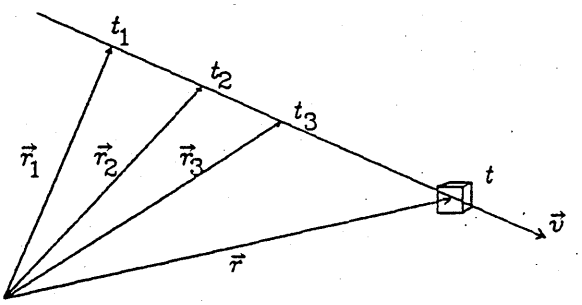

Figure 3.3 The position vector $\vec{r}$ of an atom with constant velocity $\vec{v}$.

where

$$\phi_{ac}^{(2)} = (\vec{k_1}\cdot\vec{r_1} - \vec{k_2}\cdot\vec{r_2}) + \vec{k_3}\cdot\vec{r_3} - \omega_3 t \tag{3.62}$$

This corresponds to the case when the excitation pulses are counterpropagating, as will be shown later (see Figure 3.4). A similar analysis for $\mathcal{P}_{ac}^{(3)}$ yields the phase term $\phi_{ac}^{(3)}$ where

$$\phi_{ac}^{(3)} = -(\vec{k_1}\cdot\vec{r_1} - \vec{k_2}\cdot\vec{r_2}) + \vec{k_3}\cdot\vec{r_3} - \omega_3 t \tag{3.63}$$

and this phase term corresponds to the case when all of the excitation pulses are copropagating. Since all the experiments performed for this thesis use the counterpropagating pulse configuration further analysis will concentrate on $\mathcal{P}_{ac}^{(2)}$ and $\phi_{ac}^{(2)}$ only.

3.6.2 The total radiating dipole moment

For an atom travelling at constant velocity $\vec{v}$, the position $\vec{r}$ of the atom at time t (where $t > t_3$) is related to the positions $\vec{r_m}$ at times t_m (where $m = 1, 2, 3$) by the equation

$$\vec{r} = \vec{r_m} + \vec{v}(t - t_m) \tag{3.64}$$

This relationship is depicted in Figure 3.3. Making $\vec{r_m}$ the subject and substituting into equation 3.62 gives

$$\phi_{ac}^{(2)} = [\vec{k_1}\cdot(\vec{r} - \vec{v}(t - t_1)) - \vec{k_2}\cdot(\vec{r} - \vec{v}(t - t_2))]$$

$$
\begin{aligned}
&+ \vec{k_3}\cdot(\vec{r} - \vec{v}(t - t_3)) - \omega_3 t \\
= \;& [\vec{r}\cdot((\vec{k_1} - \vec{k_2}) + \vec{k_3}) - \omega_3 t] \\
&- \vec{v}\cdot[(\vec{k_1}(t - t_1) - \vec{k_2}(t - t_2)) + \vec{k_3}(t - t_3)] \qquad (3.65)
\end{aligned}
$$

In this expression for $\phi_{ac}^{(2)}$ only the velocity $\vec{v}$ varies from atom to atom in the sample. If at some time t, $\phi_{ac}^{(2)}$ is nearly independent of $\vec{v}$, then the sample is said to exhibit *local coherence* at that time.

Now from equation 3.61

$$
\begin{aligned}
\mathcal{P}_{ac}^{(2)} \;=\; & C e^{i[\vec{r}\cdot((\vec{k_1}-\vec{k_2})+\vec{k_3})-\omega_3 t]} \\
& \times e^{-i\vec{v}\cdot[(\vec{k_1}(t-t_1)-\vec{k_2}(t-t_2))+\vec{k_3}(t-t_3)]} + c.c. \qquad (3.66)
\end{aligned}
$$

Averaging over all atoms at position $\vec{r}$ using the normalised thermal velocity distribution $n(\vec{v})$ where

$$
n(\vec{v}) = \frac{N}{(V_0\sqrt{\pi})^3} e^{-\frac{v^2}{V_0^2}} \qquad (3.67)
$$

(where N is the number of atoms, $V_0^2 = 2k_BT/m$, m is the mass of an atom, k_B is Boltzmann's constant and T is the temperature in Kelvin) gives

$$
\begin{aligned}
\overline{\mathcal{P}}_{ac}^{(2)} \;=\; & C e^{i[\vec{r}\cdot((\vec{k_1}-\vec{k_2})+\vec{k_3})-\omega_3 t]} \\
& \times \frac{1}{N}\int_{-\infty}^{\infty} e^{-i\vec{v}\cdot[(\vec{k_1}(t-t_1)-\vec{k_2}(t-t_2))+\vec{k_3}(t-t_3)]} n(\vec{v}) d\vec{v} + c.c. \qquad (3.68)
\end{aligned}
$$

where

$$
\int_{-\infty}^{\infty} \cdots d\vec{v} = \int_{-\infty}^{\infty}\int_{-\infty}^{\infty}\int_{-\infty}^{\infty} \cdots dv_x dv_y dv_z
$$

since the averaging is equivalent to the integral of equation 3.66 over the normalised thermal velocity distribution. If for some value of t the vector which forms the dot product with $\vec{v}$ in the integrand of equation 3.68 is very small in magnitude i.e.

$$
(\vec{k_1}(t - t_1) - \vec{k_2}(t - t_2)) + \vec{k_3}(t - t_3) \approx 0 \qquad (3.69)
$$

the exponential factor is close to unity and the coherent emission will have its maximum value.

The next section establishes the time t at which equation 3.69 is a minimum.

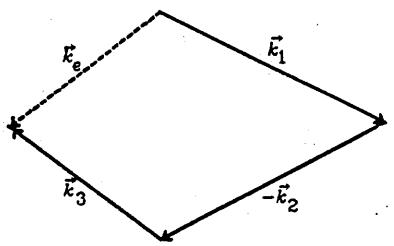

Figure 3.4 Vector diagram of excitation pulse wavevectors showing echo formation from counterpropagating pulses.

3.7 The echo formation time and intensity

3.7.1 The time of echo formation

If $\vec{K}(t)$ represents the left-hand side of equation 3.69 i.e.

$$\vec{K}(t) = (\vec{k_1}(t - t_1) - \vec{k_2}(t - t_2)) + \vec{k_3}(t - t_3) \tag{3.70}$$

then the minimum value of $\vec{K}(t)$ is found from

$$\left.\frac{d|\vec{K}(t)|^2}{dt}\right|_{t_e} = 0 \tag{3.71}$$

The echo wavevector $\vec{k_e}$ is defined by the vector equation (see Figure 3.4)

$$\vec{k_e} = \vec{k_1} - \vec{k_2} + \vec{k_3}$$

Equation 3.70 can be written

$$\begin{aligned} \vec{K}(t) &= \vec{k_e}t - \vec{k_1}t_1 + \vec{k_2}t_2 - \vec{k_3}t_3 \\ &= \vec{k_e}t - \vec{D} \end{aligned} \tag{3.72}$$

where

$$\vec{D} = \vec{k_1}t_1 + \vec{k_2}t_2 - \vec{k_3}t_3$$

Equation 3.71 then yields

$$2k_e^2 t_e - 2\vec{k_e}\cdot\vec{D} = 0$$

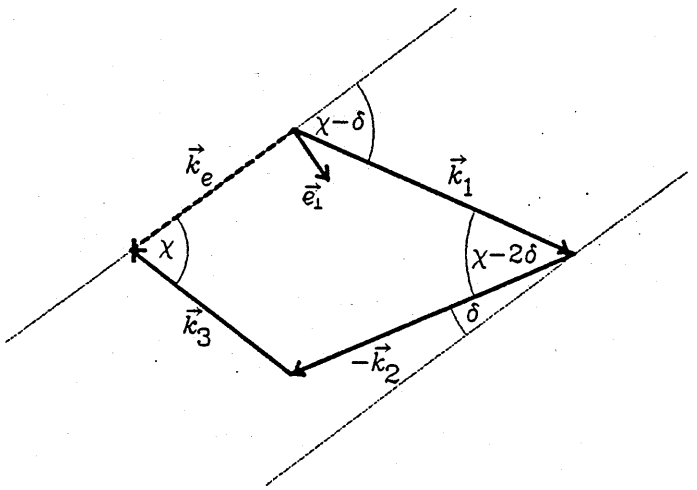

Figure 3.5 Phase-matching diagram for ground-state echo

Hence

$$t_e = \frac{\vec{k_e}\cdot\vec{D}}{k_e^2} \tag{3.73}$$

Writing equation 3.73 in full gives

$$t_e = \frac{\vec{k_e}\cdot\vec{k_1}}{k_e^2}t_1 + \frac{\vec{k_e}\cdot(-\vec{k_2})}{k_e^2}t_2 + \frac{\vec{k_e}\cdot\vec{k_3}}{k_e^2}t_3 \tag{3.74}$$

Setting $t_1 = 0$ and $t_{mn} = t_m - t_n$ enables equation 3.74 to be written

$$t_e = \frac{\vec{k_e}\cdot(-\vec{k_2})}{k_e^2}t_{21} + \frac{\vec{k_e}\cdot\vec{k_3}}{k_e^2}t_3 \tag{3.75}$$

Figure 3.5 shows the phase-matching diagram in more detail (for clarity the angles and differences of wavevector amplitudes are greatly exaggerated). The dot products in equation 3.75 can then be evaluated to give

$$t_e = \frac{|k_e||k_2|}{k_e^2}t_{21}\cos\delta + \frac{|k_e||k_3|}{k_e^2}t_3\cos\chi \tag{3.76}$$

Now $|k_1| = |k_2|$, $|k_3| = |k_e|$ and for $\delta < \chi \ll 1$ this equation reduces to

$$t_e \approx \frac{k_1}{k_3}t_{21} + t_3 \tag{3.77}$$

3.7.2 The relative echo intensity for angled excitation pulses

The expression for the average radiating dipole moment, equation 3.68, can be rewritten

$$\overline{\mathcal{P}}_{ac}^{(2)} = Ce^{i[\vec{r}\cdot((\vec{k_1}-\vec{k_2})+\vec{k_3})-\omega_3 t]} \times \frac{1}{N}\int_{-\infty}^{\infty} e^{-i\vec{v}\cdot\vec{K}(t)} n(\vec{v})d\vec{v} + c.c. \qquad (3.78)$$

and clearly this will be a maximum when $|\vec{K}(t)| = 0$, the case when the excitation pulses are collinear. In this experiment however the pulses are not collinear and so the echo intensity is reduced from its maximum value. Combining equations 3.72 and 3.73 gives

$$\vec{K}(t_e) = \vec{k_e}\left(\frac{\vec{k_e}\cdot(\vec{k_1}t_1 - \vec{k_2}t_2 + \vec{k_3}t_3)}{k_e^2}\right) - \vec{D} \qquad (3.79)$$

Using the unit vectors $\vec{e}_{||}$ (which is parallel to $\vec{k_e}$) and $\vec{e}_{\perp}$ (which is perpendicular to $\vec{k_e}$) and referring to Figure 3.5 gives

$$\begin{aligned}
\vec{K}(t_e) &= \vec{e}_{||}(-k_1\cos(\chi-\delta)t_1 + k_2\cos\delta t_2 + k_3\cos\chi t_3) - \vec{D} \\
&= \vec{e}_{||}(-k_1\cos(\chi-\delta)t_1 + k_2\cos\delta t_2 + k_3\cos\chi t_3) - \vec{k_1}t_1 + \vec{k_2}t_2 - \vec{k_3}t_3 \\
&= \vec{e}_{||}(-k_1\cos(\chi-\delta)t_1 + k_2\cos\delta t_2 + k_3\cos\chi t_3) \\
&\quad -t_1(k_1\sin(\chi-\delta)\vec{e_{\perp}} - k_1\cos(\chi-\delta)\vec{e}_{||}) \\
&\quad +t_2(k_2\sin\delta\vec{e_{\perp}} - k_2\cos\delta\vec{e}_{||}) - t_3(-k_3\sin\chi\vec{e_{\perp}} + k_3\cos\chi\vec{e}_{||}) \\
&= \vec{e_{\perp}}(-k_1t_1\sin(\chi-\delta) + k_2t_2\sin\delta + k_3t_3\sin\chi) \qquad (3.80)
\end{aligned}$$

Clearly $\vec{K}(t_e)$ is perpendicular to $\vec{k_e}$. Setting $t_1 = 0$ and $t_{mn} = t_m - t_n$ as before gives

$$\vec{K}(t_e) = \vec{e_{\perp}}(k_2\sin\delta t_{21} + k_3\sin\chi t_3) \qquad (3.81)$$

Once again, for $\delta < \chi \ll 1$ this reduces to

$$\vec{K}(t_e) = \vec{e_{\perp}}k_3\chi t_3 \qquad (3.82)$$

Using equation 3.67 to substitute for the thermal velocity distribution enables equation 3.78 at time $t = t_e$ to be written

$$\begin{aligned}
\overline{\mathcal{P}}_{ac}^{(2)}(\vec{K}(t_e)) &= Ce^{i[\vec{r}\cdot((\vec{k_1}-\vec{k_2})+\vec{k_3})-\omega_3 t_e]} \times \int_{-\infty}^{\infty} e^{-i\vec{v}\cdot\vec{K}(t_e)} e^{-\frac{m\vec{v}\cdot\vec{v}}{2k_BT}} \frac{d\vec{v}}{(V_0\sqrt{\pi})^3} + c.c. \\
&= Ce^{i[\vec{r}\cdot((\vec{k_1}-\vec{k_2})+\vec{k_3})-\omega_3 t_e]} \times \int_{-\infty}^{\infty} e^{-[\frac{\vec{v}\cdot\vec{v}}{V_0^2}+i\vec{v}\cdot\vec{K}(t_e)]} \frac{d\vec{v}}{(V_0\sqrt{\pi})^3} + (3.83)
\end{aligned}$$

The integral can be easily performed if one 'completes the square' of the exponent i.e.

$$e^{-[\frac{\vec{v}\cdot\vec{v}}{V_0^2}+i\vec{v}\cdot\vec{K}(t_e)]} = e^{-[\frac{\vec{v}}{V_0}+\frac{i}{2}\vec{K}(t_e)V_0]^2} e^{-[\frac{\vec{K}(t_e)V_0}{2}]^2}$$

Setting

$$\vec{u} = \frac{\vec{v}}{V_0} + \frac{i}{2}\vec{K}(t_e)V_0$$

and

$$V_0^3 d\vec{u} = d\vec{v}$$

enables equation 3.83 to be written

$$\begin{aligned}
\overline{\mathcal{P}}_{ac}^{(2)}(\vec{K}(t_e)) &= Ce^{i[\vec{r}\cdot((\vec{k_1}-\vec{k_2})+\vec{k_3})-\omega_3 t_e]} \times \\
&\quad \frac{1}{(\sqrt{\pi})^3}\int_{-\infty}^{\infty} e^{-\vec{u}^2} e^{-[\frac{\vec{K}(t_e)V_0}{2}]^2} d\vec{u} + c.c. \\
&= Ce^{i[\vec{r}\cdot((\vec{k_1}-\vec{k_2})+\vec{k_3})-\omega_3 t_e]} e^{-[\frac{\vec{K}(t_e)V_0}{2}]^2} \times \\
&\quad \frac{1}{(\sqrt{\pi})^3}\int_{-\infty}^{\infty} e^{-\vec{u}^2} d\vec{u} + c.c. \qquad (3.84)
\end{aligned}$$

where the integrals are along lines parallel to and above the real axis giving $\int_{-\infty}^{\infty} e^{-\vec{u}^2} d\vec{u} = \pi^{\frac{3}{2}}$. If $|\vec{K}(t_e)| = 0$ then

$$\begin{aligned}
\overline{\mathcal{P}}_{ac}^{(2)}(0) &= Ce^{i[\vec{r}\cdot((\vec{k_1}-\vec{k_2})+\vec{k_3})-\omega_3 t_e]} \times \frac{1}{(\sqrt{\pi})^3}\int_{-\infty}^{\infty} e^{-\vec{w}^2} d\vec{w} + c.c. \\
&= Ce^{i[\vec{r}\cdot((\vec{k_1}-\vec{k_2})+\vec{k_3})-\omega_3 t_e]} \qquad (3.85)
\end{aligned}$$

where $\vec{w} = \vec{v}/V_0$. Equations 3.84 and 3.85 are important results because, for an optically thin sample, the echo intensity $I \propto |\overline{\mathcal{P}}_{ac}^{(2)}|^2$, i.e.

$$\begin{aligned}
I &\propto C^2 \\
&\propto \frac{p^2}{64}\sin^2\theta_1 \sin^2\theta_2 \sin^2\theta_3 \qquad (3.86)
\end{aligned}$$

Thus

$$\frac{|\overline{\mathcal{P}}_{ac}^{(2)}(\vec{K}(t_e))|}{|\overline{\mathcal{P}}_{ac}^{(2)}(0)|} = e^{-[\frac{\vec{K}(t_e)V_0}{2}]^2} \qquad (3.87)$$

The echo intensities I are related by

$$I(\vec{K}(t_e)) = e^{-\frac{(\vec{K}(t_e)V_0)^2}{2}} I(0) \qquad (3.88)$$

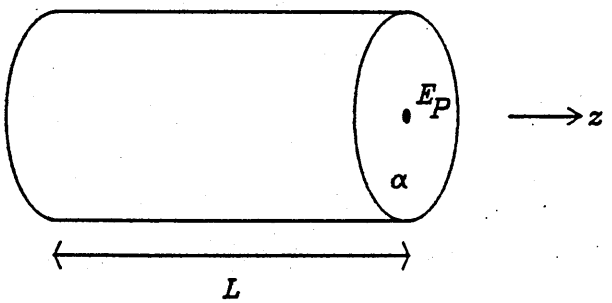

Figure 3.6 Cylinder of length L and cross-sectional area α.

where $I(0) \propto |\overline{\mathcal{P}}_{ac}^{(2)}(0)|^2$. In the experiments performed in this thesis, $V_0 \approx 200\text{ms}^{-1}$, and from equation 3.82 typically $|\vec{K}(t_e)| \approx 1.5\chi$. Substituting these values in equation 3.88 yields

$$I(\vec{K}(t_e)) \approx e^{-\frac{9\chi^2}{200}} I(0)$$

where here χ is measured in mrad. Typically $\chi \simeq 5$ mrad, giving $I(\vec{K}(t_e)) \approx 0.3I(0)$.

3.8 The absolute echo intensity

This section establishes the total energy in an echo pulse formed from a cylindrical volume of gas using optimum pulse areas. The analysis is based on the method of Fresnel half period zones. The atoms are assumed to radiate like classical hertzian dipoles.

Figure 3.6 shows a cylindrical sample which is emitting an echo pulse in the positive z-direction, and the following analysis considers a cross section of this sample of thickness δz, where $\delta z \ll \lambda$. In order to find the net radiation field at an axial point, P, a distance R from the section, it is useful to divide the section into half period zones.

Figure 3.7 shows the first two such zones. The first Fresnel zone is the disc of radius $\sqrt{R\lambda}$ centred at O. The second Fresnel zone is the annulus of inner radius $\sqrt{R\lambda}$ and outer radius $\sqrt{2R\lambda}$. All the half period zones have equal areas of $\pi R\lambda$, and therefore contain the same number of atoms. The

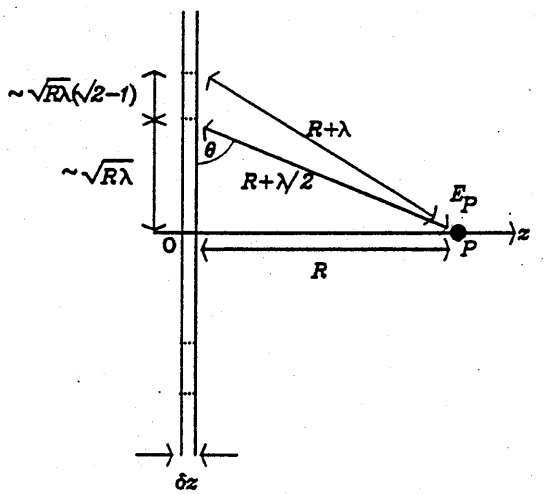

Figure 3.7 Cylindrical section of thickness δz. All atoms within the sample are radiating in phase.

phase of the radiation received at P from atoms on the circumference of the first zone is π behind that received from atoms at the centre.

Let the phase of the E field at P emitted by an atom at the centre of the section be represented by a horizontal phasor. Then Figure 3.8(i) shows the sum of the E field phasors at P for the atoms in the first zone. As one can see, the resultant phasor due to the first half period zone is retarded in phase by $\frac{\pi}{2}$ with respect to the phasor for radiation from atoms at the centre. Figure 3.8(ii) shows the resultant E field phasor for the first two Fresnel half period zones. The magnitude of the resultant phasor from the second half period zone is slightly smaller than that of the first because the distances to P are larger, and the angles θ from P to the atomic dipoles are smaller. Figure 3.8(iii) shows the resultant E field phasor as the number of zones is increased and the section is extended indefinitely. In fact, edge effects due to a finite sample profile, ragged on the scale of an optical wavelength, give rise to the same resultant field at P.

For a single dipole at the zone centre, O, radiating at frequency ω, the amplitude of the E field measured at P is given by the classical dipole

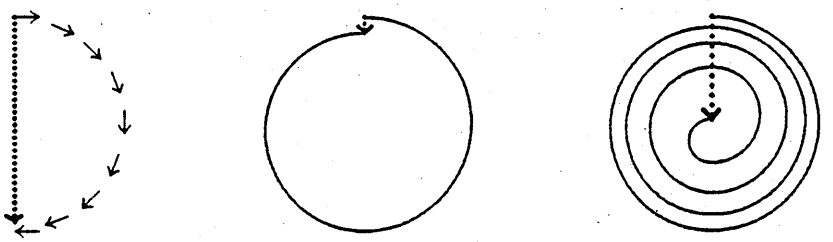

(*i*) (*ii*) (*iii*)

Figure 3.8 Phasor diagrams for the resultant E field at P emitted by a cylindrical sample: (*i*) resultant phasor for the first Fresnel half period zone; (*ii*) resultant phasor for the first and second Fresnel half period zones; (*iii*) resultant phasor for an infinitely large section.

formula

$$\frac{\omega^2 p \sin\theta}{4\pi\epsilon_0 c^2 R} \tag{3.89}$$

where p is the amplitude of the dipole moment and θ is shown in Figure 3.7. If there are n atoms per unit volume then the field for the first half period zone is given by

$$\pi(\sqrt{R\lambda})^2 \delta z n \times \frac{\omega^2 p}{4\pi\epsilon_0 c^2 R} \times \frac{2}{\pi} = \frac{nkp\delta z}{\epsilon_0} \tag{3.90}$$

where k is the wave number, the factor $\frac{2}{\pi}$ is the ratio of the diameter (resultant phasor) to the half-circumference, and it is assumed that $R \gg \lambda$ so $\sin\theta \approx 1$ for all atoms in the zone. One can see from Figure 3.8(*iii*) that the resultant field amplitude at P due to the whole section is half that due to the first half period zone alone, thus the field due to the whole section shown in Figure 3.7 is given by half the field of equation 3.90. Then

$$\delta E_P = \frac{kpn\delta z}{2\epsilon_0} \tag{3.91}$$

Since this result is independent of R, the resultant phasor amplitude at P for a cylinder of length L

$$E_P = \frac{kpnL}{2\epsilon_0} \tag{3.92}$$

Now the Poynting vector, which determines the time averaged energy flow rate and its direction, is given by

$$\vec{S} = \frac{1}{2}\vec{E}_0 \wedge \vec{H}_0$$

where E_0 and H_0 are the amplitudes of the electromagnetic wave, thus

$$\begin{aligned} |\vec{S}| &= \frac{1}{2}|\vec{E}_0 \wedge \vec{H}_0| \\ &= \frac{1}{2\mu_0}|\vec{E}_0 \wedge \vec{B}_0| \\ &= \frac{E_0^2}{2\mu_0 c} \end{aligned}$$

Hence, for a cylinder of length L and cross-sectional area α (see Figure 3.6) the total power emerging, W, is given by

$$\begin{aligned} W &= \frac{E_P^2 \alpha}{2\mu_0 c} \\ &= \frac{n^2 k^2 p^2 L^2 c \alpha}{8\epsilon_0} \end{aligned} \tag{3.93}$$

If the echo duration is t_p, then the number of photons in an echo, $\mathcal{N}$, is simply

$$\begin{aligned} \mathcal{N} &= \frac{W t_p}{h\nu} \\ &= \frac{n^2 p^2 L^2 \pi k \alpha t_p}{4\epsilon_0 h} \end{aligned} \tag{3.94}$$

Taking p to be the matrix element of the electric dipole moment operator for the transition involved, and using the relationship [83]

$$|p|^2 = \frac{A 3\pi\epsilon_0 \hbar c^3 g_2}{\omega^3 g_1}$$

where A is the Einstein rate coefficient for the transition, and g_1 and g_2 are the level degeneracies. Equation 3.94 becomes

$$\begin{aligned} \mathcal{N} &= \frac{n^2 p^2 L^2 \pi k \alpha t_p}{4\epsilon_0 h} \frac{A 3\pi\epsilon_0 \hbar c^3 g_2}{\omega^3 g_1} \\ &= \frac{3n^2 L^2 \lambda^2 \alpha t_p A g_2}{32\pi g_1} \end{aligned} \tag{3.95}$$

For the experiments performed for this thesis, typical values for the various factors of equation 3.95 are $n \simeq 10^{16}$ m^{-3}, $L \simeq 0.01$ m, $\lambda \simeq 500 \times 10^{-9}$ m, $\alpha \simeq 4 \times 10^{-6}$ m^2, $t_p \simeq 1$ ns, $A \simeq 10^7$ s^{-1} and $\frac{g_1}{g_2} \simeq 1$, which combine to give $\mathcal{N} \simeq 10^7$ photons.

3.9 The rôle of velocity modulated populations in echo experiments

It was stated in Subsection 1.3.4 that unlike the two pulse photon echo the three pulse photon echo can be used to study the effects of collisional mechanisms which are otherwise masked by optical coherence destroying effects. As pointed out in Section 1.4, in the interval t_{32}, the components of orientation and alignment of both ground and excited state levels when excited by similar pulses are modulated in velocity space.

For the 3 × 3 laboratory frame density matrix

$$\rho(t) = \begin{pmatrix} \rho'_{aa} & \rho'_{ab} & \rho'_{ac} \\ \rho'_{ba} & \rho'_{bb} & \rho'_{bc} \\ \rho'_{ca} & \rho'_{cb} & \rho'_{cc} \end{pmatrix}$$

(assuming non-degenerate levels for simplicity) the terms on the leading diagonal describe the populations for the various levels (ρ_{aa} gives the population of state $|a>$ etc.). The off-diagonal terms describe the optical coherences that exist between states.

If one considers the effect of individual excitation pulses on the density matrix, then after the first excitation pulse in the ground-state tri-level echo excitation sequence, $\rho(t)$ is given by transforming Equation 3.46 to the laboratory frame giving

$$\rho(t) = \begin{pmatrix} c_1^2 & \frac{i}{2}\frac{\alpha^*}{|\alpha|}S_1 e^{i\omega_1 t} & 0 \\ -\frac{i}{2}\frac{\alpha}{|\alpha|}S_1 e^{-i\omega_1 t} & s_1^2 & 0 \\ 0 & 0 & 0 \end{pmatrix} (t > t_1)$$

where $s_n = \sin\frac{\theta_n}{2}$, $S_n = \sin\theta_n$ and similar terms apply for the cosines. The dipole moment $< p >$ after the first pulse is found from equation 3.50 to be

$$< p >= p_{ba}\frac{i}{2}\frac{\alpha^*}{|\alpha|}S_1 e^{i\omega_1 t} + c.c.$$

This is simply the FID (free induction decay) of the first excitation pulse. The population terms are dependent upon the pulse area only.

After the second excitation pulse, the laboratory frame density matrix becomes

$$\rho(t) = \begin{pmatrix} \rho'_{aa} & \rho'_{ab} & 0 \\ \rho'_{ba} & \rho'_{bb} & 0 \\ 0 & 0 & 0 \end{pmatrix} (t > t_2)$$

where

$$\begin{aligned}
\rho'_{aa} &= c_1^2 c_2^2 + s_1^2 s_2^2 - \frac{1}{4} S_1 S_2 \left(\frac{\alpha^* \beta + \alpha \beta^*}{|\alpha||\beta|}\right) \\
\rho'_{bb} &= c_1^2 s_2^2 + s_1^2 c_2^2 + \frac{1}{4} S_1 S_2 \left(\frac{\alpha^* \beta + \alpha \beta^*}{|\alpha||\beta|}\right) \\
\rho'_{ab} &= \rho^*_{ba} = \frac{i}{2} \frac{\alpha^*}{|\alpha|} S_1 c_1^2 e^{i\omega_1 t} + \frac{i}{2} \frac{\beta^*}{|\beta|} C_1 S_1 e^{i\omega_1 t} - \frac{i}{2} \frac{\alpha \beta^{*2}}{|\alpha||\beta|^2} S_1 s_1^2 e^{i\omega_1 t}
\end{aligned}$$

The dipole moment after the second pulse is then

$$\begin{aligned}
< p > &= p_{ba} \frac{i}{2} \frac{\alpha^*}{|\alpha|} S_1 c_1^2 e^{i\omega_1 t} + p_{ba} \frac{i}{2} \frac{\beta^*}{|\beta|} C_1 S_1 e^{i\omega_1 t} - \\
& \quad p_{ba} \frac{i}{2} \frac{\alpha \beta^{*2}}{|\alpha||\beta|^2} S_1 s_1^2 e^{i\omega_1 t} + c.c.
\end{aligned}$$

The first and second terms correspond to the FID of the atoms after the first and second excitation pulses respectively; the third term corresponds to a two-pulse photon echo.

If one sets $\theta_1 = \theta_2 = \frac{\pi}{2}$ for simplicity, the population terms for the density matrix after the second pulse become

$$\begin{aligned}
\rho'_{aa} &= \frac{1}{2} - \frac{1}{4} \left(\frac{\alpha^* \beta + \alpha \beta^*}{|\alpha||\beta|}\right) \\
\rho'_{bb} &= \frac{1}{2} + \frac{1}{4} \left(\frac{\alpha^* \beta + \alpha \beta^*}{|\alpha||\beta|}\right)
\end{aligned}$$

Now

$$\begin{aligned}
\frac{\alpha^* \beta + \alpha \beta^*}{|\alpha||\beta|} &= \frac{p_{ab} \mathcal{E}_1 e^{-i\vec{k_1} \cdot \vec{r_1}} p_{ba} \mathcal{E}_2 e^{i\vec{k_2} \cdot \vec{r_2}} + c.c.}{|p_{ba} \mathcal{E}_1 e^{i\vec{k_1} \cdot \vec{r_2}}||p_{ba} \mathcal{E}_2 e^{i\vec{k_2} \cdot \vec{r_2}}|} \\
&= e^{i(\vec{k_1} \cdot \vec{r_1} - \vec{k_2} \cdot \vec{r_2})} + c.c. \\
&= 2 \cos(\vec{k_1} \cdot \vec{r_1} - \vec{k_2} \cdot \vec{r_2})
\end{aligned}$$

For $\vec{k} = \vec{k_1} = \vec{k_2}$, where $k \parallel z$, using equation 3.64 yields

$$\begin{aligned}\frac{\alpha^*\beta + \alpha\beta^*}{|\alpha||\beta|} &= 2\cos[\vec{k_1}\cdot(\vec{r} - \vec{v}(t - t_1)) - \vec{k_2}\cdot(\vec{r} - \vec{v}(t - t_2))] \\ &= 2\cos kv_z t_{21}\end{aligned}$$

Hence

$$\begin{aligned}\rho'_{aa} &= \frac{1}{2}(1 - \cos kv_z t_{21}) = \sin^2(\frac{kv_z t_{21}}{2}) \\ \rho'_{bb} &= \frac{1}{2}(1 + \cos kv_z t_{21}) = \cos^2(\frac{kv_z t_{21}}{2})\end{aligned}$$

However, $k = 2\pi/\lambda$, so substituting this into the population terms above gives

$$\begin{aligned}\rho'_{aa} &= \sin^2(\frac{v_z \pi t_{21}}{\lambda}) = \sin^2(\pi\frac{v_z}{V_m}) \\ \rho'_{bb} &= \cos^2(\pi\frac{v_z}{V_m})\end{aligned}$$

where V_m, the period of modulation, is given by $V_m = \lambda/t_{21}$. Thus, one of the effects of this two-pulse excitation sequence is to produce modulated velocity distributions of the populations in the two states $|a>$ and $|b>$, the period of which can be altered by simply varying t_{21}, the interpulse time. The implications of this are dealt with more fully in Section 6.3.

From equation 3.49 one can see that density matrix element, ρ_{ac} (and ρ_{ca}), from which the memory term responsible for forming the ground-state tri-level echo is derived, contains a term which relates to the modulated ground state population immediately after the second pulse, ρ_{aa}, (see equation 3.48). The echo therefore is formed from the modulation stored during t_{32} in the ground state population.

For an excited-state tri-level echo (see Figure 1.23(b)), the relevant density matrix element, ρ_{bc} (and ρ_{cb} — see equation 3.56), contains information about the modulations in the excited state population immediately after the second excitation pulse (this is shown explicitly in Appendix A).

In the case of the stimulated echo (see Figure 1.23(c)), the relevant density matrix element, ρ_{ab} (and ρ_{ba}), contains information about modulations

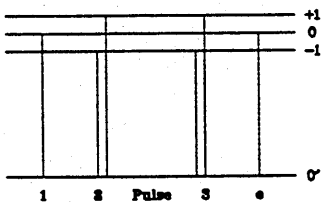

Figure 3.9 Formation of a stimulated echo from a four level atom.

in both the ground and excited state populations (in fact it contains a term describing the inversion $(\rho_{bb} - \rho_{aa})$ — see Appendix A).

3.10 The rotating frame density matrix for the echo experiments performed in this thesis

As mentioned earlier, the experiments conducted for this thesis use polarised excitation pulses and excite different degenerate Zeeman sublevels of the excited and ground states.. For the purpose of illustration, consider a four level atom subjected to three excitation pulses, as shown in Figure 3.9 (this is the same level system as that used by Yodh et al [77]). The density matrix analysis will be further simplified by setting all of the coefficients of the M matrices to unity to produce phase matrices, following the notation used by Mossberg et al [37]. The phase matrix for the first pulse is given by

$$\mathrm{M}_{10' \leftrightarrow 0} = \mathrm{M}^{-1}_{10' \leftrightarrow 0} = \begin{pmatrix} 1 & 0 & \alpha^* & 0 \\ 0 & 1 & 0 & 0 \\ \alpha & 0 & 1 & 0 \\ 0 & 0 & 0 & 1 \end{pmatrix} \tag{3.96}$$

The M matrices for the second and third pulses are given by

$$\mathrm{M}_{20' \leftrightarrow -1,+1} = \mathrm{M}^{-1}_{20' \leftrightarrow -1,+1} = \begin{pmatrix} 1 & \beta^* & 0 & \gamma^* \\ \beta & 1 & 0 & 0 \\ 0 & 0 & 1 & 0 \\ \gamma & 0 & 0 & 1 \end{pmatrix} \tag{3.97}$$

and

$$\mathrm{M}_{30'\leftrightarrow -1,+1} = \mathrm{M}^{-1}_{30'\leftrightarrow -1,+1} = \begin{pmatrix} 1 & b^* & 0 & c^* \\ b & 1 & 0 & 0 \\ 0 & 0 & 1 & 0 \\ c & 0 & 0 & 1 \end{pmatrix} \tag{3.98}$$

The phases α, β and b, γ and c refer to the first, second and third excitation pulses only. The resultant phase matrix after the third pulse is given by

$$\rho_\omega(t_3) = \begin{pmatrix} \rho_{0'0'} & \rho_{0'-1} & \rho_{0'0} & \rho_{0'+1} \\ \rho_{-10'} & \rho_{-1-1} & \rho_{-10} & \rho_{-1+1} \\ \rho_{00'} & \rho_{0-1} & \rho_{00} & \rho_{0+1} \\ \rho_{+10'} & \rho_{+1-1} & \rho_{+10} & \rho_{+1+1} \end{pmatrix} \tag{3.99}$$

where

$$\begin{aligned}
\rho_{0'0'} &= 1 + \beta^* b + \beta b^* + \gamma^* c + \gamma c^* + \beta\gamma^* b^* c + \beta^*\gamma b c^* \\
\rho_{-1-1} &= 1 + \beta^* b + \beta b^* \\
\rho_{00} &= 1 \\
\rho_{11} &= 1 + \gamma^* c + \gamma c^* \\
\rho_{0'-1} &= \rho^*_{0'-1} = b^*(1 + \beta b^*) + \gamma c^*(b^* + \beta^*) + \beta^* \\
\rho_{0'0} &= \rho^*_{0'0} = \alpha^*(1 + \beta b^* + \gamma c^*) \\
\rho_{0'+1} &= \rho^*_{0'+1} = c^*(1 + \gamma c^*) + \gamma^* + \beta b^*(\gamma^* + c^*) \\
\rho_{-10} &= \rho^*_{-10} = \alpha^*(\beta + b) \\
\rho_{-1+1} &= \rho^*_{-1+1} = (\beta + b)(\gamma^* + c^*) \\
\rho_{0+1} &= \rho^*_{+10} = \alpha(\gamma^* + c^*)
\end{aligned}$$

The echo is formed on the $0' \leftrightarrow 0$ transition (the corresponding phase factors are $\alpha^*(\beta b^* + \gamma c^*)$ and $\alpha(\beta^* b + \gamma^* c)$). Yodh et al [77] have shown how the echo amplitude can be expressed in terms of components of the orientation and alignment of the Zeeman levels. These components contain sine and cosine modulations of the factor kvt_{21} from which the echo is generated. This is however a simplfied picture of the stimulated echo experiments conducted for this thesis, since for caesium both the excited and ground states are degenerate.

Chapter 4

The equipment used for three-pulse photon echo experiments

This chapter describes the equipment used in the experiment, concentrating in detail on various aspects of the apparatus. Section 4.1 deals with the lasers which generate the excitation pulses, whilst Section 4.2 describes the optical bench configuration and major components contained therein. The detection system employed is discussed in Section 4.3. Section 4.4 covers the caesium oven and its associated maintenance, whilst a description of the vacuum system and perturber gas pressure regulation is given in Section 4.5.

4.1 The optical excitation pulse sources

The excitation pulses are produced by two dye lasers, which are both pumped by a pulsed nitrogen laser (a *Molectron UV12*) which operates at 337 nm and has a nominal pulse duration of $\approx$ 10 ns. Of the two dye lasers used, one is a commercially manufactured unit (a *Molectron DL14P*) and the other is an in-house grazing incidence type laser (hereafter referred to as a GIL (Grazing Incidence Laser)). The cavity arrangements for the DL14P and the GIL are depicted in Figure 4.1 and Figure 4.2 respectively. Fine-tuning of the DL14P is performed by rotating the intra cavity etalon, whereas fine-tuning of the GIL is carried out by rotating the optical flat: for both lasers coarse-tuning is performed by rotating the diffraction gratings.

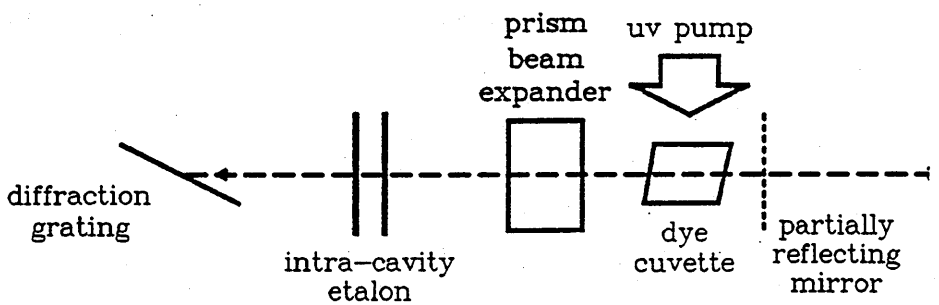

Figure 4.1 Cavity arrangement of the DL14P dye laser — note the diffraction grating in the conventional Littrow configuration.

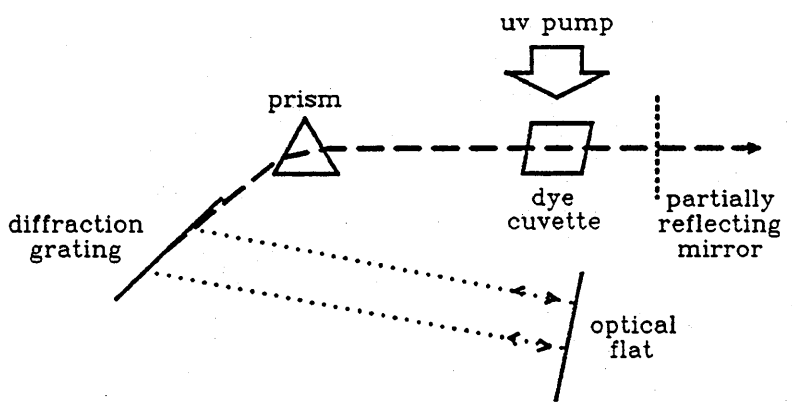

Figure 4.2 Cavity arrangement of the grazing incidence type dye laser — note the angle of the diffraction grating

Figure 4.3 is an energy level diagram for the caesium transitions ($6S_{\frac{1}{2}} \leftrightarrow 7P_{\frac{1}{2},\frac{3}{2}}$) used in this thesis. As the wavelengths of the two transitions of interest are similar (455.5 nm and 459.3 nm) both dye lasers use the same dye solution. The dye used is 7-diethylamino-4-methylcoumarin — also known as 'Coumarin 460' and 'Coumarin 1' depending on the manufacturer — which has a peak operating wavelength of 457 nm; it is dissolved at 0.01 molar strength (2.31 g/li) in research grade ethanol, the resulting liquid appearing a pale, transparent, fluorescent yellow/blue when viewed under fluorescent lighting (when the dye is exhausted it loses this fluorescent quality and turns a dark, transparent yellow). The DL14P uses a single cuvette of dye with a magnetically driven rotor at the bottom to ensure agitation of

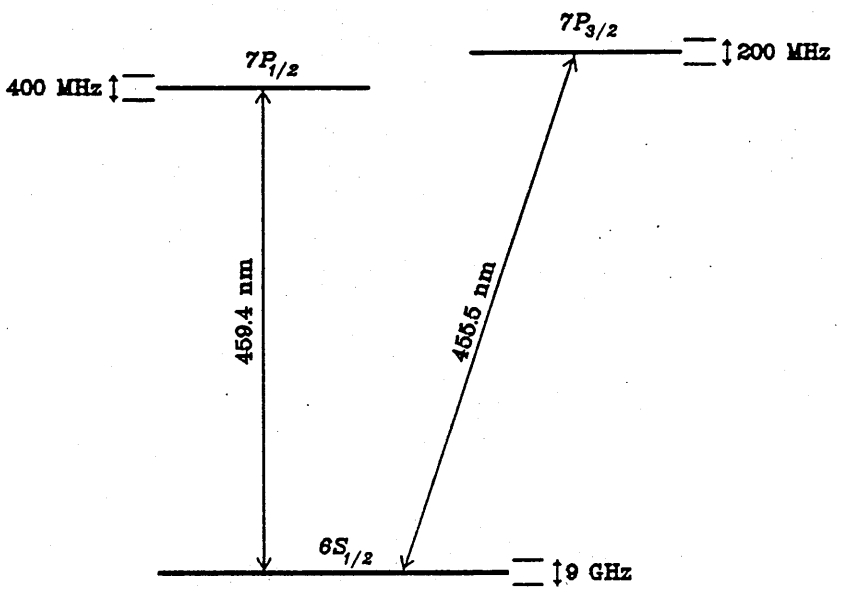

Figure 4.3 Energy level diagram for the caesium transitions $6S_{\frac{1}{2}} \leftrightarrow 7P_{\frac{1}{2},\frac{3}{2}}$.

the gain medium, and the GIL employs a flowing dye cell which is connected to a large (0.25 litre) reservoir.

The uv output from the nitrogen laser is split into two beams in the intensity ratio 1 : 3, with the weaker portion pumping the DL14P. Using a Laser Precision RJ-7620 Energy Ratiometer in conjunction with an RjP 735 pyroelectric probe, the maximum energy per pulse (averaged over 100 pulses) obtained from the nitrogen laser before splitting was $\approx$ 1 mJ when the beam was focussed down on to the probe: this was achieved for a pulse repetition rate of 20 Hz. The dye lasers both have a pulse duration of $\approx$7 ns which is shorter than the N_2 laser pulse for two reasons. Firstly, the dye population inversion is achieved during most, but not all, of the pump pulse (the pump pulse must attain sufficient intensity to exceed the threshold value of the dye for 'lasing' action to occur). Secondly, it takes approximately one cavity round trip time for the dye laser beam to build up, and for both dye lasers this is of the order of 1.5 ns. Again, using the energy ratiometer, the output energies per pulse of the dye lasers were measured (after they had been restricted by apertures to beam diameters of about 2 mm) to be $\approx$100

nJ. The DL14P output is partially plane polarised, with a polarisation ratio of about 20:1, and the GIL output exhibits no preferred polarisation plane.

4.2 The optical system

4.2.1 The optical bench configuration

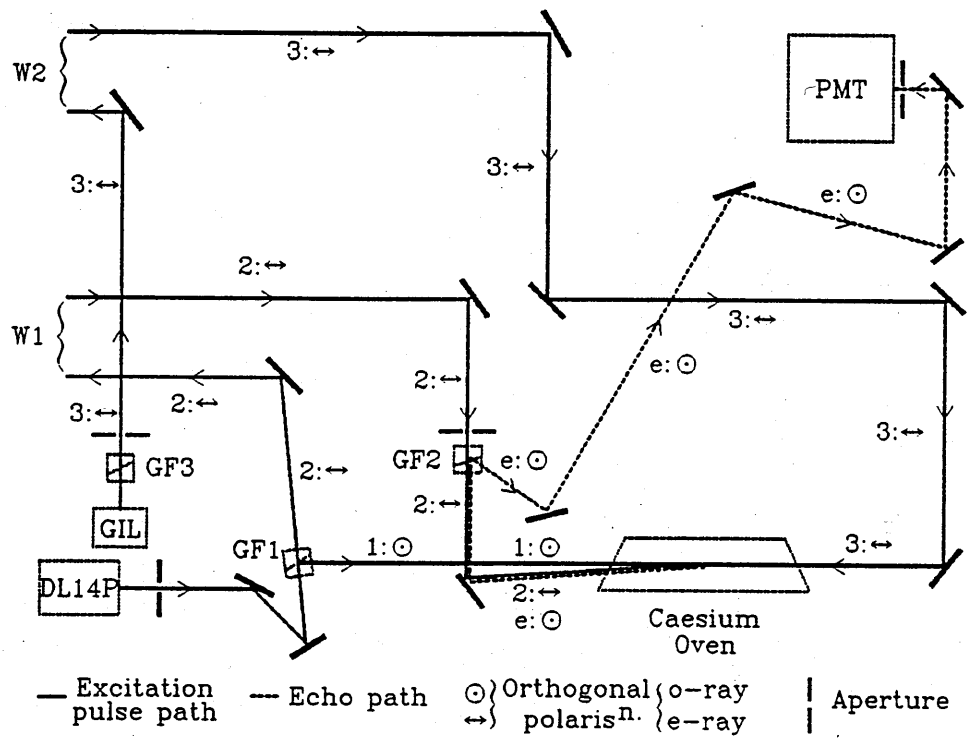

Figure 4.4 Schematic diagram of the optical bench arrangement. The three excitation pulses and the echo are labelled 1,2,3 and *e* respectively, W1,2 are White cells, GF1,2,3 are Glan-Foucault prisms and PMT is a photomultiplier tube.

A schematic diagram of the optical bench configuration for the three pulse echo experiments described in Section 1.5 is given in Figure 4.4. This optical arrangement is similar to one employed by Fujita et al [66] in their work on sodium. The three excitation pulses are provided by the two lasers described

above, with the first two pulses — referred to as pulse 1 and pulse 2 respectively — originating from the same laser (DL14P). Glan-Foucault polarising prisms are used as beam splitters, since the polarisation of the beams is an important aid in discriminating the echo pulse from the excitation pulses. Hence, when the pulse from the DL14P reaches the first polariser (GF1) it is split into two orthogonally polarised beams. Pulse 1 then goes to the oven via an aperture.

Pulse 2, however, is directed to a White cell optical delay line, labelled W1 in Figure 4.4, (a full description of a White cell is given in Subsection 4.2.2), after which it is directed through another Glan-Foucault prism (GF2) before being directed into the caesium oven. Pulse 2 enters the oven at a slight angle to pulse 1 ($\approx$ 5 mrad), with the pulses overlapping in the centre of the oven. Pulses 1 and 2 have beam diameters of about 2 mm and pulse energies of $\approx$10–15 nJ as they enter the oven.

The third excitation pulse (labelled 3 in Figure 4.4) is produced by the GIL and first passes through a Glan-Foucault prism which has been set so that pulses 2 and 3 are identically plane-polarised. The beam is then directed into a second White cell (labelled W2 in Figure 4.4) before being directed into the caesium oven so that it exactly counter-propagates with pulse 1.

The photon echo formed from this excitation pulse sequence is exactly counter-propagating with and orthogonally polarised to pulse 2. Thus, the echo pulse is directed back along the path of pulse 2 until it reaches GF2, where it is internally reflected and emerges from the side. The echo is then directed into the PMT (photo-multiplier tube) via a pin-hole.

In order to maintain the polarisation properties of the beams as much as possible, metallic mirrors are used between the lasers and the caesium oven whenever the angle of incidence is *not* near normal (dielectric mirrors can however be used when the angle of incidence is near normal).

As the echo pulse is very much smaller in intensity ($\approx 10^{-7} - 10^{-6}$) than the excitation pulses at the oven, care has to be taken to minimise the amount of stray, scattered light from optical components, apertures

etc., that reaches the PMT in order to avoid saturation. To this effect, two separate techniques are employed in the experimental arrangement described above: spatial filtering through the use of beam angling and apertures, and polarisation discrimination (see Figure 4.4).

Spatial filtering significantly reduces the amount of radiation from the excitation pulses and stray light that reaches the PMT, since none of the excitation pulses travels in exactly the same direction as the echo, and any stray light which may happen to travel in a similar direction is attenuated by the apertures. The Glan-Foucault prisms further reduce the intensity of pulse 3 seen at the PMT (and to a lesser extent any other light that may take the same oven-PMT path as the echo), since the majority of any radiation from pulse 3 (which has a propagation direction nearest to that of the echo) will be blocked off by GF2, due to the orthogonal polarisations of pulse 3 and the echo.

Polarisation discrimination is needed in addition to spatial filtering because, as was explained in Subsection 3.7.2, the echo intensity quickly reduces with increasing beam separation angle, so there is a compromise between minimising the amount of light from pulse 3 which reaches the PMT, and maximising the echo intensity at the PMT: the optimum separation angle for pulses 1 & 2 for the experiment was found to be $\approx$5 mrad, which reduces the echo intensity to $\approx e^{-1}$ of the maximum possible intensity. An aperture near the PMT (which is enclosed in a light-tight box with a pin-hole entrance) further reduces the effects of stray light and promotes discrimination of excitation pulse intensity in favour of the echo.

The results obtained with these two simple discrimination techniques are however comparable to those that can be obtained by electro-optic shuttering, and are obtained at much lower cost and far greater simplicity.

4.2.2 The White cell variable optical delay line.

The White cell is a simple, but efficient, variable optical delay line designed by White [84] which consists of three converging mirrors of the same radius of curvature. Two of these mirrors are of similar size, but smaller than the

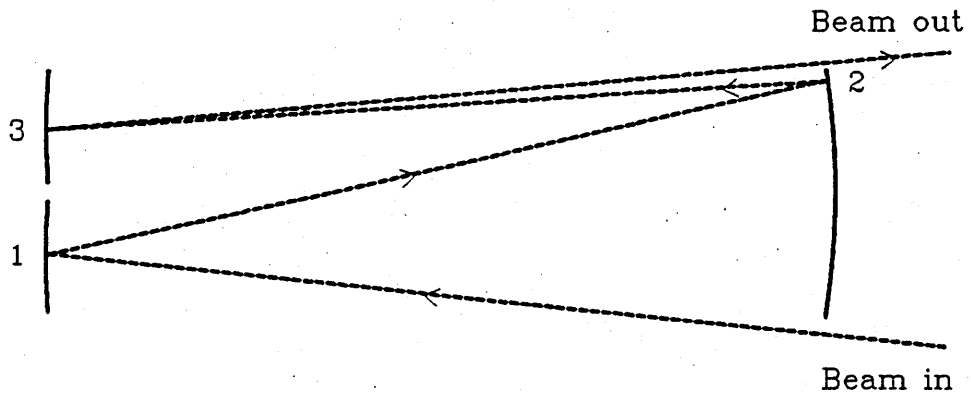

Figure 4.5 Schematic diagram of a White cell

third. The two smaller mirrors are placed opposite the larger mirror in such a way that the centre of curvature of the large mirror lies midway between them, and that their respective centres of curvature lie on the surface of the larger mirror. This arrangement is depicted in Figure 4.5.

The White cell is aligned for use in the following manner. The light beam enters the cell by passing as close as possible to the edge of the larger mirror whilst impinging upon the centre of the first small mirror (marked '1' on Figure 4.5). This smaller mirror is then orientated so that the reflected beam strikes the larger mirror near the opposite edge (marked '2' on Figure 4.5) to that which the light beam first passed. The large mirror is then in turn adjusted so that the reflected beam strikes the centre of the second small mirror (labelled '3' on Figure 4.5). Finally, this second small mirror is rotated so that the reflected beam of light emerges from the White cell passing close to the large mirror edge but on the opposite side to that which it passed on entry. This simple procedure has fully aligned the White cell which is now in its smallest delay mode.

In order to increase the optical delay it is necessary only to rotate the second small mirror to bring its axis towards the centre of the large mirror. With a very small angular displacement an extra four reflections between the mirrors can be obtained, as shown on Figure 4.6. The light enters the White cell as before and then bounces between the mirrors in the numerical

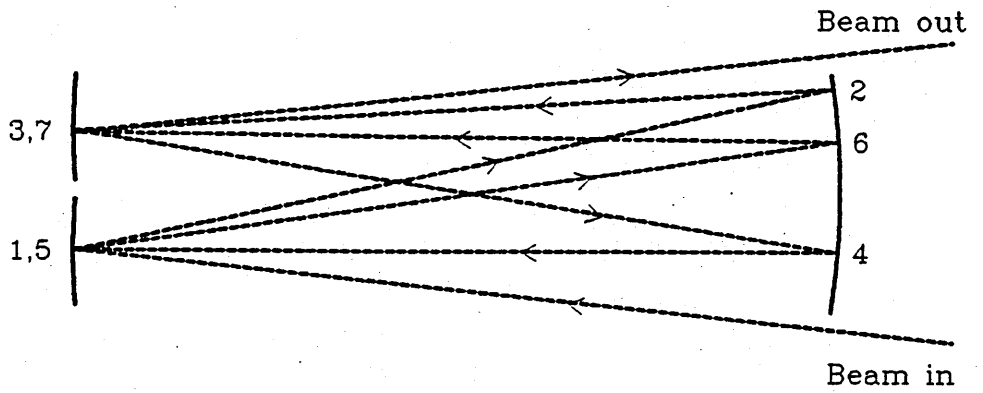

Figure 4.6 Here an extra delay of four passes between the mirrors has been obtained by rotating the top lefthand mirror clockwise by a small amount.

order shown before exiting again. Further small rotations of the second small mirror in the same direction as the previous adjustment introduce further multiples of four bounces, and it is quite easy to achieve 28 transits between the mirror faces.

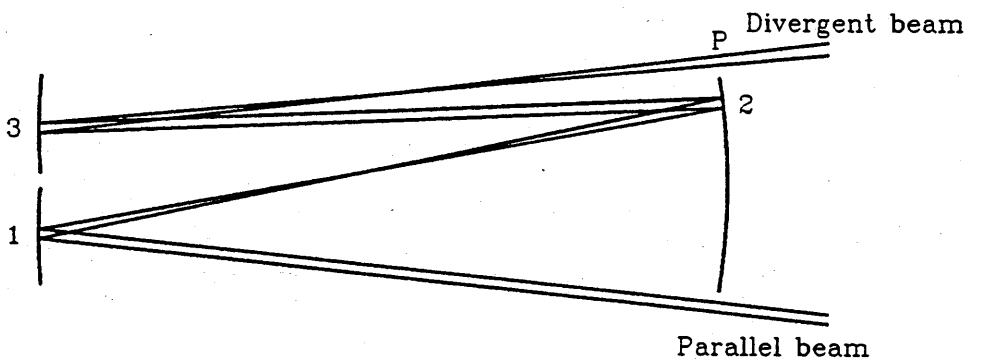

Figure 4.7 A parallel ray entering the White cell becomes divergent on exit.

However, when a parallel beam enters a White cell it becomes divergent on exit, the degree of divergence being dependent on the radius of curvature of the particular mirrors used — this divergence is indicated in Figure 4.7. This condition is easily rectified by placing (at point P on Figure 4.7) a converging lens of focal length equal to that of the mirrors (i.e. half the

radius of curvature).

4.3 The pulse detection system

The echo pulse enters a light-tight box via a pin hole aperture to reach an EMI type 9826B photomultiplier tube (PMT). The signal from the PMT is fed into a Boxcar Averager (EG&G type 162 mainframe with two type 165 gated integrators) which is triggered by directing a small amount of pulse 2 — taken by reflection from a microscope slide cover slip, before pulse 2 enters W1 (its White cell) — on to a fast response p-i-n photodiode. The trigger signal occurs before the echo (or indeed any of the pulses) reaches the PMT. The time after the trigger pulse at which each integrator aperture is open, as well as the width of each aperture (sometimes called the gate width), can be selected so that each integrator can analyse a separate part of the PMT signal. One integrator is set on pulse 1 in order to monitor the DL14P's output, whilst the other integrator is set on the echo pulse.

A gate width of 15 ns is sufficient to isolate the individual pulses, and each integrator is set to a 10μs time constant. This results in an observed averaging time constant of 1 s. The signal is effectively averaged over a period of about five time constants, which corresponds to averaging over about 100 pulses. Further filtering and smoothing of the output signal is provided by the mainframe which is also set to a time constant of 1 s.

The information collected by the Boxcar Averager is sent via a Microlink III interface to a Hewlett-Packard HP86 microcomputer and is stored on floppy disc. Some home-produced software enables the computer to store the echo intensity, the first pulse intensity and the corresponding value of perturber gas pressure in the caesium oven. The monitoring and adjustment of perturber gas pressure is discussed more fully in the next section.

4.4 The caesium oven

The caesium oven consists of a section of thick-walled, circular stainless steel tubing (formed from solid 5 cm diameter rod) approximately 11 cm

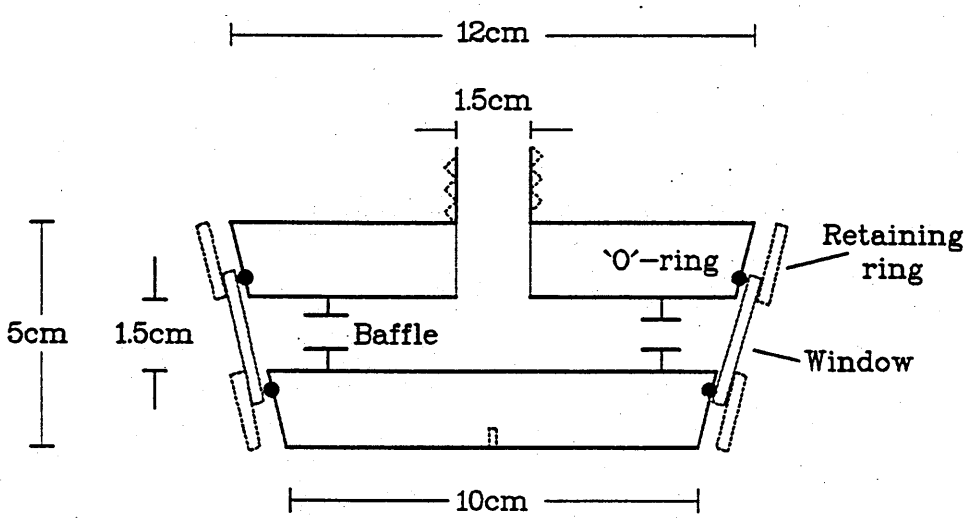

Figure 4.8 Cross-section of the caesium oven

long along its central axis. The ends are set at angles in order to minimise the effects of multiple reflections when in use (see Figure 4.8). At each end a 2.5 cm diameter strain-free silica window is held against a rubber 'O'-ring (Edwards type 1121) by a stainless steel retaining ring with a 1.5 cm aperture which is screwed in place to provide a good vacuum seal. The retaining ring has the side effect that the windows are slightly stressed, resulting in a small degree of strain depolarisation of the laser pulses as they pass through the silica. This depolarisation marginally increases the intensity of beam 3 that reaches the PMT, since a larger proportion is directed along the echo path by GF2 (see Figure 4.4). However, this is more than made up for by the increased operating life of the caesium oven, since the window seals admit less air when they are clamped.

A 1.5 cm circular aperture in the side of the caesium oven leads on to a stainless steel, threaded collar (Edwards type SC25) which is welded to the oven body and acts as the connection to the vacuum system. This allows the oven to be removed and reconnected for maintenance purposes. Stainless steel baffles placed near each end of the caesium oven serve to

contain the caesium and protect the windows to some extent by restricting the number of direct paths from the caesium surface to the oven windows. Eventually, however, sufficient caesium condenses on the windows to cause a large reduction in the magnitude of the echo pulse as seen at the PMT, in which case the windows need to be cleaned and replaced. In practice, the windows needed to be replaced after ≈30-40 hours actual experiment time, whereas the caesium in the oven needed to be replaced or topped up every 6-8 weeks (regardless of whether the experiment was running or not). The procedure adopted for changing the oven windows and refilling the oven with caesium is given in Appendix B.

The oven is uniformly heated via an electrical heating tape, which is wrapped around the oven body, with the temperature being monitored by a thermocouple placed in a small hole drilled part-way into the oven wall, midway along the oven length (see Figure 4.8). The oven temperature used throughout the echo experiments was 323 K, as this was found by Godfrey [1] to produce an echo intensity maximum. The echo intensity is subject to two competing processes: it increases with the number density (see equation 3.95), but at high number densities the caesium vapour in the oven becomes optically 'thick', absorbing the resonant light passing through it. At 323 K, the caesium vapour pressure is about 10^{-5} torr [85] (this corresponds to a number density of about 10^{17} m^{-3}), though in practice it may not be as high as this due to the physical state of the caesium in the oven.

4.5 The vacuum system

4.5.1 The purpose of the vacuum system

The vacuum system has to perform two functions: it must be able to provide a background pressure low enough that collisional degradation of the echo by collisions with contaminating gases is negligible ($\approx 10^{-8}$ torr); it must allow a perturber gas to be introduced to, or removed from, the caesium oven at a controllable rate.

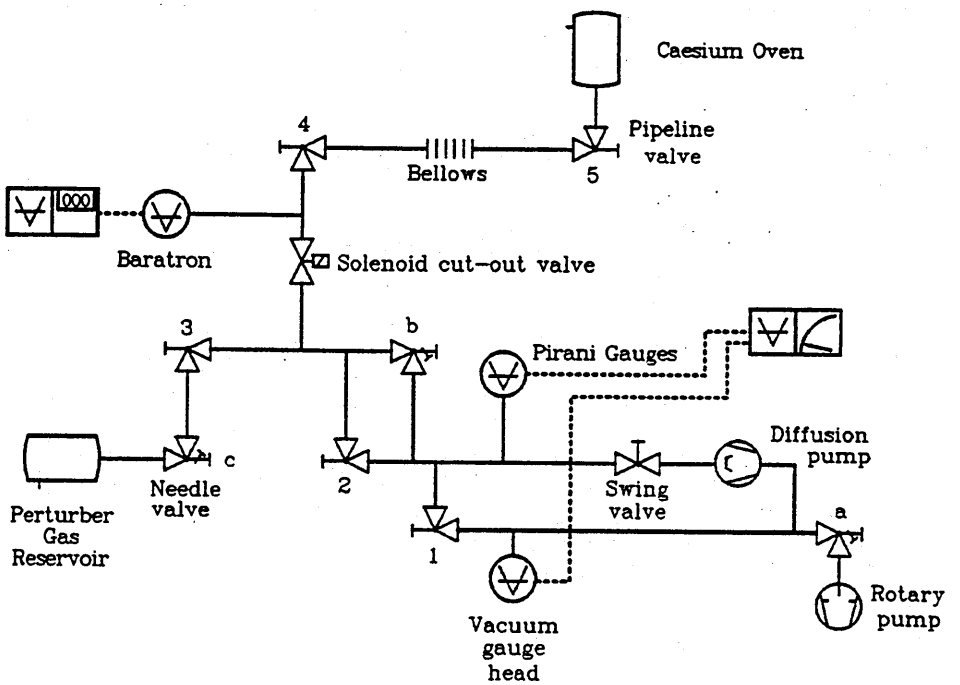

Figure 4.9 Schematic diagram of the perturber gas regulation system: needle valves are lettered, whereas pipeline valves are numbered.

4.5.2 Description of the vacuum system

Figure 4.9 is a schematic diagram of the vacuum system. In the following description of the vacuum system, the convention that the caesium oven is at the 'top' of the system and the rotary pump is at the 'bottom' has been adopted. The rotary pump (an Edwards type E1M5, located in the bottom righthand corner of Figure 4.9) is the backing pump for the system as a whole, and is therefore in operation for the entire duration of an experiment. A screw valve (Edwards 'Speedivalve', labelled 'a') serves to isolate the rotary pump from the rest of the system, and is only closed when the system is either shut down, or being restarted after a period of rest. This valve is also kept shut when the rotary pump is periodically ballasted. Closing the 'Speedivalve' not only reduces the initial volume to be evacuated by the pump, causing the pump to reach its base pressure ($\approx$0.1 mbar) slightly more quickly, but it also has the advantage that if the system above the valve

is partially evacuated, air or oil from the rotary pump cannot be drawn into it.

Above needle valve 'a' the vacuum system forks, with one arm going to a molecular diffusion pump (Edwards type E02 C). The other arm, which contains a branch to a Pirani gauge head, goes to a pipeline valve (pipeline valves are either fully open or shut, whereas needle valves can let gas pass at a user-adjustable rate). When valve 1 is shut (which is usually the case), the rotary pump backing pressure can be monitored. Above the diffusion pump is a swing valve. If the pressure in the system exceeds 0.1 mbar (the maximum pressure that the diffusion pump can handle) then the diffusion pump can be bypassed by closing the swing valve and opening valve 1, so that the pressure can be reduced by the backing rotary pump. A second Pirani gauge head located immediately above the swing valve enables the pressure of the system above the diffusion pump to be monitored. The two branches from the rotary pump then connect up before again splitting into two, with one branch containing a pipeline valve (labelled '2') and the other incorporating a needle valve (labelled 'b'), before the two arms rejoin. The reason for this arrangement is that the vacuum system above valves '2' and 'b' can be evacuated either quickly or at a controlled rate, depending on the operation being performed.

Once again, the system forks: one arm goes off towards the caesium oven, while the other goes to the perturber gas reservoir. The solenoid cut-out valve isolates the oven in the event of a power failure, which would cause the pumps to stop. As a further protection, both the solenoid valve and the diffusion pump heater are powered from a supply which is electronically shut down by a latching circuit when the power fails; even if the power is subsequently restored the circuit has to be manually re-armed before the solenoid valve re-opens — this latter feature is essential, since if the power is off for a sufficiently long period of time air will leak back into the system and would otherwise enter and contaminate the oven when the power was restored.

The Baratron manometer head is connected above the solenoid valve,

and monitors the perturber gas pressure inside the oven. This typically ranges from 10^{-8} torr to 0.3 torr, although the minimum pressure that the Baratron can measure is 10^{-4} torr. A stainless steel flexible bellows connector facilitates alignment of the oven with the excitation pulses. If the oven has to be removed for any reason, then by closing pipeline valves '4' and '5', and then disconnecting the oven (with valve '5' attached to it) only the bellows are open to the air.

4.5.3 Evacuation of the caesium oven

Evacuation of the caesium oven falls into two distinguishable cases, which are a 'cold' start and a 'warm' start. In the case of a 'cold' start, all of the equipment is initially switched off. With *all* of the valves shut, the rotary pump is switched on and is usually ballasted for about half an hour. This removes contaminants in the vacuum oil and helps the pump to attain its working backing pressure of 0.1 mbar. Once the pump has been ballasted the 'Speedivalve' is opened. With the solenoid valve disconnected, so that the valve remains shut, the latch circuit is reset, switching on the diffusion pump. The swing valve is also opened, so that while the diffusion pump is warming up, everything below valves '2' and 'b' achieves the backing pump pressure.

When the diffusion pump has warmed up, only the section between valves '1', '2', 'b' and the diffusion pump is at the diffusion pump pressure ($\approx 10^{-8}$ torr). The section below both the diffusion pump and valve '1', however, will not achieve a pressure below that of the backing pump. Parts of the vacuum system that have not yet been completely evacuated are then emptied section by section, by first closing the swing valve and opening the next valve up in the system (including the solenoid valve when that part of the system is reached). Depending on the Pirani gauge reading of the pressure above the swing valve, either the swing valve is opened, or the pressure is reduced by opening and then closing valve '1' before the swing valve is opened.

If the system is being started up from a 'warm' start then initially all the valves excepting the 'Speedivalve' are shut, both the rotary pump and

the diffusion pump are operating, and the pressure inside each section of apparatus above the swing valve has been set previously at about 2 mbar of perturber gas (this helps to reduce the amount of caesium deposited on the oven windows by reducing the mean free path). The section by section evacuation procedure for the system is identical to that used for a 'cold' start. In a normal experimental session (which can take several days) when the apparatus is unattended for periods shorter than 12 hours, the equipment is set up so that only a 'warm' start is necessary in order to continue experimental work. For any periods longer than this then both of the pumps are shut down as well and the 'Speedivalve' is closed.

Chapter 5

Preliminary experiments

This chapter describes some preliminary experiments undertaken to characterise and optimize some of the equipment. A measurement of the bandwidths of the two dye lasers is necessary in order to determine whether they can resolve the $F = 3$ and $F = 4$ hyperfine levels of the $6S_{\frac{1}{2}}$ level. The procedure employed is given in Section 5.1. Since the determination of the various collision cross sections depends upon measurement of the exponential decay rate of the echo signal with respect to perturber gas pressure, it is essential that the echo intensity lies in a region of linear PMT response; Section 5.2 shows the PMT response to varying intensities of laser radiation. Section 5.3 describes how the echo pulse is directed to the PMT, and Section 5.4 is concerned with the manner in which the pulse areas of the individual laser pulses are optimised with respect to echo intensity. In addition, outgassing tests were conducted on the caesium oven, and it was found that the oven pressure rose by about 1 mtorr over a 5 minute period (a typical experimental run time — see Chapter 6).

5.1 Estimation of the dye laser bandwidths

The bandwidth of each of the dye lasers was estimated using an air-spaced Fabry-Perot etalon. The output from the laser was first directed through a 13 mm focal length converging lens in order to produce a sufficiently diverging beam, and then directed through a Fabry-Perot etalon of plate

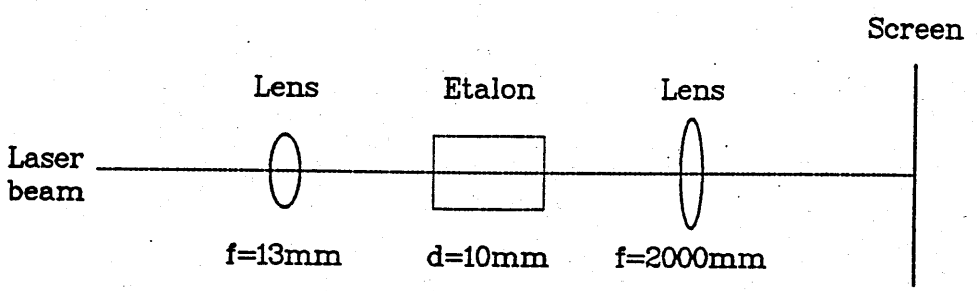

Figure 5.1 Schematic diagram of etalon/lens arrangement in order to observe interference fringes.

separation d mm, for which a number of different spacers were available. A 2 m focal length converging lens was placed as close to the exit side of the etalon as possible, with the resultant interference fringe pattern appearing on a white screen placed 2m away. Figure 5.1 shows this arrangement.

The fringe patterns for the DL14P and the GIL are shown in Figure 5.2(a) and Figure 5.2(b) respectively. The ratio of the fringe width to the fringe separation can be estimated and this, with the free spectral range (FSR) of the Fabry-Perot etalon, gives the an estimate of the value of the laser linewidth. For a plate separation of d=30 mm, the FSR ($= \frac{1}{2d}$) was 0.167 cm^{-1} (5 GHz). Clearly, the linewidths of both dye lasers were less than 5 GHz and hence the ground state hyperfine lines are resolvable. However, the excited state hyperfine structure is not resolved.

5.2 Linearity of the photomultiplier tube

The PMT employed was powered by an EMI type PM28B EHT power supply. The maximum voltage used was 1.15 kV, since higher values caused the PMT to self-trigger due to the dark current, so the PMT was fixed at this EHT value throughout the duration of the laboratory work. The smallest echo signal which could reliably be used for the experiment (due to problems

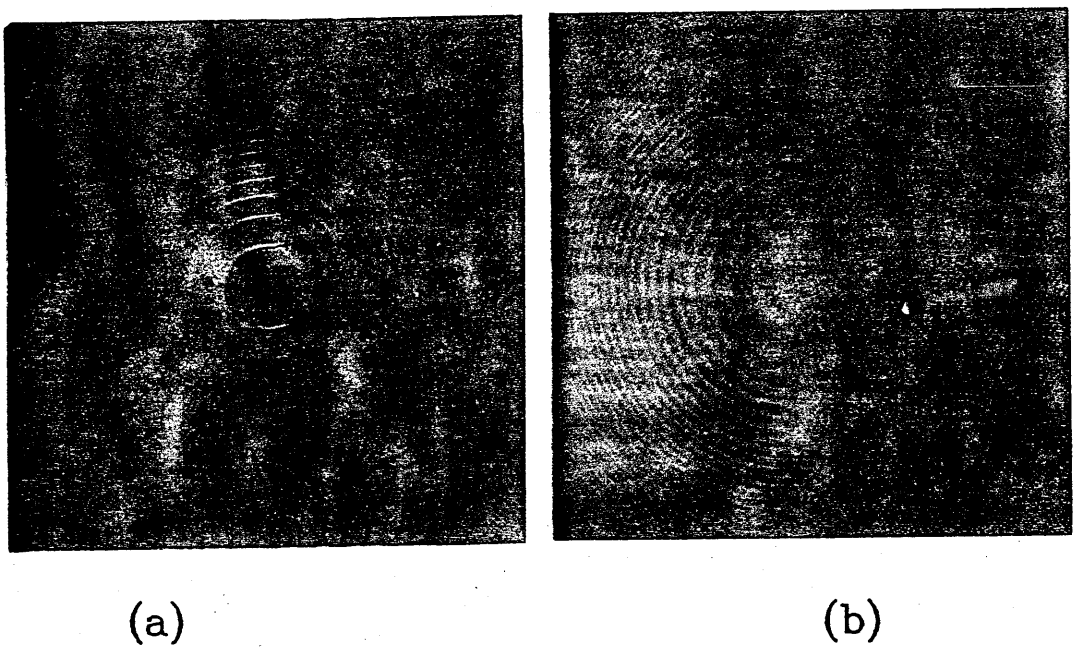

Figure 5.2 Fabry-Perot fringe patterns for (a) the DL14P, and (b) the GIL for an etalon plate separation of $d = 30$ mm.

with dark current noise) measured 2 mV on the Boxcar PMT voltage output indicator. This dictated the upper limit for the interpulse times that could be used, since the echo intensity diminishes exponentially with interpulse time, due to the excited state lifetime ($\simeq$ 150 ns).

In order to determine the linear portion of the PMT response at a gain voltage of 1.15 kV, pulse 3 from the GIL was used as a test signal, whose intensity was greatly reduced by spatial filtering and then varied through the use of neutral density filters. Figure 5.3 shows the response of the PMT as the input pulse intensity was varied. The linear response region for the PMT thus corresponds to pulse intensities which give a Boxcar-measured voltage of 0-80 mV.

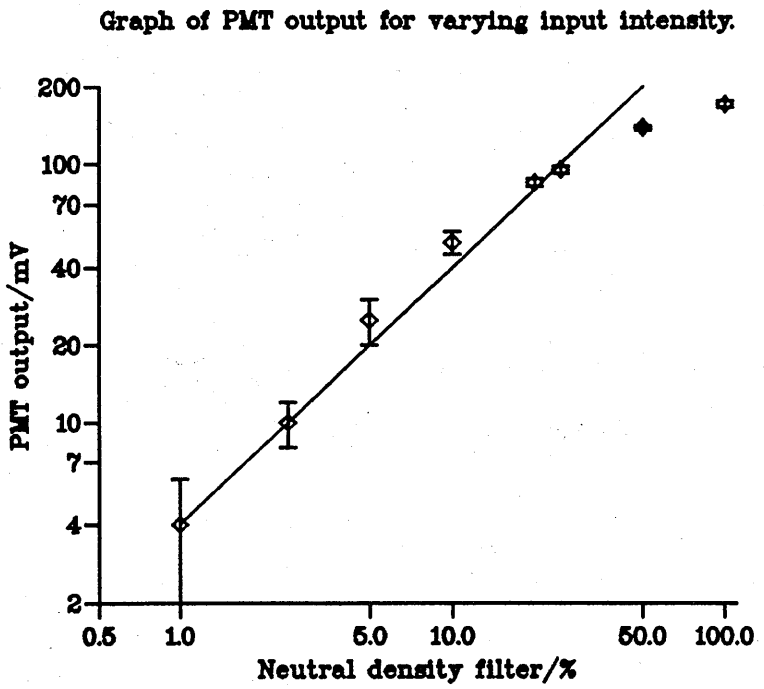

Figure 5.3 PMT response with the variation of input pulse intensity for a PMT EHT setting of 1.15 kV. The line on the graph is of gradient 1.

5.3 Directing the echo to the PMT.

The echo is considerably lower in intensity (about six or seven orders of magnitude less) than the excitation pulses when they leave the vapour sample, and this means that the echo path to the PMT cannot be followed using a piece of card as it is far too faint to be seen. However, since pulse 2 and the echo, when formed, are exactly counterpropagating (see Figure 4.4), pulse 2 can be used to 'simulate' the echo, giving a visible beam for alignment purposes. This is easily achieved by placing a mirror at the entrance side (for pulse 2) of the oven and adjusting it so that it exactly back-reflects pulse 2. A half-wave plate placed directly in front of the mirror causes the reflection of pulse 2 to have the same polarisation as well as the same propagation direction as the echo would have. On reaching GF2 it is internally reflected and is guided into the PMT via a pin-hole aperture. In order to protect the PMT from damage due to the intensity of this alignment pulse,

the EHT power supply is switched off and the PMT is blocked off. The PMT alignment can be 'fine-tuned' by reducing the intensity of this 'simulated' echo with neutral density filters and putting a small gain voltage across the PMT, and then adjusting the mirror immediately outside the PMT enclosure to give the maximum possible signal. When the backreflecting mirror and half-wave plate are subsequently removed the system should be well aligned for echo detection. The echo signal can be finally optimised by slight adjustments of the mirrors.

5.4 Optimisation of excitation pulse areas

Once the apparatus has been aligned to produce the best echo pulse as seen at the PMT, the pulse areas of the excitation pulses can themselves be optimised. From equation 3.86 the echo intensity I varies with excitation pulse area in the form

$$I \propto \sin^2\theta_1 \sin^2\theta_2 \sin^2\theta_3$$

where θ_n (n=1,2,3) are the pulse areas, which from equations 3.20 and 3.31 are given by

$$\theta_n = \frac{2p\mathcal{E}_n\tau}{\hbar}$$

This expression for pulse area is for an atom of dipole moment p subjected to Fourier transform limited square pulses. However, in the present work both laser mode structure and intensity vary from pulse to pulse and across the beam profile, and the dipole moment, p, is in fact an average of the degenerate level transitions, hence the echo intensity variation with pulse intensity will not follow this simple formula. Optimisation of the pulse intensities was therefore determined experimentally. The intensity of each excitation pulse was varied using neutral density filters whilst keeping the other two pulse intensities constant, and the size of the corresponding echo signal noted. These pulse area checks are performed prior to each set of echo experiments, and Figure 5.4 shows the results for a typical set of measurements. As one can see from the curves for beams 2 and 3, the echo

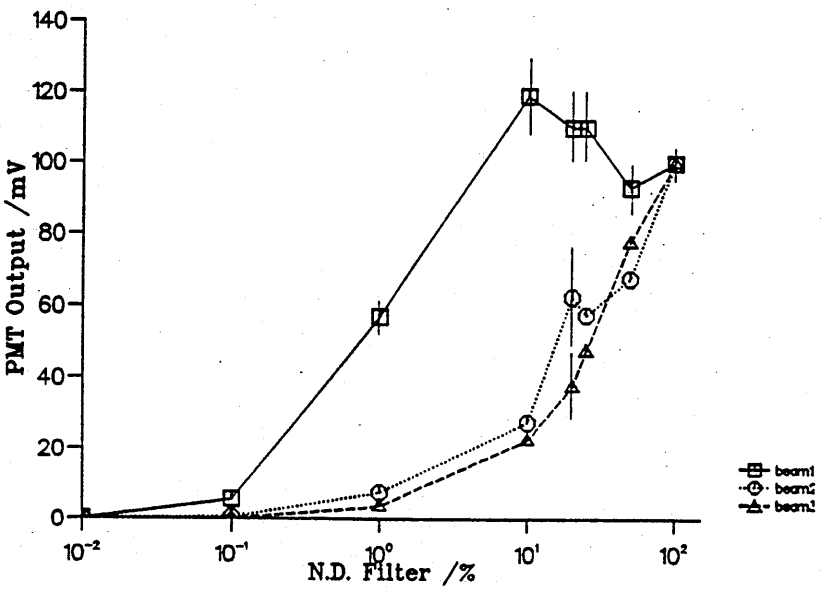

Figure 5.4 Echo intensity variation as a function of the excitation pulse intensities.

intensity increases with laser pulse intensity, indicating that the intensities of the non-attenuated beams are less than optimum. However, the curve for beam 1 shows a peak in echo intensity followed by a decrease as the pulse intensity is increased, indicating that the pulse area is greater than $\frac{\pi}{2}$ for the non-attenuated beam.

Since the output of the DL14P is partially polarised, a half-wave plate placed at the DL14P output window enables the relative proportion of energy in beams 1 and 2 to be varied by simply rotating the half-wave plate, without reducing the total energy emitted by the laser. The echo is optimised with respect to the orientation of this half-wave plate.

Chapter 6

Experimental method and presentation of results.

This chapter describes the experimental methods for three pulse echo experiments on the $6S_{\frac{1}{2}} \leftrightarrow 7P_{\frac{1}{2},\frac{3}{2}}$ second resonance transitions in caesium which are designed to measure: (i) optical coherence destroying collision cross sections; (ii) $6S_{\frac{1}{2}}$ ground state depolarising collision cross sections and associated collisional velocity changes. In the experiments described in this chapter, the term 'stimulated echo' is applied to an experiment when all three excitation pulses are tuned to the same transition ($6S_{\frac{1}{2}} \leftrightarrow 7P_{\frac{3}{2}}$ or $6S_{\frac{1}{2}} \leftrightarrow 7P_{\frac{3}{2}}$), and the term 'tri-level echo' is applied to those experiments where the first two excitation pulses are tuned to the same transition but the third excitation pulse is tuned to another transition involving a third energy level. In all cases the echo is insensitive to optical coherence destroying collisions during the interval t_{32} between the second and third pulses, and decays by collisional destruction of Zeeman coherences (depolarising collisions and associated velocity changing collisions) during this interval.

Before a series of echo experiments can be performed the equipment has to be prepared and checked, and this preparatory procedure is discussed in Section 6.1. A description of the procedure during an echo experiment is given in Section 6.2. Section 6.3 contains the theory of how the collision cross sections are obtained from the data, and Section 6.4 is concerned with the practicalities of this. The results are presented and discussed in Section 6.5.

6.1 Initial procedure

The nitrogen laser is set to a repetition rate of about 20 Hz, and when switched on is usually left running for 2-3 hours to stabilise (during which time the caesium oven is evacuated as described in Subsection 4.5.3). Both the caesium oven and bellows are heated to a steady temperature of 323 K, and when the dye lasers are tuned to their respective frequencies the optical components are adjusted to produce the photon echo (see Section 5.3). The perturber gas influx rate is set by closing valves '2' and 'b' (see Figure 4.9) and opening valve 'c', so that the steady rise in gas pressure in the oven after a period of about 2 minutes causes the echo to fall to about e^{-5} of its initial intensity. This pressure is denoted by P_{max}. The oven gas efflux rate is set by closing valve '3' and opening valve 'b', so that the oven pressure falls to about 30% of P_{max} over a period of about 3 minutes. The zero offset and gain controls on both the Microlink and the Boxcar are checked to ensure that the computer records the true Baratron pressure and the corresponding first pulse and echo intensities.

6.2 Procedure during an experimental run

At the beginning of each experimental run with no perturber gas in the oven, the echo and first pulse intensities as displayed on the Boxcar output meter are noted and the optics adjusted if necessary. The computer is set to record, immediately after which the swing valve is closed, allowing the gas to enter the oven slowly and at a controlled rate. The computer then stores the values of the intensities of the first pulse and the echo with the corresponding values of rising perturber gas pressure in the oven, until the oven gas pressure has reached P_{max}. Valves '3' and '2' are closed and the swing valve is opened, allowing the perturber gas to be slowly pumped out of the oven, and the values of the first pulse and echo intensities with their corresponding perturber gas pressure are stored. At the end of the experimental run (usually about 5 minutes for the filling and emptying cycle), the computer is reset, and valve '3' is opened to fill the oven with perturber gas

so that the zero offset on the Boxcar channel which monitors the echo signal can be checked. To begin the next run, valve '2' is opened, and the echo and first pulse intensities are again noted leaving the equipment ready for another experimental run.

If either of the echo intensity v pressure plots (there are two, since one corresponds to rising perturber gas pressure, and the other to falling pressure) are excessively noisy, the experimental run is rejected and the laser tuning, the excitation pulse paths and the echo pulse path are checked and adjusted as necessary.

Eleven experimental runs with the same interpulse times are conducted. An extra run is performed where, after the first few seconds, excitation pulse 1 is blocked for the remainder of the run. The purpose of this last experimental run is to monitor the response time of the data collection system. These 12 *experimental runs* comprise one *data set.* Figures 6.1(a) and (b) show the fluctuations of the first pulse and the decay of a stimulated echo for two experimental runs from the same data set. The perturber gas used was helium and the interpulse times were t_{21}=29.1 ns and t_{32}=129.8 ns. The upper traces show the first pulse intensity, whilst the lower traces show the echo intensity. In these two figures, the small dots correspond to rising perturber gas pressure, and the bold dots correspond to falling perturber gas pressure. Figure 6.1(c) shows the instrumental response when the first pulse has been blocked. Here the upper trace is the first pulse and lower trace is the echo: both traces give the instrumental response. Figure 6.1(d) is the average of 11 experimental runs with the same interpulse periods mentioned above. The rising and falling perturber gas pressures are denoted as before. One or other of the White cells is then adjusted to give new interpulse times, and the whole run procedure is repeated.

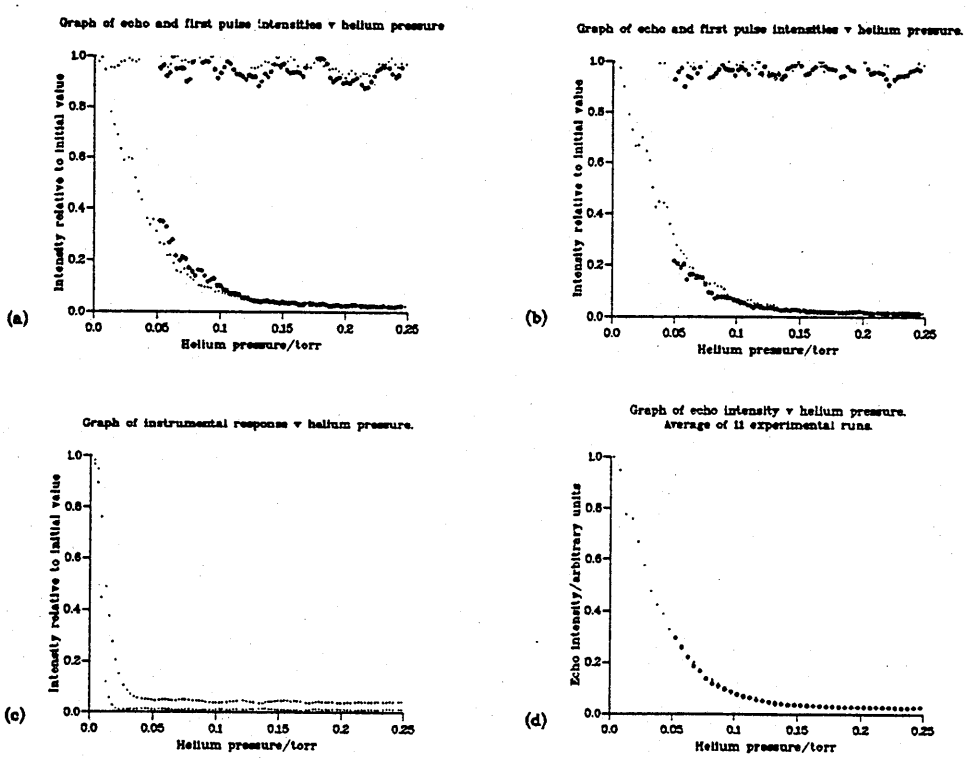

Figure 6.1 Typical data plots from the echo experiments. Figures (a) and (b) are plots for two experimental runs from the same data set. Figure (c) is the instrumental response plot for the same set, and Figure (d) is the averaged plot for the data set of 11 runs.

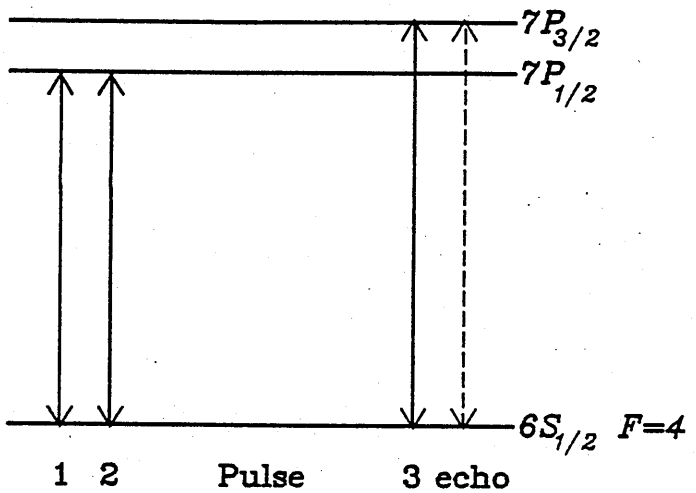

Figure 6.2 Energy level diagram for the tri-level echo experiments whose results are presented in this chapter.

6.3 Collisional cross sections from pressure induced decay

This section shows how measurements of the various collisional parameters can be obtained from the experimental data for the tri-level echo experiment shown in Figure 6.2. The first two excitation pulses (both from the DL14P) are tuned to the $6S_{\frac{1}{2}} \leftrightarrow 7P_{\frac{1}{2}}$ (459 nm) transition on the F=4 hyperfine level of the ground state — see Figure 6.2. The third excitation pulse (from the GIL) is tuned to the $6S_{\frac{1}{2}} \leftrightarrow 7P_{\frac{3}{2}}$ (455 nm) transition, again on the F=4 hyperfine level of the ground state. The tri-level echo which is produced is also on this latter transition, such that each of the three excitation pulses and the echo have a common level, i.e. the F=4 hyperfine level of the ground state.

From equation 3.95 the echo intensity varies as

$$I_{\text{echo}} \propto n^2$$

where n is the active (caesium) atom number density. However, the discussion in Section 3.8 did not take into account the effects of either spontaneous decay or collisions between the active atoms and perturber atoms:

both of these effects attenuate the echo, by destroying or reducing an atom's contribution to the echo-forming process as outlined in Chapter 1. In the experiments, the caesium vapour density ($\simeq 10^{-5}$ torr) was very much less than the perturber gas pressure ($\geq 10^{-2}$ torr), so only caesium-perturber collisions are relevant.

In the interval t_{21}, spontaneous decay of the $6S_{\frac{1}{2}} \leftrightarrow 7P_{\frac{1}{2}}$ (459 nm) transition occurs, with a rate constant denoted by Γ'_{spon}. Optical coherence destroying collisions occurring in this period can also reduce the echo intensity, and the effect of this process is represented by the rate constant Γ'_{coll}. Similarly, in the interval t_{e3} spontaneous decay of the $6S_{\frac{1}{2}} \leftrightarrow 7P_{\frac{3}{2}}$ transition contributes to echo degradation, which is denoted by the rate constant Γ''_{spon}. Optical coherence destroying collisions occurring in this interval are denoted by a rate constant Γ''_{coll}.

Optical coherence destroying collisions in the interval t_{32} do not attenuate the echo because during t_{32} the echo producing information is stored in the populations and the Zeeman coherences (see Subsection 3.9), so the echo intensity is insensitive to optical coherence destroying collisions during this interval. In this interval the echo is destroyed only by the collisional destruction of the Zeeman coherences through depolarising collisions and the collisional destruction of the modulation of these coherences in velocity space. The relaxation produced by collisions in the interval t_{32} is denoted by the rate constant Γ_{coll}.

The rate of loss of echo forming atoms in the whole period t_{e1} due to collisions is therefore given by

$$\frac{dn}{dt} = \begin{array}{ll} -\Gamma'_{coll} n & t_1 < t < t_2 \\ -\Gamma_{coll} n & t_2 < t < t_3 \\ -\Gamma''_{coll} n & t_3 < t < t_e \end{array}$$

There is also an additional exponential decay factor due to spontaneous decay, but this is independent of pressure and will not be shown. The echo intensity therefore varies as

$$I_{\text{echo}} \propto e^{-2[\Gamma'_{coll} t_{21} + \Gamma_{coll} t_{32} + \Gamma''_{coll} t_{e3}]} \qquad (6.1)$$

Velocity averaged collision cross sections for the optical coherences for the 459 nm and 455 nm transitions, denoted by $\sigma'_{\rm opt}$ and $\sigma''_{\rm opt}$ respectively, can be defined for the relaxation processes by

$$\Gamma'_{coll} = N\sigma'_{\rm opt}\bar{v}$$

and

$$\Gamma''_{coll} = N\sigma''_{\rm opt}\bar{v}$$

respectively, where N is the perturber atom number density (for this experiment $N \gg n$) and $\bar{v} = \sqrt{\frac{8k_BT}{\pi\mu}}$ is the averaged relative active atom perturber atom velocity. Here k_B is Boltzmann's constant, T the absolute temperature and μ is the reduced mass of the colliding atoms. Similarly, a velocity averaged cross section for the appropriate Zeeman coherence, $\sigma_{\rm eff}(t_{21})$, can be determined by

$$\Gamma_{coll} = N\sigma_{\rm eff}(t_{21})\bar{v}$$

$\sigma_{\rm eff}(t_{21})$ is an effective cross section and dependent on t_{21} due to the effects of velocity changing collisions. The reason for this t_{21} dependence is given later on in this section. $\sigma'_{\rm opt}$ and $\sigma''_{\rm opt}$ are also functions of t_{21} (see subsection 2.3.1), but this will not be shown since the variation over the values of t_{21} used is known to be small. However, $\sigma'_{\rm opt}$, $\sigma''_{\rm opt}$ and $\sigma_{\rm eff}(t_{21})$ are determined for a particular value of t_{21}. Substituting these expressions into equation 6.1 gives

$$I_{\rm echo} \propto e^{-2N\bar{v}[\sigma'_{\rm opt}t_{21}+\sigma_{\rm eff}(t_{21})t_{32}+\sigma''_{\rm opt}t_{e3}]} \qquad (6.2)$$

At the low perturber gas pressures used (<1 torr) the perturber gas approaches ideal gas behaviour and the perturber gas number density can be expressed

$$N = \frac{P}{k_BT}$$

where P is the perturber gas pressure. Substituting this expression for N into equation 6.2 yields

$$I_{\rm echo} \propto e^{-\frac{2\bar{v}P}{k_BT}[\sigma'_{\rm opt}t_{21}+\sigma_{\rm eff}(t_{21})t_{32}+\sigma''_{\rm opt}t_{e3}]} \qquad (6.3)$$

Equation 6.3 is more usually written

$$I_{\text{echo}} \propto e^{-\beta(t_{21},t_{32},t_{e3})P} \tag{6.4}$$

where $\beta(t_{21}, t_{32}, t_{e3})$ is the experimentally measured pressure induced decay parameter obtained from graphs of the kind discussed in Section 6.2, and can also be written as

$$\beta(t_{21}, t_{32}, t_{e3}) = \beta_{\text{opt}}(t_{21}, t_{e3}) + \beta_{Zee}(t_{21}, t_{32}) \tag{6.5}$$

where

$$\begin{aligned} \beta_{\text{opt}}(t_{21}, t_{e3}) &= \frac{2\bar{v}}{k_B T}(\sigma'_{\text{opt}} t_{21} + \sigma''_{\text{opt}} t_{e3}) \\ \beta_{Zee}(t_{21}, t_{32}) &= \frac{2\bar{v}}{k_B T}\sigma_{\text{eff}}(t_{21}) t_{32} \end{aligned} \tag{6.6}$$

The expression for $\beta_{\text{opt}}(t_{21}, t_{e3})$ can be further simplified, since according to equation 3.77

$$\begin{aligned} t_{e3} &= \tfrac{k_1}{k_3} t_{21} \\ &\approx t_{21} \end{aligned}$$

since for this experiment $\frac{k_1}{k_3} = 0.99$. Hence

$$\beta_{\text{opt}}(t_{21}, t_{e3}) \approx \frac{4\bar{v}}{k_B T}\left(\frac{\sigma'_{\text{opt}} + \sigma''_{\text{opt}}}{2}\right) t_{21} \tag{6.7}$$

Substituting equation 6.6 and equation 6.7 into equation 6.5 gives

$$\beta(t_{21}, t_{32}, t_{e3}) = \frac{4\bar{v}}{k_B T}\left[\left(\frac{(\sigma'_{\text{opt}} + \sigma''_{\text{opt}})}{2}\right) t_{21} + \frac{1}{2}\sigma_{\text{eff}}(t_{21}) t_{32}\right] \tag{6.8}$$

For the stimulated echo, the analysis is the same apart from the fact that the first and second pulses are also on the $6S_{\frac{1}{2}} \leftrightarrow 7P_{\frac{3}{2}}$ transition and so σ'_{opt} in equation 6.8 must be replaced by σ''_{opt} giving

$$\beta(t_{21}, t_{32}, t_{e3}) = \frac{4\bar{v}}{k_B T}\left[\sigma''_{\text{opt}} t_{21} + \frac{1}{2}\sigma_{\text{eff}}(t_{21}) t_{32}\right] \tag{6.9}$$

By keeping t_{21} fixed and varying t_{32}, equation 6.8 becomes the equation of a straight line, with $\frac{(\sigma'_{\text{opt}} + \sigma''_{\text{opt}})}{2}$ (for t_{21}) and $\sigma_{\text{eff}}(t_{21})$ being obtained from the intercept and the gradient respectively. This relationship was used in

a series of tri-level and stimulated echo experiments with t_{21}=29.1 ns to obtain values of $\sigma'_{\rm opt}$, $\sigma''_{\rm opt}$ and $\sigma_{\rm eff}(t_{21} = 29.1\ {\rm ns})$.

In a second series of experiments, the collisional depolarisation of the Zeeman coherences and the effects of velocity changing collisions were investigated. As was mentioned in Section 3.10, when a sample is subjected to two excitation pulses, separated by a time t_{21}, that are resonant with the same transition, the components of orientation and alignment of the two levels involved are modulated in velocity space (see for example Yodh et al [77]). The modulation period, $\rm V_m$, is given by

$$\rm V_m = \frac{\lambda}{t_{21}}$$

where λ is the wavelength of the resonant pulses. This modulation can be destroyed by excited state atoms returning to the ground state due to spontaneous decay, and for a non-degenerate ground state the modulation will nearly all have disappeared after a few excited state lifetimes. However, the $6S_{\frac{1}{2}}$ ground state has two hyperfine levels ($F = 3$ and $F = 4$) into which excited state atoms can decay, leaving a modulation of some form or other in the populations and orientation and alignment components of both ground state hyperfine levels for much longer periods. The modulation can also be destroyed by collisions. Atoms receiving velocity changing collisions, where the change in velocity is of the order of or greater than the modulation period, acquire a sufficient change in phase that they are lost from the echo. If t_{21} is small then the modulation period is large and only 'hard' velocity changing collisions will contribute to echo decay. However, as t_{21} is increased the modulation period decreases, and progressively weaker velocity changing collisions will also have an effect. A detailed discussion of the t_{21} dependence of $\sigma_{\rm eff}(t_{21})$ follows.

According to Mossberg et al [37]

$$\sigma_{\rm eff}(t_{21}) = \sigma_D + \sigma_{\rm vcc}[1 - \int_{-\infty}^{\infty} W(\Delta v_z) e^{ik\Delta v_z t_{21}} d(\Delta v_z)] \qquad (6.10)$$

where σ_D is the cross section for collisions that destroy ground state Zeeman coherences by depolarising collisions, $\sigma_{\rm vcc}$ is the cross section for collisions

that produce velocity changes in the z direction but do not depolarise, z being the direction of propagation of the first and second excitation pulses. $W(\Delta v_z)$ is a normalised scattering kernel, assumed symmetric about $\Delta v_z = 0$, which gives the probability that a non-depolarising collision will change the atom's z-component of velocity by an amount Δv_z. Now $\sigma_{\rm eff}(t_{21})$ has simple limits. When $t_{21} \rightarrow 0$, the integral of equation 6.10 equals unity and so

$$\sigma_{\rm eff}(t_{21} \rightarrow 0) = \sigma_D$$

In this region the velocity modulation period, V_m, is near-infinite and thus velocity changing collisions have no effect. When $t_{21} \rightarrow \infty$ the integral of equation 6.10 vanishes and so

$$\sigma_{\rm eff}(t_{21} \rightarrow \infty) = \sigma_D + \sigma_{\rm vcc}$$

This corresponds to the situation where V_m is so small that any change in velocity is sufficient to remove the atom from the echo signal.

For arbitrary t_{21} the exponential term in the equation 6.10 must be expanded in a Taylor series to yield

$$e^{ik\Delta v_z t_{21}} = 1 + ik\Delta v_z t_{21} - \frac{k^2 \Delta v_z^2 t_{21}^2}{2} + ...$$

Substituting this expansion into equation 6.10 and integrating has the result that the first non-vanishing term in the integral contains the second order term. Hence for small $k\Delta v_z t_{21}$,

$$\begin{aligned} \sigma_{\rm eff}(t_{21}) &\propto \sigma_D + \sigma_{\rm vcc} \int_{-\infty}^{\infty} W(\Delta v_z) \frac{k^2 \Delta v_z^2 t_{21}^2}{2} d(\Delta v_z) \\ &\propto \sigma_D + \sigma_{\rm vcc} \overline{\Delta v_z^2} \frac{k^2 t_{21}^2}{2} \end{aligned} \tag{6.11}$$

In the experiments performed for this thesis t_{21} was typically 30 ns, and with $k \approx 2\pi/500 \times 10^{-9}$ m^{-1} and with typical values of $|\Delta v_z| \simeq 1$ ms^{-1} [24] [61] [86] the product $k\Delta v_z t_{21} = 0.5$. Clearly, the variation of $\sigma_{\rm eff}(t_{21})$ with t_{21}^2 will enable σ_D to be determined from the intercept of a straight-line graph, with the gradient of such a graph giving an estimate of the product $\sigma_{\rm vcc}\overline{\Delta v_z^2}$. The second series of experiments performed in this thesis are

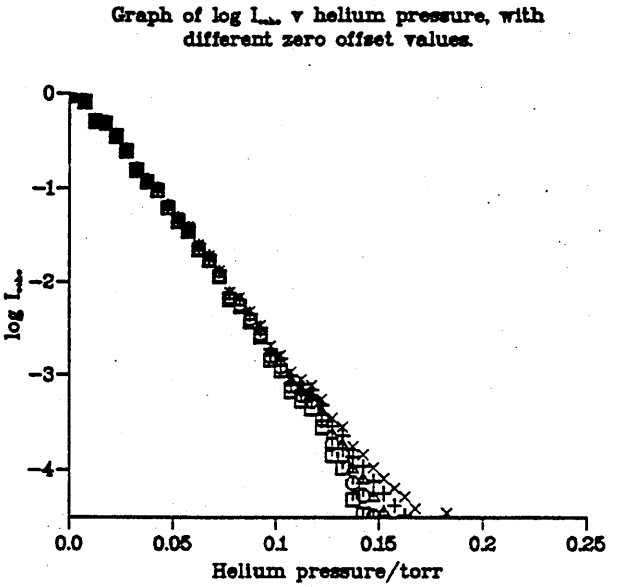

Figure 6.3 Logarithmic plot of the averaged data set shown in Figure 6.1(d), with five different values of zero offset correction factor.

concerned with this relationship, and both tri-level and stimulated echoes were used. In this series of experiments, t_{21} was varied over the range 18.9 – 69.9 ns, and the experimentally measured values of β, together with the known values of $\sigma'_{\rm opt}$ and $\sigma''_{\rm opt}$ were used to obtain values of $\sigma_{\rm eff}(t_{21})$. $\sigma_{\rm eff}(t_{21})$ was then plotted against t_{21}^2 to obtain σ_D and $\sigma_{\rm vcc}\overline{\Delta v_z^2}$ from the intercept and gradient respectively.

6.4 Data processing

Figure 6.3 shows a logarithmic graph of the data shown in Figure 6.1(d), which according to equation 6.4 should be a straight line. The first few points show the effects of the finite instrumental response time. These points are rejected in the data processing. Inspection of Figure 6.1(d) reveals that the recorded echo intensity shown does not decay to zero as the perturber pressure is increased, but levels off instead just above the x-axis. The reason for this is that it is difficult to set all the instruments perfectly to zero. This

zero offset causes the logarithmic plot to deviate from a straight line, with the deviation becoming more pronounced as I_{echo} decreases. The solution is to correct for this zero offset by subtracting the offset value from the data before the logarithm is taken, though this is harder to do than at first it seems, for random fluctuations and drifts in the echo intensity caused, for example, by pulse-to-pulse variations of the excitation pulse areas make it hard to determine the true magnitude of the offset. Figure 6.3 shows logarithmic plots of the data show in Figure 6.1(d) with five different values of offset correction term. The task of fitting the best line to the data is made easier by the multiple plot, and the gradient of the best straight line gives the value of the decay constant, $\beta(t_{21}, t_{32}, t_{e3})$, which from now on will be abbrieviated to β. In all of the experiments, the error in measuring β is of the order of 5% or less.

6.5 Experimental results

Tri-level echo experiments (Figure 6.2) and stimulated echo experiments (Figure 6.7) were performed for various values of the interpulse times. The tri-level experiment of Figure 1.23(b) was attempted but eventually abandoned after much effort since the echo amplitudes were too small and noisy to work with. Two series of experiments were conducted. The first series of experiments was designed to measure the collisional destruction of optical coherences. The second series was designed to measure the collisional destruction of Zeeman coherences. The results of these two series of experiments are presented in Subsections 6.5.1- 6.5.4.

There was no evidence for non-exponential decay (other than effects described in Section 6.4) in any of the experimental runs taken. It is therefore assumed that only a single collisionally induced exponential decay is present in any experiment so that equation 6.8 (or 6.9) and equation 6.11 apply.

6.5.1 The experimental results for measurements of optical coherence destroying collisions using tri-level and stimulated echoes

The excitation pulse sequence and the transitions involved in the tri-level echo experiments are shown in Figure 6.2. In the first set of tri-level echo experiments, (i.e. the β v t_{32} experiments), t_{21} was fixed at 29.1 ns, and t_{32} was taken at various values up to about 190 ns. Graphs of the pressure induced decay parameter β v t_{32} with helium, argon and xenon perturbers are shown in Figures 6.4- 6.6 respectively. The estimated error in measuring β is typically less than 5%, so only one typical error bar has been shown on each graph. On each of these graphs an equivalent value of β for the two pulse echo experiments conducted by Durrant et al [61] (calculated by substituting their σ'_{opt} and σ''_{opt} measurements into either equation 6.7 or equation 6.8 to obtain a value for β) is shown for comparison — this extra point is denoted by a triangle in Figures 6.4- 6.10. The values of the intercepts of Figures 6.4- 6.6 are presented in Subsection 6.5.2.

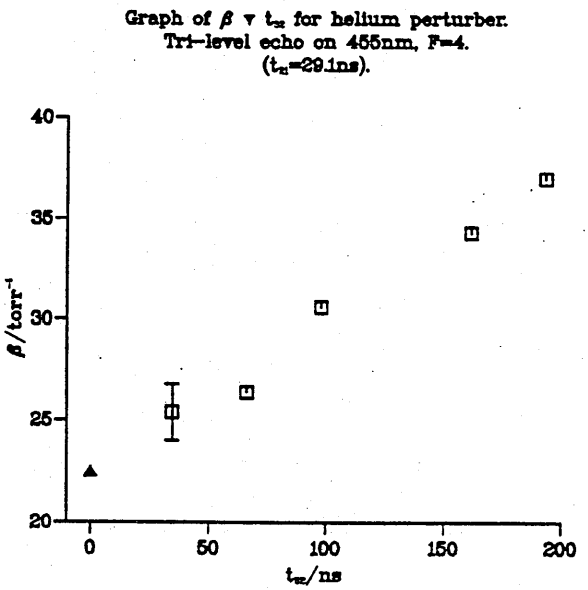

Figure 6.4 Graph of β v t_{32} for helium perturber - t_{21} was fixed at 29.1 ns. The point marked with a triangle has been calculated from the results of Durrant et al [61].

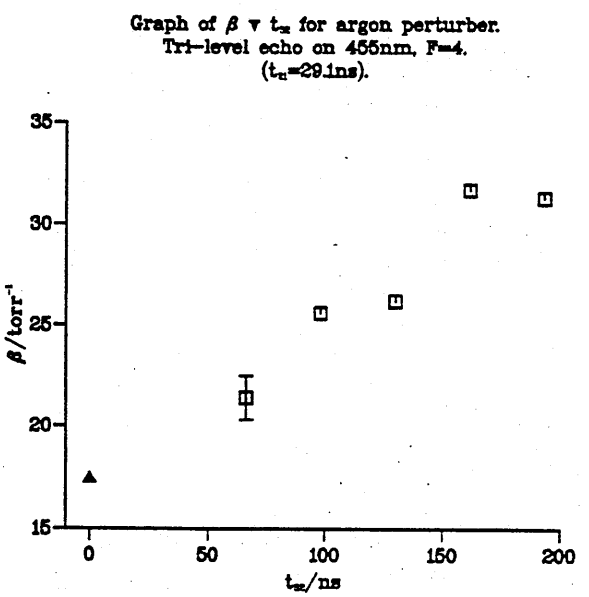

Figure 6.5 Graph of β v t_{32} for argon perturber - t_{21} was fixed at 29.1 ns. The point marked with a triangle has been calculated from the results of Durrant et al [61].

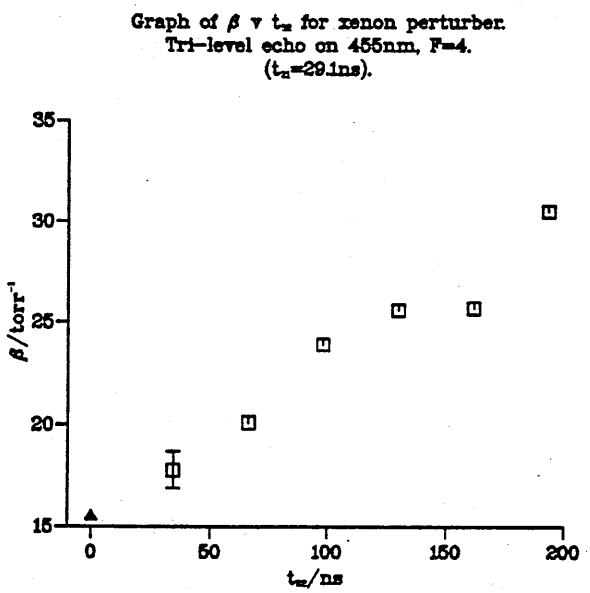

Figure 6.6 Graph of β v t_{32} for xenon perturber - t_{21} was fixed at 29.1 ns. The point marked with a triangle has been calculated from the results of Durrant et al [61].

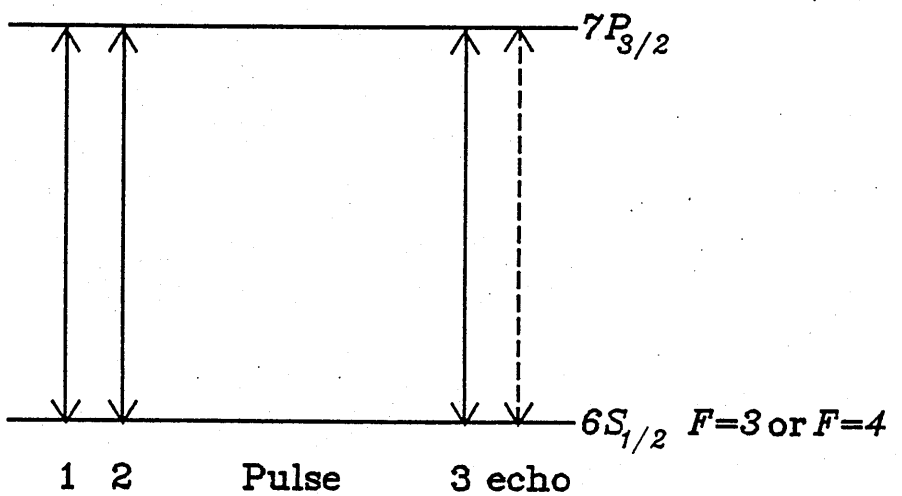

Figure 6.7 Energy level diagram for the stimulated echo experiments whose results are presented in this section.

The excitation pulse sequence employed for the stimulated echo experiments is shown in Figure 6.7. Once again, t_{21} was fixed at 29.1 ns, and t_{32} was varied as before. Graphs of the β v t_{32} results for the stimulated echo experiments involving helium, argon and xenon perturbers are shown in Figures 6.8- 6.10 respectively. The values of the intercepts of Figures 6.8- 6.10 are presented in Subsection 6.5.2.

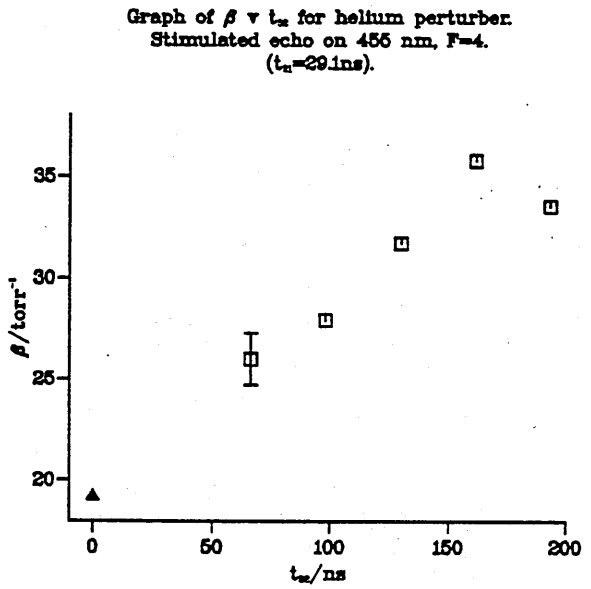

Figure 6.8 Graph of β v t_{32} for helium perturber - t_{21} was fixed at 29.1 ns. The point marked with a triangle has been calculated from the results of Durrant et al [61].

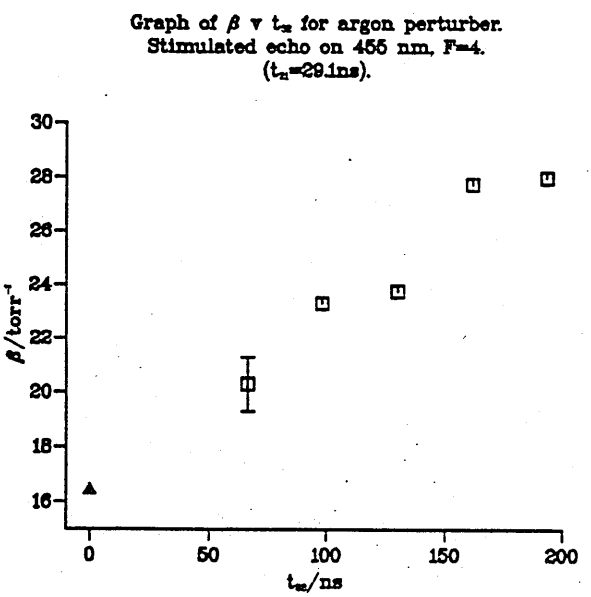

Figure 6.9 Graph of β v t_{32} for argon perturber - t_{21} was fixed at 29.1 ns. The point marked with a triangle has been calculated from the results of Durrant et al [61].

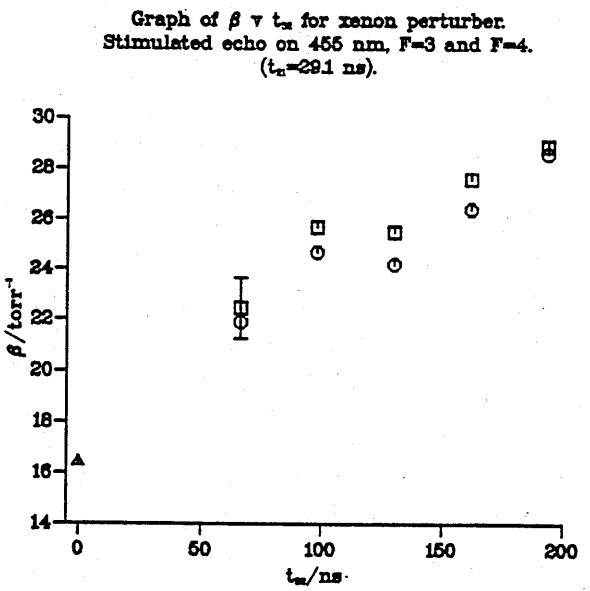

Figure 6.10 Graph of β v t_{32} for xenon perturber - t_{21} was fixed at 29.1 ns. The squares denote an echo formed on the $F = 3$ hyperfine ground state, and the octagons denote an echo formed on the $F = 4$ hyperfine ground state. The point marked with a triangle has been calculated from the results of Durrant et al [61].

6.5.2 Presentation of the optical coherence destroying collision cross section measurements

The intercept obtained from Figures 6.4- 6.6 enables the average of the collision cross sections for optical coherence destroying collisions, $(\sigma'_{opt} + \sigma''_{opt})/2$, to be determined, where σ'_{opt} is the cross section for the $6S_{\frac{1}{2}} \leftrightarrow 7P_{\frac{1}{2}}$ transition and σ''_{opt} is the cross section for the $6S_{\frac{1}{2}} \leftrightarrow 7P_{\frac{3}{2}}$ transition. The intercepts obtained from Figures 6.8- 6.10 give the cross section for optical coherence destroying collisions, σ''_{opt}, only. Note that all of these cross section measurements have been determined for $t_{21} = 29.1$ ns. The intercepts have been obtained from least squares fits of the data, and the error values quoted are the standard errors calculated from the deviations of β for each of the least squares fits. These measurements are presented in Table 6.1. The corresponding results obtained by Durrant et al [61] in their two pulse echo experiments using caesium are also shown for comparison.

Echo type	Perturber gas atom	$(\sigma'_{opt} + \sigma''_{opt})/2$ (Å^2)	
		This work	Durrant et al [61]
	Helium	488 ± 17	485 ± 8
Tri-level	Argon	1020 ± 96	1060 ± 11
	Xenon	1392 ± 110	1382 ± 20
		σ''_{opt} (Å^2)	
	Helium	471 ± 44	415 ± 7
Stimulated	Argon	1009 ± 60	997 ± 9
	Xenon	1738 ± 140	1328 ± 6
	Xenon*	1478 ± 131	1328 ± 6

Table 6.1 Table of the average cross section, $(\sigma'_{opt} + \sigma''_{opt})/2$, for optical coherence destroying collisions measured by tri-level echoes, and the cross section σ'' for optical coherence destroying collisions measured by stimulated echoes.

With the exception of the stimulated echo result using xenon as a perturber, the two sets of results are in very good agreement. The asterisked figure for xenon has been obtained by including the value of β calculated from the data of Durrant et al [61] (marked with a triangle on Figure 6.10) when calculating the least squares fit.

Since the tri-level echo experiments yield an average collision cross section value, substitution of the σ''_{opt} measurements from the stimulated echo experiments enables σ'_{opt} to be determined from the tri-level echo experiment results. The optical coherence destroying collision cross section results are presented in Table 6.2.

Transition	Perturber gas atom	σ''_{opt} (Å^2)	σ''_{opt}‡ (Å^2)	σ''_{opt}† (Å^2)
	Helium	471 ± 44	415 ± 7	434 ± 26
455 nm	Argon	1009 ± 60	997 ± 9	1027 ± 80
$6S_{\frac{1}{2}} \leftrightarrow 7P_{\frac{3}{2}}$	Xenon	1738 ± 140	1328 ± 6	1438 ± 110
	Xenon*	1478 ± 131	1328 ± 6	1438 ± 110
		σ'_{opt} (Å^2)	σ'_{opt}‡ (Å^2)	σ'_{opt}† (Å^2)
459 nm	Helium	505 ± 44	556 ± 2	532 ± 29
$6S_{\frac{1}{2}} \leftrightarrow 7P_{\frac{1}{2}}$	Argon	1031 ± 75	1123 ± 6	1110 ± 76
	Xenon	1306 ± 131	1436 ± 19	1450 ± 93

Table 6.2 Table of cross section measurements for optical coherence destroying collisions.

The results marked with a dagger and a double dagger are those obtained by Durrant and Manners [59] and Durrant et al [61] respectively, with the latter set of results adjusted to 323 K. As can be seen from Table 6.2, with the exception of the 455 nm ($6S_{\frac{1}{2}} \leftrightarrow 7P_{\frac{3}{2}}$) stimulated echo result for xenon, the optical coherence cross sections obtained from these experiments are in good agreement with those derived by Durrant et al [59] [61] from their two pulse echo experiments. The asterisked figure for xenon (455 nm) has been obtained by including the value of β calculated from the data of Durrant et al [61] (marked with a triangle on Figure 6.10) when calculating the least squares fit. The 459 nm value for xenon has been obtained using the asterisked 455 nm result. The averaged cross section value for xenon, obtained from the tri-level echo experiments, is in much better agreement with Durrant et al's results than the single cross section measurement obtained from the stimulated echo experiments.

The agreement for the helium and argon measurements is very satisfactory, as is the average measurement obtained for the tri-level echo exper-

iment using xenon. The discrepancy for the stimulated echo xenon measurement remains however, but it is interesting to note that the results for echoes formed from the F=3 and F=4 hyperfine levels of the ground state (see Figure 6.10) are similar.

6.5.3 The experimental results for tri-level and stimulated echo measurements of the cross sections for depolarising collisions and velocity changing collisions

From equations 6.8 and 6.9, the gradients of each of the graphs in Figures 6.4- 6.10 yield values for $\sigma_{\text{eff}}(t_{21})$ for $t_{21} = 29.1$ ns. Measurements of $\sigma_{\text{eff}}(t_{21})$ for other values of t_{21} were obtained in a different manner for the following reason. Because of the arrangement of the components on the optical bench, altering t_{21} changes the value of t_{32} such that as t_{21} is increased t_{32} is reduced. Thus, for these new values of t_{21} (and hence t_{32}), obtained by adjusting White cell 1 (see Figure 4.4), $\sigma_{\text{eff}}(t_{21})$ has been calculated by re-arranging equation 6.8 to give

$$\sigma_{\text{eff}}(t_{21}) = \frac{2}{t_{32}}[\beta - \frac{4\bar{v}}{k_B T}(\frac{(\sigma'_{\text{opt}} + \sigma''_{\text{opt}})}{2})t_{21}] \qquad (6.12)$$

for tri-level echoes, and a similar equation obtained from equation 6.9 above for stimulated echoes. Values of $\sigma_{\text{eff}}(t_{21})$ have been calculated by substituting into the above the relevant values of β (obtained as described above), t_{21} and t_{32}, along with the respective values for σ'_{opt} and σ''_{opt} obtained from the β v t_{32} experiments. A dozen echo intensity v perturber gas pressure runs were performed for each value of t_{21}. Note that equation 6.12 has t_{32} as a denominator, and this coupled with the fact that $\sigma_{\text{eff}}(t_{21})$ is obtained from subtracting two similarly sized quantities has the result that as t_{32} is reduced, the error increases from typically 12%, for $t_{21} = 18.9$ ns, to double this value for $t_{21} = 69.9$ ns.

The results for the tri-level echo experiments to measure the variation of $\sigma_{\text{eff}}(t_{21})$ for the $6S_{\frac{1}{2}}$ (F=4) ground state with t_{21}^2 are shown in Figures 6.11-6.13. The values obtained from the intercepts and gradients of Figures 6.11-6.13 are presented in Subsection 6.5.4.

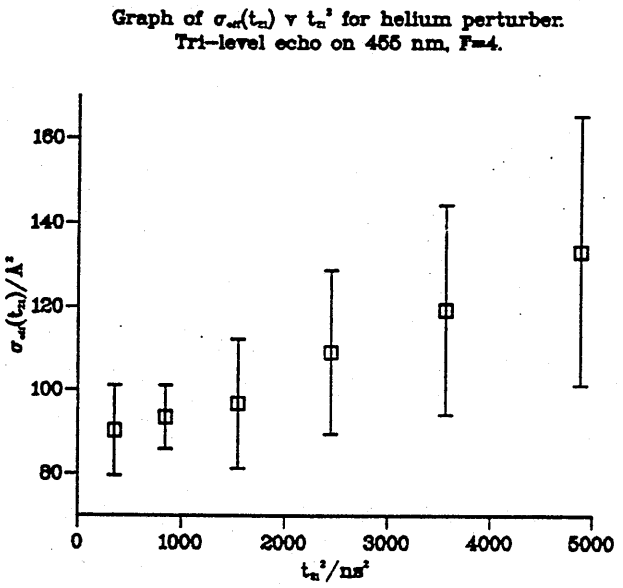

Figure 6.11 Graph of $\sigma_{\text{eff}}(t_{21})$ v t_{21}^2 for helium perturber.

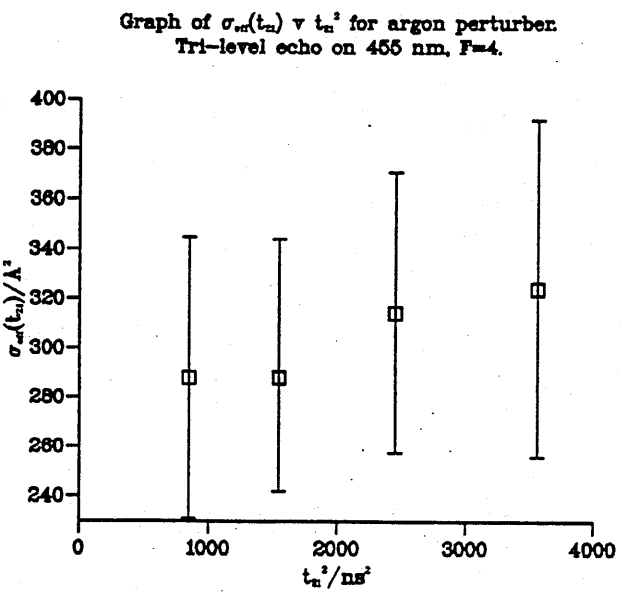

Figure 6.12 Graph of $\sigma_{\text{eff}}(t_{21})$ v t_{21}^2 for argon perturber.

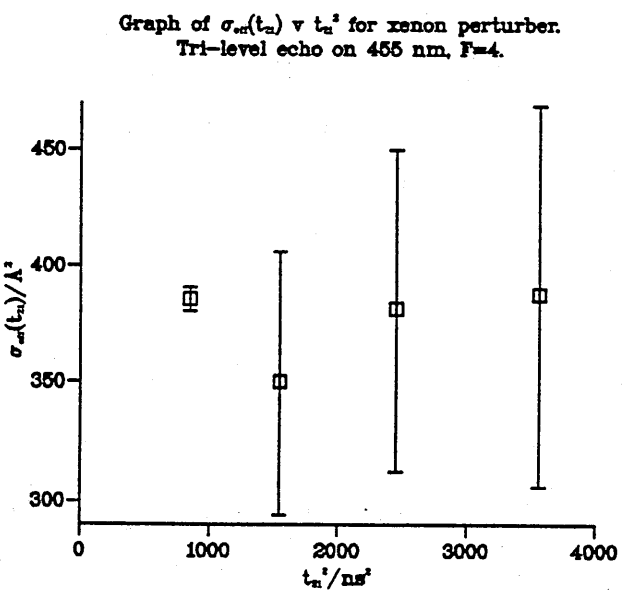

Figure 6.13 Graph of $\sigma_{\text{eff}}(t_{21})$ v t_{21}^2 for xenon perturber.

The results for the stimulated echo experiments for the variation of $\sigma_{\text{eff}}(t_{21})$ with t_{21}^2 are shown in Figures 6.14- 6.16. The values obtained from the intercepts and gradients of Figures 6.14- 6.16 are presented in Subsection 6.5.4.

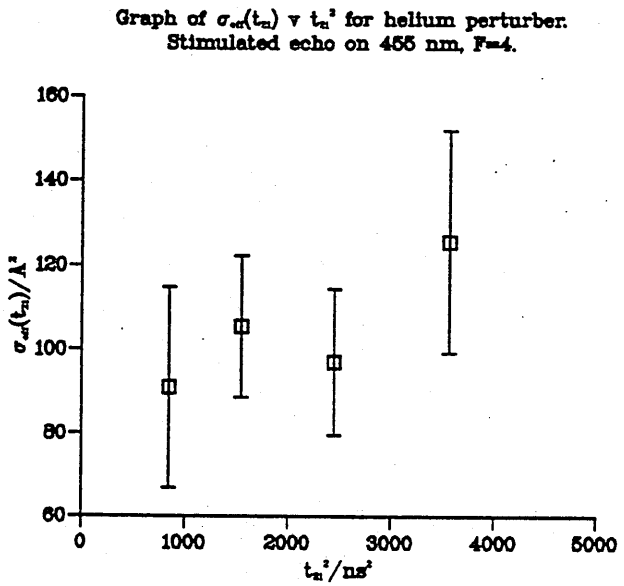

Figure 6.14 Graph of $\sigma_{\text{eff}}(t_{21})$ v t_{21}^2 for helium perturber.

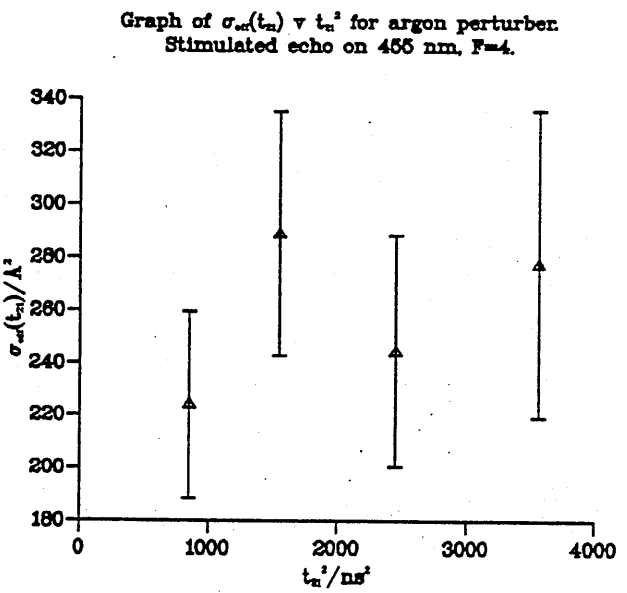

Figure 6.15 Graph of $\sigma_{\text{eff}}(t_{21})$ v t_{21}^2 for argon perturber.

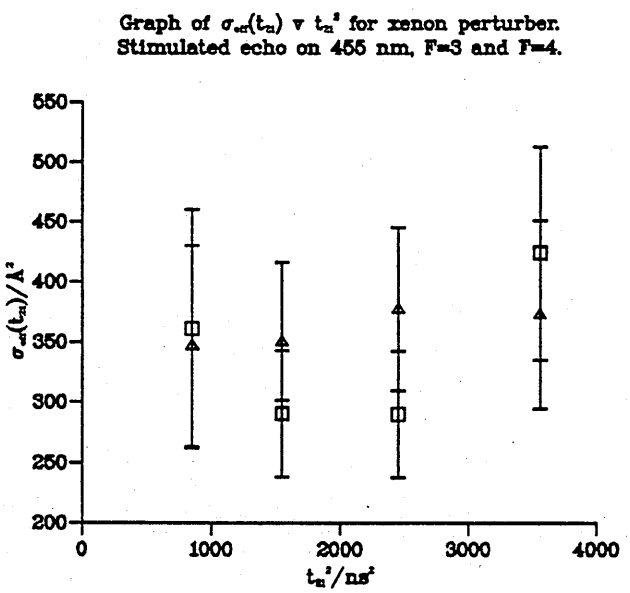

Figure 6.16 Graph of $\sigma_{\text{eff}}(t_{21})$ v t_{21}^2 for xenon perturber.

6.5.4 Presentation of the tri-level and stimulated echo cross section measurements for depolarising collisions and velocity changing collisions

It can be seen from equation 6.11 that the intercept of Figures 6.11- 6.16 gives σ_D, the depolarising collision cross section, whilst the gradient gives the product $\sigma_{vcc}\overline{\Delta v_z^2}$. The intercepts and gradients obtained from the least squares best fit lines for Figures 6.11- 6.16 are given in Table 6.3. The error values quoted are the standard errors for the deviations in $\sigma_{eff}(t_{21})$ and $\sigma_{vcc}\overline{\Delta v_z^2}$ (the gradient) of the least squares best fit lines. The measurements of the depolarising collision cross sections, σ_D, for the stimulated echo and tri-level echo experiments are in good agreement, and this, coupled with the fact that the stimulated echo decay graphs do not exhibit multi-exponential decay, would tend to support the assertion made in Section 1.5 that the depolarising cross sections determined from the stimulated echo experiments relate predominantly to ground state atoms.

With, perhaps, the exception of the results obtained from helium, no confidence can be placed in the estimates of the product $\sigma_{vcc}\overline{\Delta v_z^2}$ derived from the gradients, and for this reason these values are shown in parentheses.

Figures 6.17- 6.19 are combined plots of the stimulated and tri-level echo results.

Echo type	Perturber gas atom	σ_D (Å^2)	$\sigma_{vcc}\Delta v_z^2$ (Å^{2}m^{2}s^{-2})
	Helium	85 ± 2	53 ± 5
Tri-level	Argon	272 ± 7	(79 ± 16)
	Xenon	366 ± 20	(26 ± 53)
	Helium	82 ± 10	59 ± 27
Stimulated	Argon	234 ± 32	(63 ± 84)
	Xenon [F=3]	288 ± 70	(137 ± 180)
	Xenon [F=4]	343 ± 9	(53 ± 21)

Table 6.3 Table of tri-level and stimulated echo measurements of the depolarising collision cross section, σ_D, and the product $\sigma_{vcc}\overline{\Delta v_z^2}$.

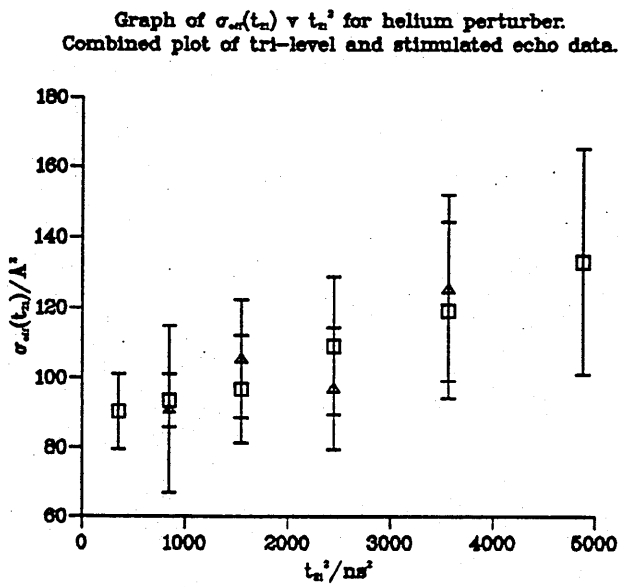

Figure 6.17 Combined graph of the stimulated and tri-level echo experiments for the variation of $\sigma_{\text{eff}}(t_{21})$ with t_{21}^2 for helium perturber.

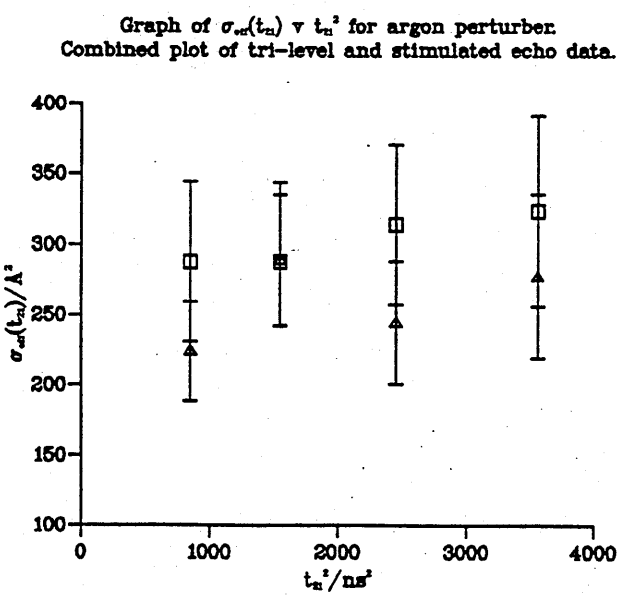

Figure 6.18 Combined graph of the stimulated and tri-level echo experiments for the variation of $\sigma_{\text{eff}}(t_{21})$ with t_{21}^2 for argon perturber.

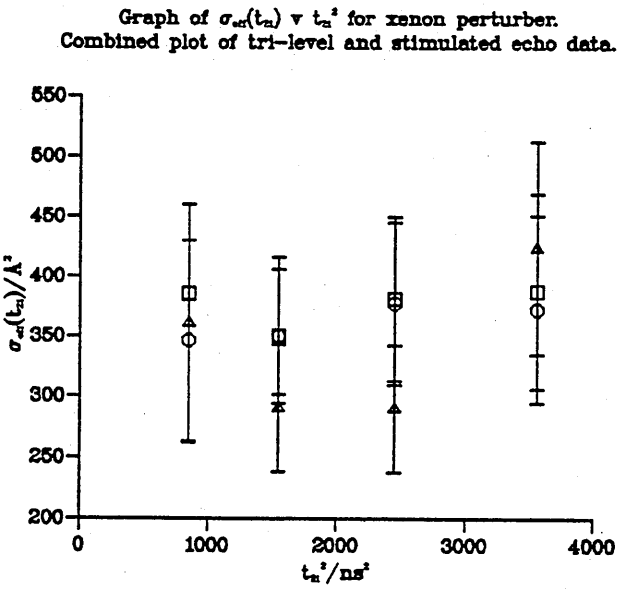

Figure 6.19 Combined graph of the stimulated and tri-level echo experiments for the variation of $\sigma_{\text{eff}}(t_{21})$ with t_{21}^2 for xenon perturber.

In Figures 6.17- 6.19, there is considerable overlap of the error bars. The measurements of σ_D and $\sigma_{vcc}\overline{\Delta v_z^2}$ obtained from Figure 6.17- 6.19 are given in the first two columns of Table 6.4.

Perturber gas atom	σ_D (Å^2)	$\sigma_{vcc}\overline{\Delta v_z^2}$ (Å^{2}m^{2}s^{-2})	$\sigma_D\dagger$ (Å^2)	$\sigma_D\ddagger$ (Å^2)
Helium	84 ± 5	53 ± 5	108 ± 16	61
Argon	253 ± 32	(68 ± 58)	225 ± 35	212
Xenon	332 ± 37	(74 ± 58)	398 ± 60	356

Table 6.4 Table of combined tri-level and stimulated echo measurements of the depolarising collision cross section, σ_D, and the product $\sigma_{vcc}\overline{\Delta v_z^2}$.

The measurements of the product $\sigma_{vcc}\overline{\Delta v_z^2}$ for argon and xenon are in parentheses as no real confidence can be placed in them. The results marked with the single and double-daggers are measurements of linear depolarising cross sections of excited state ($6P_{\frac{3}{2}}$) caesium atoms, obtained in resonance fluorescence experiments by Guiry and Krause [88] and theoretical calculations for the $6P_{\frac{3}{2}}$ level by Rebane and Rebane [89] respectively, and are included here for comparison.

6.6 Conclusion

The values obtained here for the optical coherence cross sections for the $6S_{\frac{1}{2}} \leftrightarrow 7P_{\frac{1}{2},\frac{3}{2}}$ caesium transitions are, apart from the anomalous stimulated echo results for xenon, in good agreement with previous measurements using two pulse echoes [59] [61]. Further stimulated echo work using xenon may reveal a cause for this anomaly. The results confirm the discrepancies discussed in [59] between cross sections obtained by echo measurements and by pressure broadening studies. Further stimulated echo work using xenon may reveal the cause of the discrepancy.

The results obtained for the depolarising cross section of the caesium $6S_{\frac{1}{2}}$ ground state, σ_D, mark the first measurement of this parameter for ground state caesium atoms. The measurements of σ_D obtained from the tri-level and stimulated echo experiments are in good agreement, which would tend to

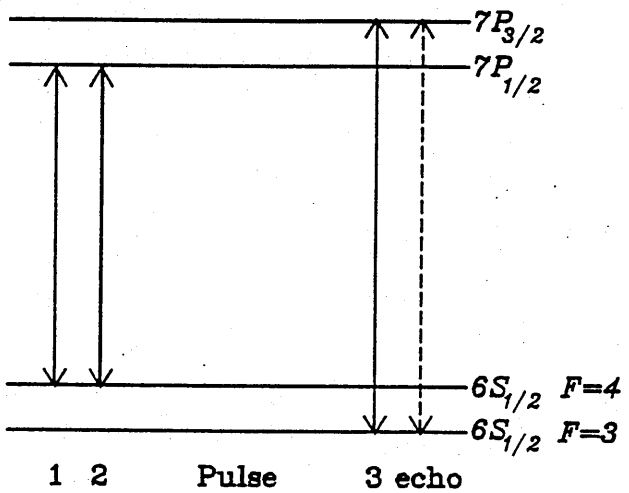

Figure 6.20 Proposed excitation pulse sequence to investigate the effect of spontaneous decay in the interval t_{32}.

support the comments made in Section 1.5 about the excited state echo being too small to make a significant contribution to the stimulated echo cross section measurements. Interestingly, the values obtained for σ_D are very similar to resonance fluorescence measurements performed by Guiry and Krause [88] into depolarising collision cross sections for linear polarisation of the excited state $6P_{\frac{3}{2}}$ caesium atoms perturbed by noble gases at a buffer pressure of 0-10 torr.

Further experimental work in this area would include tri-level echo experiments using sub-nanosecond duration excitation pulses to measure the depolarising collision cross sections for $7P_{\frac{1}{2}}$ and $7P_{\frac{3}{2}}$ excited state caesium atoms. Sub-nanosecond excitation pulses would mean that the excitation pulse separation could be greatly reduced without the echo signal being swamped at the photomultiplier tube by the other excitation pulses, especially the third excitation pulse. Shorter duration pulses would allow further investigation of $\sigma_{\text{eff}}(t_{21})$ for shorter intervals of t_{21} than was possible here, resulting in smaller errors in the value of $\sigma_{\text{eff}}(t_{21})$ calculated from the appropriate measurement of β and a more accurate measurement of σ_D.

Another possible area of study would be using tri-level echo experiments

to investigate the transfer of modulation by spontaneous decay during the interval t_{32}. Figure 6.20 shows the proposed excitation pulse sequence. Immediately after the first two excitation pulses have been applied, velocity modulations exist in the $F = 4$ ground state and the excited state. Subsequent spontaneous decay would cause an excited state atom to decay into either of the hyperfine levels of the ground state, with the result that modulations of some form will exist in both of the ground state levels even after a few lifetimes. The third excitation pulse would therefore provide a means of measuring the rate of decay by forming an echo on a different transition to that of the first two excitation pulses.

Appendix A: The excited-state tri-level echo and the stimulated echo

The excited-state tri-level echo depicted in Figure 3.2(ii) shares the same 3×3 M matrices for the first two pulses as the ground-state tri-level echo. For the third pulse however, ω_3, the frequency of the third pulse, couples levels $|b>$ and $|c>$ only, and with $\zeta = -p_{bc}\mathcal{E}_3 e^{i\vec{k}_3 \cdot \vec{r}_3}$, the rotating frame Hamiltonian is

$$\mathrm{H}_\omega = \begin{pmatrix} 1 & 0 & 0 \\ 0 & 0 & \zeta^* \\ 0 & \zeta & 0 \end{pmatrix}$$

By comparison with equations 3.19 and 3.34, the time evolution operator matrix for the third pulse is

$$\mathrm{M}_{3b\leftrightarrow c>} = \begin{pmatrix} 1 & 0 & 0 \\ 0 & \cos\frac{\theta_3}{2} & -i\frac{\zeta^*}{|\zeta|}\sin\frac{\theta_3}{2} \\ 0 & -i\frac{\zeta}{|\zeta|}\sin\frac{\theta_3}{2} & \cos\frac{\theta_3}{2} \end{pmatrix}$$

and consequently

$$\mathrm{M}^{-1}_{3b\leftrightarrow c>} = \begin{pmatrix} 1 & 0 & 0 \\ 0 & \cos\frac{\theta_3}{2} & i\frac{\zeta^*}{|\zeta|}\sin\frac{\theta_3}{2} \\ 0 & i\frac{\zeta}{|\zeta|}\sin\frac{\theta_3}{2} & \cos\frac{\theta_3}{2} \end{pmatrix}$$

Since the first two pulses are the same for both the ground-state and excited-state tri-level echoes, for a system which is initially in the ground-state the resulting density matrix in the rotating frame after the second pulse is given

by equation 3.48 i.e.

$$\rho_\omega(t_2) = \begin{pmatrix} \rho_{aa}\prime & \rho_{ab}\prime & 0 \\ \rho_{ba}\prime & \rho_{bb}\prime & 0 \\ 0 & 0 & 0 \end{pmatrix}$$

where

$$\begin{aligned}
\rho_{aa}\prime &= \cos^2\frac{\theta_1}{2}\cos^2\frac{\theta_2}{2} + \sin^2\frac{\theta_1}{2}\sin^2\frac{\theta_2}{2} - \frac{1}{4}\sin\theta_1\sin\theta_2\left(\frac{\alpha^*\beta + \beta^*\alpha}{|\alpha||\beta|}\right) \\
\rho_{bb}\prime &= \sin^2\frac{\theta_1}{2}\cos^2\frac{\theta_2}{2} + \cos^2\frac{\theta_1}{2}\sin^2\frac{\theta_2}{2} + \frac{1}{4}\sin\theta_1\sin\theta_2\left(\frac{\alpha^*\beta + \beta^*\alpha}{|\alpha||\beta|}\right) \\
\rho_{ab}\prime &= \rho^*_{ba} = \frac{i}{2}\sin\theta_1\left(\cos^2\frac{\theta_2}{2}\frac{\alpha^*}{|\alpha|} - \sin^2\frac{\theta_2}{2}\frac{\alpha\beta^{*2}}{|\alpha||\beta|^2}\right) \div \frac{i}{2}\cos\theta_1\sin\theta_2\frac{\beta^*}{|\beta|}
\end{aligned}$$

The density matrix after the third pulse is obtained from

$$\rho_\omega(t_3) = \mathrm{M}_{3b\leftrightarrow c}\rho_\omega(t_2)\mathrm{M}^{-1}_{3b\leftrightarrow c}$$

giving

$$\rho_\omega(t_3) = \begin{pmatrix} \rho_{aa}\prime & \cos\frac{\theta_3}{2}\rho_{ab}\prime & i\frac{\zeta^*}{|\zeta|}\sin\frac{\theta_3}{2}\rho_{ab}\prime \\ \cos\frac{\theta_3}{2}\rho_{ba}\prime & \cos^2\frac{\theta_3}{2}\rho_{bb}\prime & \frac{i}{2}\frac{\zeta^*}{|\zeta|}\sin\theta_3\rho_{bb}\prime \\ -i\frac{\zeta}{|\zeta|}\sin\frac{\theta_3}{2}\rho_{ba}\prime & -\frac{i}{2}\frac{\zeta}{|\zeta|}\sin\theta_3\rho_{bb}\prime & \sin^2\frac{\theta_3}{2}\rho_{bb}\prime \end{pmatrix}$$

where the primed matrix elements are defined above.

Transforming back to the laboratory frame using equation 3.38 and the matrix

$$\mathrm{A} = \begin{pmatrix} 0 & 0 & 0 \\ 0 & \omega_1 & 0 \\ 0 & 0 & (\omega_1 - \omega_3) \end{pmatrix}$$

gives

$$\begin{aligned}
\rho(t) &= \begin{pmatrix} \rho_{aa} & \rho_{ab} & \rho_{ac} \\ \rho_{ba} & \rho_{bb} & \rho_{bc} \\ \rho_{ca} & \rho_{cb} & \rho_{cc} \end{pmatrix} \\
&= \begin{pmatrix} \rho_{aa}\prime & \cos\frac{\theta_3}{2}\rho_{ab}\prime e^{i\omega_1 t} & i\frac{\zeta^*}{|\zeta|}\sin\frac{\theta_3}{2}\rho_{ab}\prime e^{i(\omega_1-\omega_3)t} \\ \cos\frac{\theta_3}{2}\rho_{ba}\prime e^{-i\omega_1 t} & \cos^2\frac{\theta_3}{2}\rho_{bb}\prime & \frac{i}{2}\frac{\zeta^*}{|\zeta|}\sin\theta_3\rho_{bb}\prime e^{-i\omega_3 t} \\ -i\frac{\zeta}{|\zeta|}\sin\frac{\theta_3}{2}\rho_{ba}\prime e^{-i(\omega_1-\omega_3)t} & -\frac{i}{2}\frac{\zeta}{|\zeta|}\sin\theta_3\rho_{bb}\prime e^{i\omega_3 t} & \sin^2 \end{pmatrix} (t >
\end{aligned}$$

Since

$$\mathbf{p} = \begin{pmatrix} 0 & p_{ab} & 0 \\ p_{ba} & 0 & p_{bc} \\ 0 & p_{cb} & 0 \end{pmatrix}$$

then

$$\begin{aligned} < p > &= Tr(\rho \mathbf{p}) \\ &= p_{ab}\rho_{ba}e^{-i\omega_1 t} + p_{ba}\rho_{ab}e^{i\omega_1 t} + p_{bc}\rho_{cb}e^{i\omega_3 t} + p_{cb}\rho_{bc}e^{-i\omega_3 t} \\ &= \mathcal{P}_{ab} + \mathcal{P}_{bc} \end{aligned}$$

Note that the echo is formed from $\mathcal{P}_{bc}$, which contains $\rho_{bb'}$, the excited state population after the first two excitation pulses.

For the stimulated echo shown in Figure 1.23(c), the density matrix formed after the first two pulses is identical to that for the tri-level echo experiments. After the third pulse, the dipole moment expectation value is given by

$$\begin{aligned} < p > &= Tr(\rho \mathbf{p}) \\ &= p_{ab}\rho_{ba}e^{-i\omega_3 t} + p_{ba}\rho_{ab}e^{i\omega_3 t} \end{aligned}$$

where

$$\rho_{ab} = \rho^*_{ba} = -\frac{i}{2}\frac{\gamma^*}{|\gamma|}(\rho_{bb'} - \rho_{aa'})$$

These density matrix elements contain the memory terms

$$\begin{aligned} T^{(2)}_{ab} &= -\frac{i}{8}\sin\theta_1 \sin\theta_2 \sin\theta_3 \frac{\alpha\beta^*\gamma}{|\alpha||\beta||\gamma} \\ T^{(3)}_{ab} &= \frac{i}{8}\sin\theta_1 \sin\theta_2 \sin\theta_3 \frac{\alpha^*\beta\gamma^*}{|\alpha||\beta||\gamma|} \end{aligned}$$

which produce the stimulated echo.

Appendix B: Caesium oven maintenance.

When either the oven windows need replacing, or more caesium needs to be added, the oven has to be disconnected from the vacuum system. The procedure adopted is as follows. Valves '4', '5' and the solenoid valve (see Figure 4.9) are closed, and the evacuated caesium oven, with valve '5' attached, is disconnected and placed inside an 'Atmos' bag (a transparent, polythene gas chamber which has one large, resealable opening, and a number of smaller openings for admitting and exhausting gas). The bag is then sealed and physically compressed in order to remove as much air from it as possible, before being filled with high purity nitrogen. The emptying and filling procedures are then each repeated three more times, after which it is estimated that the air in the bag has been reduced to one part in 10^5 or better. The excess pressure within the bag over the surrounding atmospheric pressure prevents any air from entering back through the exhaust outlet. The windows and 'O'-rings can then be removed and replaced, and if necessary caesium can be added to the oven from a 1g phial. The resealed oven is then reconnected to the vacuum system.

Both window changing and oven refilling can be performed with the oven disconnected from the vacuum system for less than 10 minutes, though throughout this time the bellows are open to the air. To prevent this air from contaminating the oven, everything below valve '5' is evacuated with the diffusion pump. Valve '5' is then opened momentarily (in order to further reduce the quantity of air in the oven) before the bellows are baked for about an hour at $\simeq$100°C via a heater tape, to drive off any contaminants from the bellows walls. The bellows are then allowed to cool to room temperature

before valve '5' is opened. The oven seals (window and bellows) are checked with the ion gauge, before the oven and bellows are heated to the required temperature.

Whenever there is a large quantity of contaminated caesium in the oven the oven has to be emptied completely. Clean windows are put on the empty oven, which is connected to the vacuum system. The empty oven and bellows are then baked out at $\simeq$100°C, again for about an hour, but this time the oven is evacuated as well as the bellows. They are both then left to cool to room temperature before the oven is filled with caesium as described above.

Bibliography

[1] K W Godfrey, Ph.D. Thesis *An optical echo study of caesium-noble gas collisions* (1989)

[2] B H Bransden and C J Jochain, *Physics of atoms and molecules* pub. Longman (1983)

[3] A Yariv, *Quantum Electronics — 3rd Edition* pub. Wiley 342-52

[4] A P Thorne, *Spectrophysics* pub. Chapman and Hall (1974)

[5] S Y Ch'en, E L Lewis and D N Stacey, J. Phys. B: At. Mol. Phys. **2** (1969) 274-6

[6] F Rostas and J L Lemaire, J. Phys. B: At. Mol. Phys. 4 (1971) 555-64

[7] G Smith, J. Phys. B: At. Mol. Phys. 8 (1975) 2273-82

[8] T W Hansch, I S Shahin and A L Schawlow, Nat. Phys. Sci. **235** (1972) 63-5

[9] C Bréchignac, R Vetter and P R Berman, J. Phys. B: At. Mol. Phys. **10** (1977) 3443-50

[10] I Colomb and M Dumont, Opt. Comm. 21 (1977) 143-6

[11] I Colomb, M Gorlicki and M Dumont, Opt. Comm. 21 (1977) 289-92

[12] J-L Le Gouët, J. Phys. B: At. Mol. Phys. 11 (1978) 3001-14.

[13] F Biraben, B Cagnac, E Giacobino and G Grynberg, J. Phys. B: At. Mol. Phys. 10 (1977) 2369

[14] R L Shoemaker, *Laser and Coherence Spectroscopy*, ed. Steinfeld, pub. Plenum Press, 197-371

[15] L Allen and J H Eberly, *Optical Resonance and Two-level Atoms* pub. Wiley

[16] H C Torrey, Phys. Rev. **76** (1949) 1059-68

[17] G B Hocker and C L Tang, Phys. Rev. Lett. **21** (1968) 591

[18] R G Brewer and R L Shoemaker, Phys. Rev. A **6** (1972) 2001

[19] E L Hahn, Phys. Rev. **80** 4 (1950) 580-94

[20] R P Feynman, F L Vernon, Jr, and R W Hellwarth, J. Appl. Phys. **28** (1957) 49-52

[21] T W Mossberg and S R Hartmann, Phys. Rev. A **23** (1981) 1271-80

[22] R Beach, S R Hartmann and R Friedberg, Phys. Rev. A **25** (1982) 2658-66

[23] A V Durrant, J Manners and P M Clark, Eur. J. Phys. **10** (1989) 291-7

[24] P R Berman, T W Mossberg and S R Hartmann, Phys. Rev. A **25** (1982) 2550-71

[25] N A Kurnit, I D Abella and S R Hartmann, Phys. Rev. Lett. **15** (1964) 567-8

[26] I D Abella, N A Kurnit and S R Hartmann, Phys. Rev. **141** (1965) 390-406

[27] A Compaan, A Q Lambert and I D Abella, Phys. Rev. Lett. **20** (1968) 1089-91

[28] M Scully, M J Stephen and D C Burnham, Phys. Rev. **171** (1968) 213-4

[29] A Rebane and D Haarer, Opt. Comm. **70** (1989) 478-82

[30] C K N Patel and R E Slusher, Phys. Rev. Lett. **20** (1968) 1087-9

[31] J P Gordon, C H Wang, C K N Patel, R E Slusher and W J Tomlinson, Phys. Rev. **179** (1969) 294-309

[32] J R Meckley and C V Heer, Phys. Lett. **46A** (1973) 41-2

[33] W M Gutman and C V Heer, Phys. Lett. **51A** (1975) 437-8

[34] R G Brewer and R L Shoemaker, Phys. Rev. Lett. **27** (1971) 631-4

[35] J Schmidt, P R Berman and R G Brewer, Phys. Rev. Lett. **31** (1973) 1103-6

[36] H Y Carr and E M Purcell, Phys. Rv. **94** (1954) 630-9

[37] T W Mossberg, R Kachru, S R Hartmann and A R Flusberg, Phys. Rev. A **20** (1979) 1976-96

[38] P R Berman, J M Levy and R G Brewer, Phys. Rev. A **11** (1975) 1668-88

[39] B Bölger and J C Diels, Phys. Lett. **28A** (1968) 401

[40] T W Mossberg, R Kachru, K P Leung, E Whittaker and S R Hartmann, *Spectral Line Shapes*, pub. Walter de Gruyter & Co. (1981) 1093-110

[41] T W Mossberg *Spectral Line Shapes, Vol. 2*, pub. Walter de Gruyter & Co. (1983) 899-915

[42] T Baer and I D Abella, Phys. Lett. **59A** (1976) 371-2

[43] L Q Lambert, A Compaan and I D Abella, Phys. Rev. A 4 (1971) 2022

[44] T Baer, Phys. Rev. A 18 (1978) 2570-79

[45] T Baer and I D Abella, Phys. Rev. A 16 (1977) 2093-100

[46] S Aoki, Phys. Rev. A **20** (1979) 2013-21

[47] B Bölger, L Baede and H M Gibbs, Opt. Comm. **18** (1976) 67-8

[48] R G Brewer and Z A Genack, Phys. Rev. Lett. **36** (1976) 959-62

[49] A Flusberg, T Mossberg and S R Hartmann, Opt. Comm. **24** (1978) 207-10

[50] T W Mossberg, R Kachru and S R Hartmann, Phys. Rev. Lett., 44 (1980) 73-7

[51] R Kachru, T W Mossberg and S R Hartmann, J. Phys. B: At. Mol Phys. **13** (1980) L363-8

[52] R Beach, B Brody and S R Hartmann, Phys. Rev. A **27** (1983) 2925-9

[53] R Kachru, T J Chen, S R Hartmann, T W Mossberg and P R Berman, Phys. Rev. Lett. **47** (1981) 902-5

[54] R Kachru, T J Chen, T W Mossberg and S R Hartmann, Phys. Rev. A **25** (1982) 1546-9

[55] R A Forber, J E Thomas, L Spinelli and M S Feld, *Spectral Line Shapes* pub. Walter de Gruyter & Co. (1983) 945- 59

[56] R A Forber, L Spinelli, J E Thomas and M S Feld, Phys. Rev. Lett. **50** (1983) 331-5

[57] J E Thomas, R A Forber, L A Spinelli and M S Feld, Phys. Rev. Lett. **51** (1983) 2194-7

[58] A V Durrant and J Manners, Opt. Comm. **49** (1984) 293-6

[59] A V Durrant and J Manners, J Phys. B: At. Mol. Phys. **17** (1984) L701-6

[60] P Munster and J Marek, J. Phys. B: At. Mol. Phys. 14 (1981) 1009-18

[61] A V Durrant, J Manners and K W Godfrey, J. Mod. Opt. **36** (1989) 1173-84

[62] M Aihara and H Inaba, Opt. Comm. **8** (1973) 280-4

[63] M Aihara and H Inaba, J Phys. A: Math., Nucl. Gen. **6** (1973) 1709-24

[64] M Aihara and H Inaba, J Phys. A: Math., Nucl. Gen. **6** (1973) 1725-42

[65] A Flusberg, T W Mossberg, R Kachru and S R Hartmann, Phys. Rev. Lett. **41** (1978) 305-8

[66] M Fujita, H Nakatsuka, H Nakanishi and M Matsuoka, Phys. Rev. Lett. **42** (1979) 974-7

[67] S Asaka, H Yamada, H Nakatsuka and M Matsuoka, J. Phys. Soc. Jpn. **52** (1983) 3029-38

[68] T W Mossberg, A Flusberg, R Kachru and S R Hartmann, Phys. Rev. Lett. **39** (1977) 1523-6

[69] A Flusberg, R Kachru, T W Mossberg and S R Hartmann, Phys. Rev. A **19** (1979) 1607-21

[70] T W Mossberg, E Whittaker, R Kachru and S R Hartmann, Phys. Rev. A **22** (1980) 1962-9

[71] J Manners and A V Durrant, Opt. Comm. **58** (1986) 389-94

[72] T Mossberg, A Flusberg, R Kachru and S R Hartmann, Phys. Rev. Lett. **42** (1979) 1665-9

[73] R Kachru, T W Mossberg and S R Hartmann, Opt. Comm. **30** (1979) 57-62

[74] J -C Keller and J -L Le Gouët, *Spectral Line Shapes* pub. Walter de Gruyter & Co. (1985) 309-334

[75] J -C Keller and J -L Le Gouët, Phys. Rev. Lett. **52** (1984) 2035-7

[76] J -C Keller and J -L Le Gouët, Phys. Rev. A **32** (1985) 1624-41

[77] A G Yodh, J Golub and T W Mossberg Phys. Rev. A **32** (1985) 844-53

[78] A P Ghosh, C D Nabors, M A Attili and J E Thomas, Phys. Rev. Lett. **54** (1985) 1794-7

[79] J E Thomas, A P Ghosh and A Attili, Phys. Rev. A **33** (1986) 3029

[80] N W Carlson, W R Babbitt and T W Mossberg, Opt. Lett. **8** (1983) 623-5

[81] I V Yevseyev and V A Reshetov, Opt. Commun. **72** (1989) 377-80

[82] I V Evseev, P V Nesterov and V A Reshetov, Optica Acta **32** (1985) 357

[83] R. Loudon,.*The Quantum Theory of Light* 52 (Oxford University Press, 1973)

[84] J U White, J. Opt. Soc. Am. **32** (1942) 285-8

[85] R E Honig and D A Kramer, RCA Review **30** (1969) 285

[86] P R Berman, *Les Houches, Session XXXVIII (1982) — New Trends In Atomic Physics*, pub. Elsevier Science Publishers B.V. (1984) 451-515

[87] A Flusberg, Opt. Comm. **29** (1979) 123- 5

[88] J Guiry and L Krause, Phys. Rev. A 14 (1976) 2034-42

[89] V N Rebane and T K Rebane, Opt. Spectrosc. **33**